Test of the Equivalence Principle in an Einstein Elevator

Annual Report #2

NASA Grant NAG8-1780

For the period 1 March 2002 through 28 February 2003

Principal Investigator

Irwin I. Shapiro

June 2003

Prepared for
National Aeronautics and Space Administration
Office of Biological and Physical Research
Washington, DC

Smithsonian Institution
Astrophysical Observatory
Cambridge, Massachusetts 02138

The Smithsonian Astrophysical Observatory
is a member of the
Harvard-Smithsonian Center for Astrophysics

Test of the Equivalence Principle in an Einstein Elevator

Annual Report #2

NASA Grant NAG8-1780

For the period 1 March 2002 through 28 February 2003

Principal Investigator

Irwin I. Shapiro

Co-Investigators

E.C. Lorenzini
S. Glashow
M.L. Cosmo
P. Cheimets (Project Engineer)
N. Finkelstein (E/PO)
M. Schneps (E/PO)

Non-US Partners (IFSI/CNR)

V. Iafolla (Non-US PI)
S. Nozzoli (Co-I)

Collaborators

J. Ashenberg

Ph.D. Students

G. Parzianello
C. Bombardelli
A. Turner

SAO Engineering

M. Freeman
M. Burke
R. Eng

June 2003

Prepared for
National Aeronautics and Space Administration
Office of Biological and Physical Research
Washington, DC

Smithsonian Institution
Astrophysical Observatory
Cambridge, Massachusetts 02138

TABLE OF CONTENTS

LIST OF FIGURES

LIST OF TABLES

INTRODUCTION

The scientific goal of the experiment is to test the equality of gravitational and inertial mass (i.e., to test the Principle of Equivalence) by measuring the independence of the rate of fall of bodies from their compositions. The measurement is accomplished by measuring the relative displacement (or equivalently acceleration) of two falling bodies of different materials which are the proof masses of a differential accelerometer. The experiment is a null experiment in which a result different from zero will indicate a violation of the Equivalence Principle. The final aim is to measure the Eötvös ratio $\delta g/g$ (differential acceleration/common acceleration) with a targeted accuracy that is much improved with respect to the state of the art (presently at several parts in 10^{13}).

The estimate of the accuracy attainable with our experimental method is being carefully evaluated based on more refined analyses and advancements in the definition of the system. As the work progresses, we are setting our accuracy goal at improving the present EP test accuracy by about two orders of magnitude.

The analyses carried out have focused on: (1) the evaluation of modal frequencies of the detector; (2) the dynamics of the instrument package after release following an imperfect release; (3) the computation of the higher-order mass moments on the proof masses generated by nearby masses; (4) thermal analysis of the instrument package during flight operation; (5) a preliminary design of the leveling and release mechanisms; and (6) a conceptual design of the cryostat and its interface. We are also cooperating with a cryostat designer on the topic of cryostat design development and costing.

The project also involves an international cooperation with the Institute of Space Physics (IFSI/CNR) in Rome, Italy. The group at IFSI is in charge of prototyping the differential accelerometer and carrying out precursor laboratory measurements. Our Italian colleagues have received their external funding on this project from the Italian Space Agency (ASI) in November 2002. Thanks to some activity carried out in 2002 with IFSI internal funds and the new activities made possible by the ASI funds, they have been remarkably productive. They built a differential accelerometer laboratory prototype and carried out very important laboratory measurements focused on evaluating the common-mode rejection factor and on techniques for damping the natural dynamics of the accelerometer after release. The highlights of these activities are documented in a section of this report.

UPDATE ON SCIENTIFIC ISSUES

Need for Tests with Improved Accuracy

The accuracy of the Equivalence Principle (EP) tests with laboratory proof masses on the ground is limited by the Earth's seismic noise and the weakness of suitable signal sources. Previous experiments include the famous torsion balance experiments of Eötvös (1890-1922)[i] [ii] as well as the classical tests of the Equivalence Principle by Roll-Krotkov-Dicke (1964)[iii] utilizing a torsion balance which had an accuracy of 3 parts in 10^{11} and the I.I. Shapiro et al. (1976)[iv] and Williams et al. (1976)[v] lunar laser ranging experiment with an accuracy of 3 parts in 10^{12}. The present state of the art is at several parts in 10^{13} both for lunar laser ranging tests (Williams et al., 1996)[vi] and for torsion balance tests (Adelberger et al., 1999)[vii].

In two recent papers[viii] [ix], Damour et al., provide a theoretical justification, based on the string theory for expecting violations of the Equivalence Principle at an accuracy above one part in 10^{-12} which is slightly below the present state of the art in EP tests. Their argument centers on the inflationary rate of expansion of the early universe and on the decoupling of scalar fields from matter during the expansion of the universe. When the recent estimates of the early expansion rates are factored into the theory, they conclude that violations of the EP may well occur at accuracy much lower than previously thought.

The conclusion of the analysis by Damour et al. gives strength to EP experiments with improved accuracy even if the improvement is not as dramatic as those promised by the space-based tests (of several orders of magnitude) of the EP. Another implication is that our goal should not be to push the accuracy as high as possible (and consequently increase the difficulty and cost of the experiment) but rather achieve a significant improvement in accuracy with respect to the present state of the art.

One of the strength of our experiment is that by conducting it in free fall, the strength of the signal is increased by about three folds with respect to the signal available to experiments conducted in the laboratory. This simple fact simplifies the detector requirements vs. an equivalent-accuracy experiment conducted on the ground. However, in a drop experiment like ours, the measurement time is limited and, consequently, the detector must satisfy requirements associated with the ability to abate the transient dynamics after release.

A rapid damping of the detector natural oscillations excited by the instrument release during the first few seconds of release is required. This point translates into the ability to switch the detector's quality factor from the high value required during the data taking to low values during the damping phase. Our colleague at IFSI in Rome have already demonstrated with laboratory tests of a precursor accelerometer that this is indeed possible (see later on).

The test of the Equivalence Principle requires a differential measurement of acceleration. This fact has a positive consequence in terms of the rejection of accelerations that affect the two proof masses equally (common-mode type) and their effects on the differential acceleration. The capsule shields the free falling detector from external perturbations and provides a quiet environment for the experiment. However, the noise produced by the detector moving inside the co-moving capsule is not equal to zero. The residual gas in the evacuated capsule produces a tiny drag force and also allows the propagation of strongly-attenuated perturbations from the capsule's wall. The evaluation carried out in the previous Annual Report[x] on the noise related to residual gas in the capsule points to the need for a common-mode rejection factor of 10^{-4} in order to meet the desired target accuracy. Our Italian colleagues have already carried out laboratory measurements on the instrument prototype and achieved the required common-mode rejection factor in the frequency band of interest.

UPDATED REFERENCE CONFIGURATION

Capsule mass and Size

One of the important results of the analysis carried out is that the small vacuum chamber at the top of the capsule has been eliminated in favor of a fully cryogenic vacuum chamber (see Figure 1). The new solution eliminates the problem of the gravity gradient produced by the small cryostat in the proximity of the detector and also provides more clearance to the instrument package during the early stage of free fall.

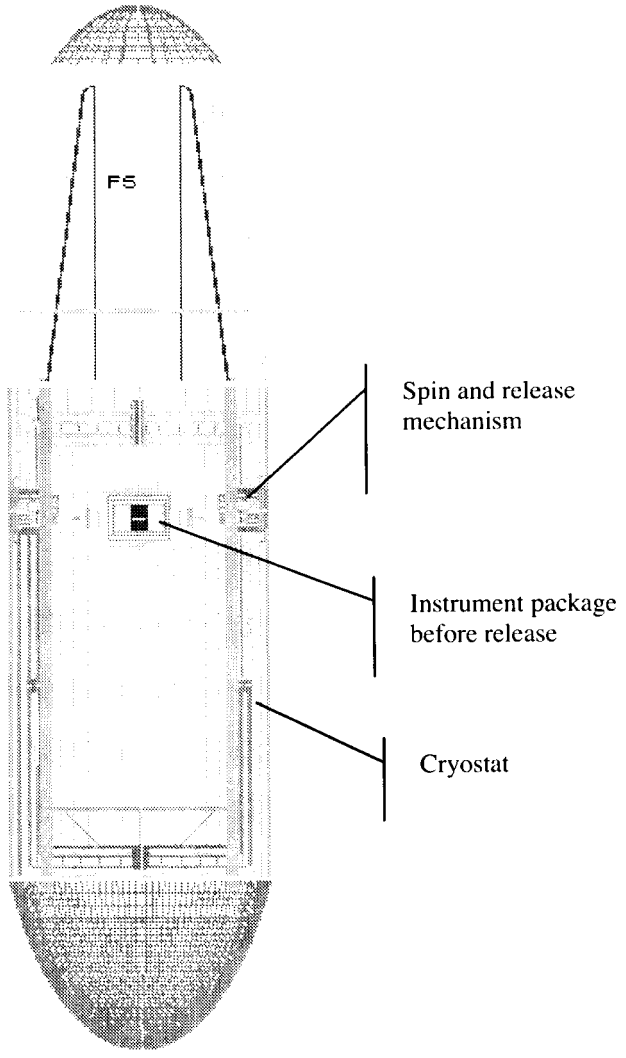

Figure 1 Schematic of capsule with instrument package attached before release

The new configuration also has the advantage of using a more conventional design of the cryostat rather than one with doors opening at the bottom as in the old reference design.

The preferred size of the vacuum chamber/cryostat was identified(see the analysis/optimization conducted in Annual Report#1) as a cylinder with internal diameter of 1 m and an internal height of 2.1 m which results in an external diameter for the capsule of about 1.4 m and a free-to-chose capsule length of roughly 5.6 m. Preliminary data on large cryostats (from Janis Research), indicate that the mass of a cryostat of the size considered above will fit well within the mass limit of the system. Such chamber/cryostat will allow free fall times in the range 24-28 s depending on the amount of ballast added to the capsule.

The overall capsule mass could start at a minimum value of about a 1000 kg which provides a free fall time of about 24 s. The free-fall time can be increased by 1 s for every 250-kg ballast (or other equipment) added to the capsule up to the point where the a (limit) mass of 2000 kg is reached. The low-speed ballistic coefficient β_0 of the capsule will vary from about 6500 kg/m^2 for a capsule mass = 1000 kg to 13,000 kg/m^2 for a capsule mass of 2000 kg. Correspondingly, the free fall time will vary from 24 s to 28 s.

Experiment Sequence

Figure 3 shows the preliminary timetable of the experiment sequence. The experiment starts with the loading of the sensor into the vacuum chamber/cryostat about 2 weeks before the planned launch. This operation is then followed by the pumping down of the chamber and the refrigeration of the sensor. After connecting the capsule to the gondola and the balloon, the balloon is launched. The estimated time to reach altitude is of order 3 hours. Upon reaching altitude, the attitude of the capsule is stabilized by the leveling mechanism on the gondola, the sensor is spun up, and the dynamics of the system is analyzed. When the dynamics is within the acceptable bounds, the capsule is released from the gondola and the sensor is released from the top of the chamber/cryostat immediately afterwards. The science data is taken during the free-fall phase in which the sensor spans the length of the chamber. Shortly after the sensor has reached the bottom of the capsule, the blut (first stage of the deceleration system) is released and, when the speed has decreased below the required value, the parachute is deployed.

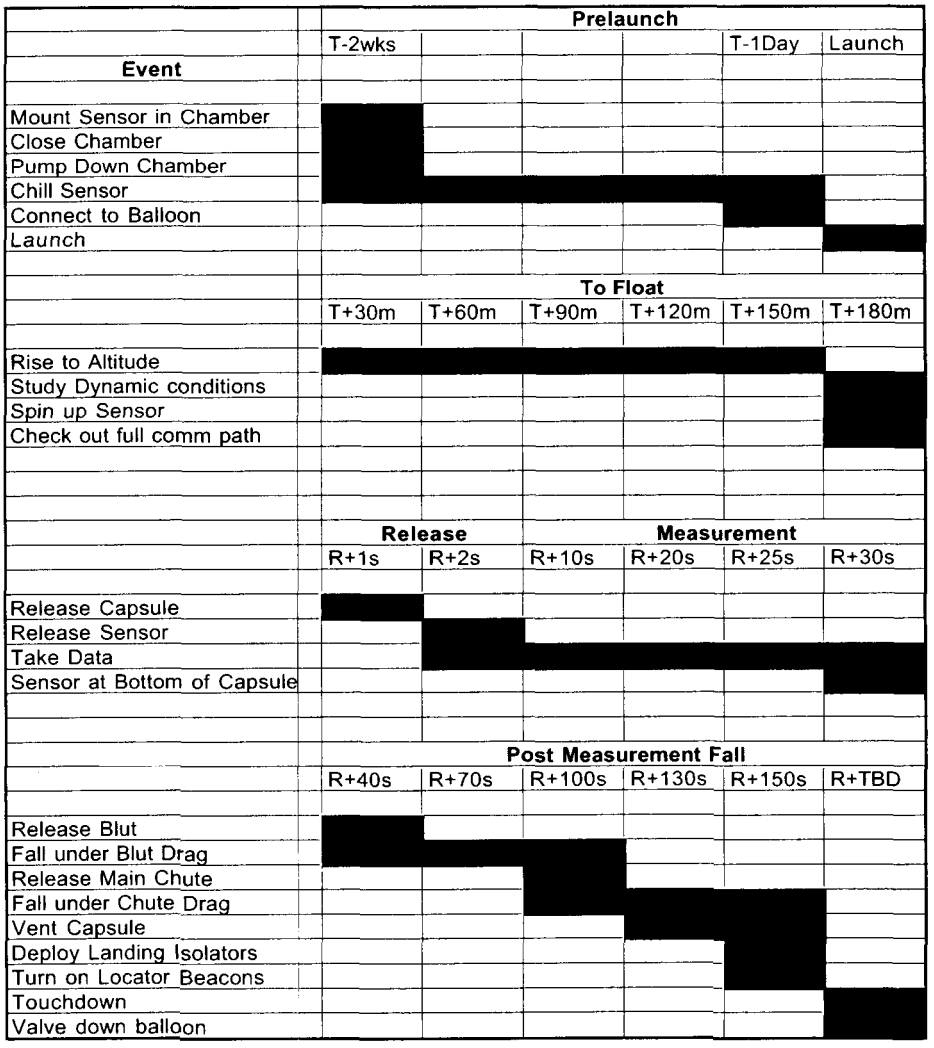

Figure 2 Preliminary timeline of experiment

Capsule Drop Dynamics

The free fall time of the instrument package inside the capsule was computed for several values of the low-speed ballistic coefficient in the previous Annual Report. Figure 4 depicts the capsule drop distance and Mach number vs. drop time.

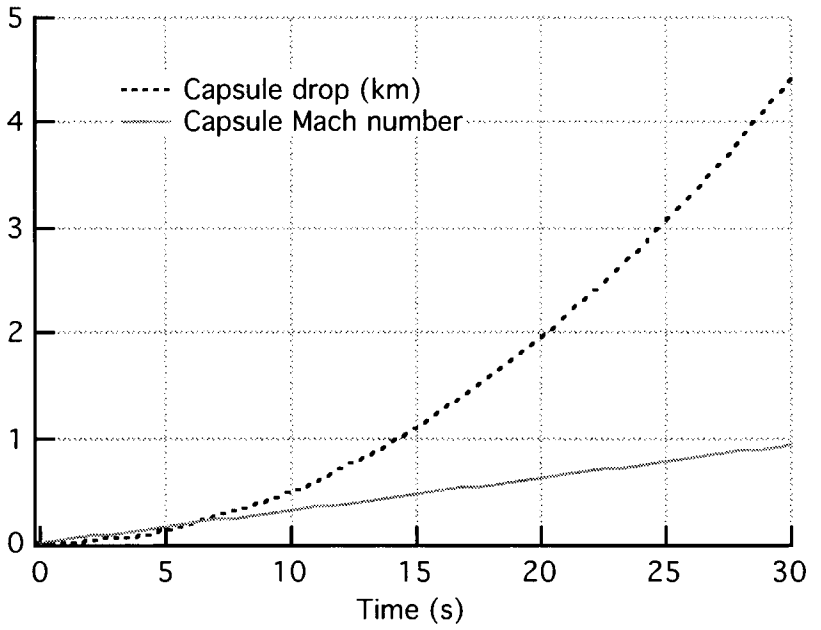

Figure 3 Capsule drop and Mach number vs. drop time

Following up the computation of the preferable range of values for the capsule mass and size, Figure 5 shows the relative distance covered by the instrument package during free fall with respect to the capsule for a low-speed ballistic coefficient ranging from 6500 kg/m^2 to 13500 kg/m^2.

These results clearly indicate that a capsule of relatively compact size can provide a free fall time between 24 s and 28 s with a capsule mass ranging from 1000 kg to 2000 kg, respectively. The higher value of the mass is for the same capsule with ballast.

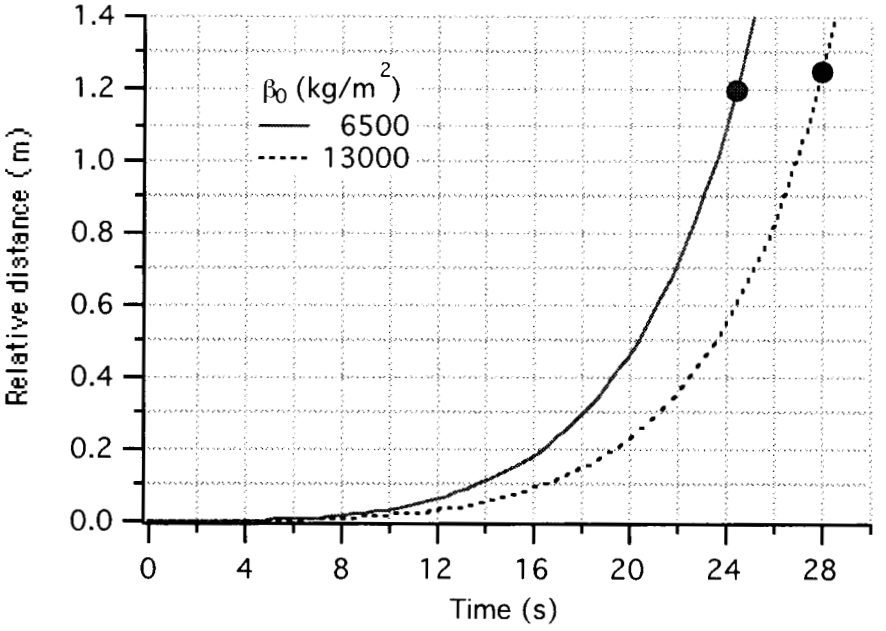

Figure 4 Relative vertical distance vs. free fall time for limit values of interest of ballistic coefficient. Dots mark the expected operating points for the light capsule (M = 1000 kg) and ballasted capsule (M = 2000 kg).

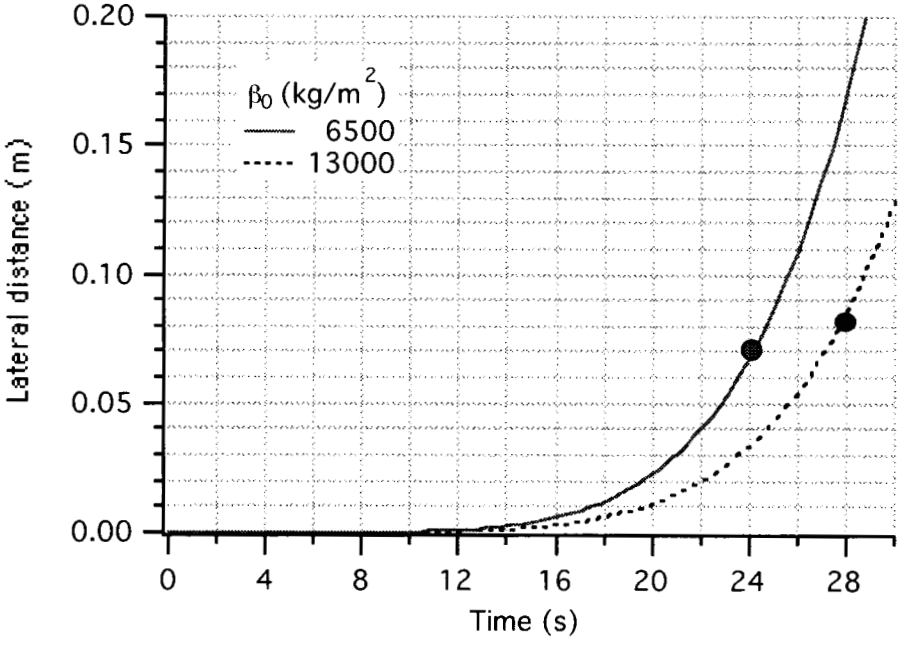

Figure 5 Relative lateral displacement due to wind shear vs. free fall time. Dots mark the expected operating points for the light capsule (M = 1000 kg) and ballasted capsule (M = 2000 kg).

An internal diameter of the capsule of 1 m was also computed from the optimization process. This diameter determines the tolerance to wind shear acting sideways on the capsule. Figure 6 shows the lateral displacement of the capsule with respect to the free-falling instrument package vs. free fall time for the limit values of interest for the low-speed ballistic coefficient. The value adopted for the wind shear of 0.005 s^{-1} is equivalent to a vertical gradient of 10 knots per km. This value is twice as high as the maximum wind shear reported[xi] for the Air Force balloon base at Holloman, New Mexico. The lateral displacements due to wind shear are relatively small in the parameter range of interest. Furthermore, if the balloon is launched during the periodically-occurring wind reversal times (in April-May and September-October) the vertical wind gradient is much smaller than the value adopted for the computations shown here.

MODAL ANALYSIS OF DETECTOR

Introduction

The following is the modal analysis of the differential accelerometer for the EP test. The sensor is composed by two masses of different materials constrained to an external case by means of elastic springs. The measurement is performed by monitoring the displacement of the two masses with respect to the external case through the measurement of capacitance variations caused by the displacement.

This analysis evaluates the eigenfrequencies and eigenmodes of the detector and the sensitivity of the modes to variations in the detector parameters.

The model adopts six degrees of freedom, that is, one rotation and one translation for each body. The system parameters considered for the sensitivity analysis are masses and moments of inertia of the bodies, stiffness of the springs and their ratio.

The influence of these parameters is evaluated on both the separation of the natural frequencies and the vibrational modes, particularly for what concerns the differential and common modes of the detector.

Detector Dynamics Model

The detector consists of two sensing masses having their Centers of Mass (CM) coincident with the CM of the external case. In the current detector model, one mass has a dumbbell shape, while the other is a hollow cylinder. The shape of the flight detector sensing masses will likely be different from this early choice. Nevertheless, the shape of the sensing masses, however, does not affect the generality of this study. The two sensing masses are constrained to the case by means of elastic springs, having a pivot axis parallel to the longitudinal axis of symmetry of the three elements. Figure 7 shows a schematic of the instrument model.

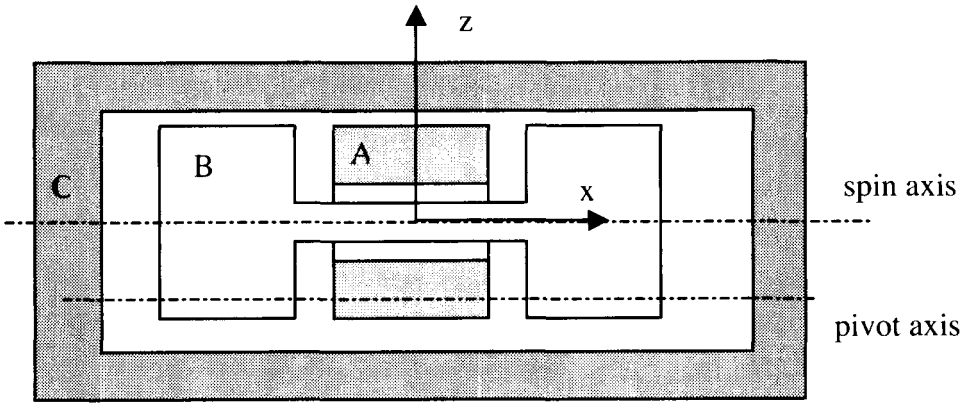

Figure 6 Schematic of detector model.

For this analysis, we assume that the capsule containing the sensor is fixed to the Earth surface, so that only the sensor is falling into it. This assumption does not affect the generality of the modal analysis. The Z axis is the axis of fall and of the Earth's gravity acceleration.

The reference system Cf is a frame parallel to the geographic X, Y, Z axes and displaced by the vector r_Z (see Fig. 8). Another coordinate system D is attached to the capsule and having axes parallel to the local normal frame. At this stage of the analysis, reference frame D is assumed to coincide with the local normal frame and the capsule is assumed stationary with respect to the Earth's surface. This assumption doesn't cause any loss of generality for the modal analysis. The coordinate that describes the fall of the case along the z axis is $r_z(t)$, where **r** is the position vector that identifies the body C (external case) with respect to the capsule and, finally, z indicates the axis of fall.

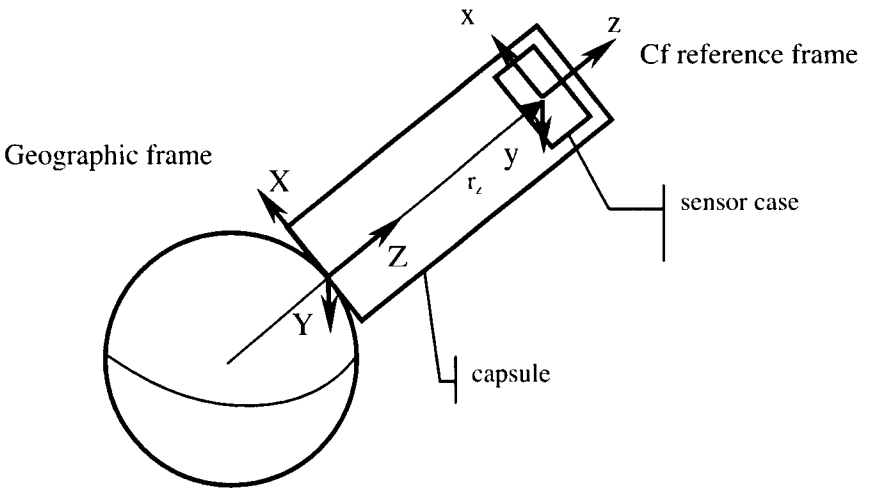

Figure 7 Local normal (geographic) and Cf frames

The body coordinate systems x, y, z are centered at the body CM, and fixed with the body itself. Each system has the x axis along the longitudinal axis of symmetry, corresponding also to the spin axis while the y and z axes are radial axes rotating with the body.

A rotational and translational degrees of freedom have been considered for each mass. More precisely, the x rotation about the CM of each mass, and the y translation referred to the xyz frame. Therefore each body can rotate about the x axis through its CM and can translate along the y axis of our reference frame. Figure 9 shows the possible movements of each body.

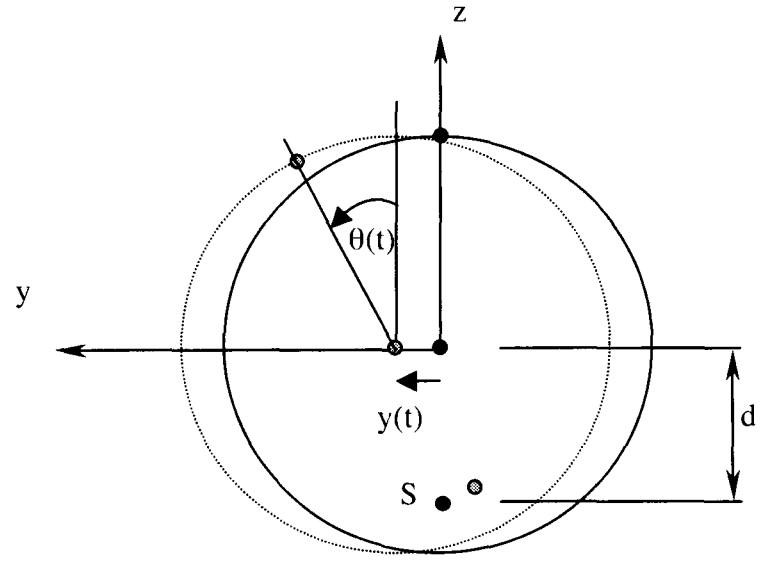

Figure 8 Degrees of freedom of each body

External forces

The motion of the sensing mass consists of a rotation θ(t) about the pivot axis (related to the torsional stiffnesses of the springs) and a translation y(t) that depends on the flexural stiffness of the springs. The flexural stiffnesses are typically much greater than the torsional ones. The distance *d* in the figure identifies the distance between the CM of the sensing mass and the pivot axis.

The external forces are written in the Cf reference frame, and consist of elastic forces. The elastic forces are produced by the springs connecting the sensing masses to the external case, and consist of a torsional torque and a force. In this analysis we assume that the rotational displacements are small, so that the displacement of the point S along the y axis due to a rotation around the CM is simply equal to θd [i. e. we assume that $\cos(\theta) = \theta$].

The differential displacement of the point S between body A and body C and the elastic force along the y axis are therefore:

$$\Delta y_A = y_A - \theta_A \cdot d_A - (y_C - \theta_C \cdot d_A)$$

$$F_{yA} = -k_{yA} \cdot \Delta y_A = -k_{yA} (y_A - \theta_A \cdot d_A - y_C + \theta_C \cdot d_A)$$

Where y_A and y_C, are the displacements along the y axis with respect to the Cf frame, θ_A and θ_C are the rotations about the x axis of masses A and C, respectively. k_{yA} is the flexural stiffness along y of the spring connecting body A to the case C.

The elastic torque about the CM of A is:

$$N_A = -k_{tA}(\theta_A - \theta_C) - k_{yA}\cdot d_A\cdot\Delta y_A = -k_{tA}(\theta_A - \theta_C) - k_{yA}\cdot d_A(y_A - \theta_A\cdot d_A - y_C + \theta_C\cdot d_A)$$

Where k_{tA} is the torsional stiffness of the spring connecting A and C.

Similarly, for the other two bodies we have:

$$F_{yB} = -k_{yB}\cdot\Delta y_B = -k_{yB}(y_B - \theta_B\cdot d_B - y_C + \theta_C\cdot d_B)$$

$$N_B = -k_{tB}(\theta_B - \theta_C) - k_{yB}\cdot d_B\cdot\Delta y_B = -k_{tB}(\theta_B - \theta_C) - k_{yB}\cdot d_B(y_B - \theta_B\cdot d_B - y_C + \theta_C\cdot d_B)$$

$$F_{yC} = -k_{yA}(y_C - \theta_C\cdot d_A - y_A + \theta_A\cdot d_A) - k_{yB}(y_C - \theta_C\cdot d_B - y_B + \theta_B\cdot d_B)$$

$$N_C = -k_{tA}(\theta_C - \theta_A) - k_{yA}\cdot d_A(y_C - \theta_C\cdot d_C - y_A + \theta_A\cdot d_A) - k_{tB}(\theta_B - \theta_C) - k_{yB}\cdot d_B(y_B - \theta_B\cdot d_B - y_C + \theta_C\cdot d_B)$$

These equations will be used in the next section to compute the stiffness matrix.

Modal Analysis

The mass and stiffness matrices are computed in this section. It has to be noted that out of 18 degrees of freedom (DoF) associated with the translational and rotational motion of the three masses only six of them are describing the motion of the degrees of freedom of interest. Specifically, only the translations along the y axis and the rotations about the x axis have to be considered for each body because the other motions do not affect the measurement. The state vector involved is, therefore, as follows:

$$X = [y_A \; y_B \; y_C \; \theta_A \; \theta_B \; \theta_C \;]^T \tag{8}$$

which contains the translations along y axis and the rotations about the principal x axis of each body.

The mass matrix is a diagonal matrix in a system of rigid bodies as follows:

$$M = \begin{bmatrix} m_A & 0 & 0 & 0 & 0 & 0 \\ 0 & m_B & 0 & 0 & 0 & 0 \\ 0 & 0 & m_C & 0 & 0 & 0 \\ 0 & 0 & 0 & I_{Axx} & 0 & 0 \\ 0 & 0 & 0 & 0 & I_{Bxx} & 0 \\ 0 & 0 & 0 & 0 & 0 & I_{Cxx} \end{bmatrix} \tag{9}$$

The stiffness matrix, obtained from the force and torque equations by using the displacement method, is:

$$K = \begin{bmatrix} k_{yA} & 0 & -k_{yA} & -d_A k_{yA} & 0 & d_A k_{yA} \\ 0 & k_{yB} & -k_{yB} & 0 & -d_B k_{yB} & d_B k_{yB} \\ -k_{yA} & -k_{yB} & k_{yA}+k_{yB} & d_A k_{yA} & d_B k_{yB} & -d_A k_{yA} - d_B k_{yB} \\ -d_A k_{yA} & 0 & d_A k_{yA} & k_{tA} + d_A^2 k_{yA} & 0 & -k_{tA} - d_A^2 k_{yA} \\ 0 & -d_B k_{yB} & d_B k_{yB} & 0 & k_{tB} + d_B^2 k_{yB} & -k_{tB} - d_B^2 k_{yB} \\ d_A k_{yA} & d_B k_{yB} & -d_A k_{yA} - d_B k_{yB} & -k_{tA} - d_A^2 k_{yA} & -k_{tB} - d_B^2 k_{yB} & k_{tA} + k_{tB} + d_A^2 k_{yA} + d_B^2 k_{yB} \end{bmatrix}$$

(10)

We can observe that for an external body that is not constrained in its free fall, two rigid motions are possible, that is, the rigid body rotation around the x axis of the Cf frame, and the rigid body translation along the y axis. In order to carry out an analysis of the natural frequencies and natural modes of the system we can eliminate these two rigid motions so as to preserve only the elastic modes. This can be done by expressing one rotational and one translational coordinate of a body as a function of the corresponding coordinates of the other two bodies.

A vector having the three translations equal to a constant and the three rotations equal to zero is a solution of the eigenproblem, so that this vector is an eigenvector. Consequently, all the others eigenvectors must be orthogonal to this one to yield:

$$\{\Phi_0\}^T [M]\{\Phi\} = 0$$

where Φ_0 is a rigid eigenvector, and Φ is another eigenvector. After evaluating the matrix products we obtain:

$$\Phi_0(m_A\Phi_1 + m_B\Phi_2 + m_C\Phi_3) = 0$$

where now Φ_i is the i-th component of a general eigenvector. Because $\Phi_i = fx_i$, where x_i is the i-th component of the vector x and f is a constant equal for all the components, we can also write

$$m_A y_A + m_B y_B + m_C y_C = 0$$

which allows to express one translational coordinate of a body as function of the translations of the other two. It can also be noted that in deriving the former equation we have obtained the conservation of the linear momentum for any elastic motion.

We can obtain similar expressions for the rotational case as follows (from now on we drop the subscript "xx" in the moments of inertia):

$$I_A \theta_A + I_B \theta_B + I_C \theta_C = 0$$

We can now express the coordinates of a body as function of the analogous coordinates of the other two bodies. We can write therefore

$$\{x\} = [C]\{x_c\}$$

where x is the coordinate vector, C is a matrix, and x_e is the new coordinate vector having the two coordinates of a body expressed as function of the others. In our case, we have eliminated the coordinates of body C, obtaining the following matrix [C]:

$$C = \begin{bmatrix} 1 & 0 & 0 & 0 \\ 0 & 1 & 0 & 0 \\ -\frac{m_A}{m_C} & -\frac{m_B}{m_C} & 0 & 0 \\ 0 & 0 & 1 & 0 \\ 0 & 0 & 0 & 1 \\ 0 & 0 & -\frac{I_A}{I_C} & -\frac{I_B}{I_C} \end{bmatrix} \tag{11}$$

and the vector X_e being

$$X_e = \begin{bmatrix} y_A \\ y_B \\ \theta_A \\ \theta_B \end{bmatrix} \tag{12}$$

The stiffness and mass matrices can be modified using the new coordinates by

$[K_e] = [C]^T[K]\,[C]$

$[M_e] = [C]^T[M]\,[C]$

where M_e and K_e are the transformed mass and stiffness matrices which are not shown here for the sake of brevity. The dynamical matrix $[D] = [M_e]^{-1}[K_e]$ that is needed to compute the eigenfrequencies of the elastic modes is as follows:

$$D = \begin{bmatrix} k_{yA}\left(\frac{1}{m_A}+\frac{1}{m_C}\right) & \frac{k_{yA}m_B}{m_A m_B} & -\frac{d_A k_{yA}(I_A+I_C)}{I_C m_A} & -\frac{d_A k_{yA} I_B}{I_C m_A} \\ \frac{k_{yB}m_A}{m_B m_C} & k_{yB}\left(\frac{1}{m_B}+\frac{1}{m_C}\right) & -\frac{d_B k_{yB} I_A}{I_C m_B} & -\frac{d_B k_{yB}(I_B+I_C)}{I_C m_B} \\ -\frac{d_A k_{yA}(m_A+m_C)}{I_A m_C} & -\frac{d_A k_{yA} m_B}{I_A m_C} & \frac{(I_A+I_C)\left(k_{tA}+d_A^2 k_{yA}\right)}{I_A I_C} & \frac{I_B\left(k_{tA}+d_A^2 k_{yA}\right)}{I_A I_C} \\ -\frac{d_B k_{yB} m_A}{I_B m_C} & -\frac{d_B k_{yB}(m_B+m_C)}{I_B m_C} & \frac{I_A\left(k_{tB}+d_B^2 k_{yB}\right)}{I_B I_C} & \frac{(I_B+I_C)\left(k_{tB}+d_B^2 k_{yB}\right)}{I_B I_C} \end{bmatrix} \tag{13}$$

Once solved the eigenvalue problem for the constrained system (i.e. with the previous dynamical matrix), the total eigenvector including also the two variables eliminated can be obtained simply premultiplying the eigenvector obtained by the matrix [C].

Eigenvalues and Eigenvectors.

Using the dynamical matrix evaluated before an analysis of the eigenvalues and eigenvectors have been carried out in order to evaluate the influence of parameters on the natural frequencies and modal vectors.

The parameters are the following:

M_A = mass of body A

M_B = mass of body B

M_C = mass of body C

I_A = moment of inertia of body A about the spin axis (x axis)

I_B = moment of inertia of body B about the spin axis (x axis)

I_C = moment of inertia of body C about the spin axis (x axis)

d_A = distance between the CM and the constrained point of body A

d_B = distance between the CM and the constrained point of body B

k_{tA} = torsional stiffness of spring connecting bodies A and C

k_{tB} = torsional stiffness of spring connecting bodies B and C

k_{yA} = bending stiffness of spring connecting bodies A and C

k_{yB} = bending stiffness of spring connecting bodies B and C

Numerical values have been assigned to these parameters to evaluate natural frequencies and eigenvectors. Subsequently, the values of key parameters have been changed while keeping the others constant.

The values used for the first evaluation are as follows:

$m_A = m_B = 5$ kg

$I_A = I_B = 0.009$ kg-m^2 (which corresponds to an external radius of body A of 0.06 m and a mass m_A)

$I_C = 1$ kg-m^2

$d_A = d_B = 0.06$ m

$k_{tA} = k_{tB} = 9.593$ Nm/rad (corresponding to a first torsional frequency for a single-degree-of-freedom system of 3 Hz)

$k_{yA} = k_{yB} = 18000\ \pi^2$ N/m (corresponding to a first lateral frequency for a single-degree-of-freedom system of 30 Hz)

Using these values we obtain the following values:

$f_1 = 2.99$ Hz; $f_2 = 3.29$ Hz

$f_3 = 52.13$ Hz; $f_4 = 55.22$ Hz

and the associated eigenvectors:

$v_1 = \{0.0427736, -0.0427736, 0.705812, -0.705812\}$

$v_2 = \{0.0326524, 0.0326524, 0.706352, 0.706352\}$

$v_3 = \{-0.0209932, 0.0209932, 0.706795, -0.706795\}$

$v_4 = \{-0.0210127, -0.0210127, 0.706795, 0.706795\}$

Remembering that the eigenvector components represent in order y_A, y_B, θ_A, θ_B, we can make a few considerations about the natural modes.

The first vector is composed of a translation of the masses and a rotation about the CM. The sign is opposite for the two masses, so that each of them moves in opposition to the other while the signs of y_A and θ_A are the same so that the pivot point tends to remain in its original position. In the first mode body C is at rest, the motion being auto-compensating. In summary, the first mode corresponds to a differential mode of the two test masses.

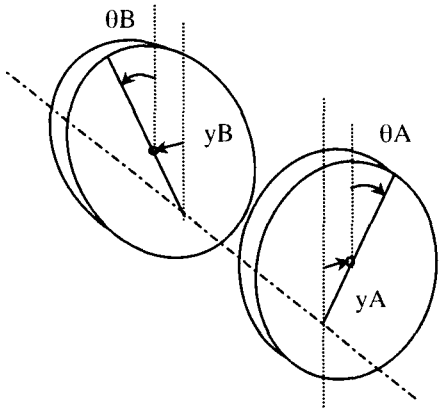

Figure 9 First natural mode (differential)

The second vibrational mode has a similar type of motion, the only difference being that the two masses move in the same direction. In this mode body C moves in the opposite direction of the masses in order to equilibrate the motion.

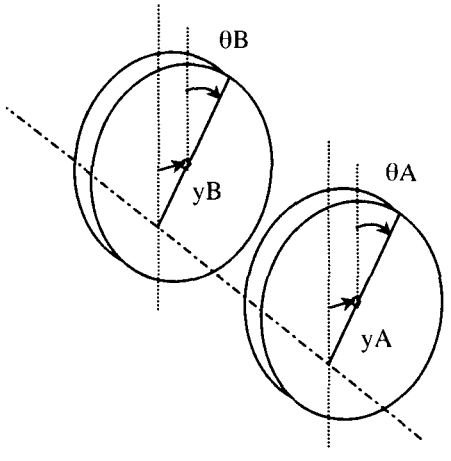

Figure 10 Second natural mode (common)

The third and fourth modes involve the lateral stiffness of the springs as the sign of the rotation and translation of each mass is now opposite, so that the displacement of the constrained point is now the sum of the y translation and of $\theta\, d_A$ term (i.e., $y_A - \theta_A d_A$). The y translation depends on the lateral stiffness of the springs that is much higher than the torsional stiffness. The first two modes are analyzed in detail in the following.

Parametric Analysis

K_y influence

The following plots show the variation of the first and second natural frequencies as k_y varies. In each plot the components of the eigenvector is also plotted.

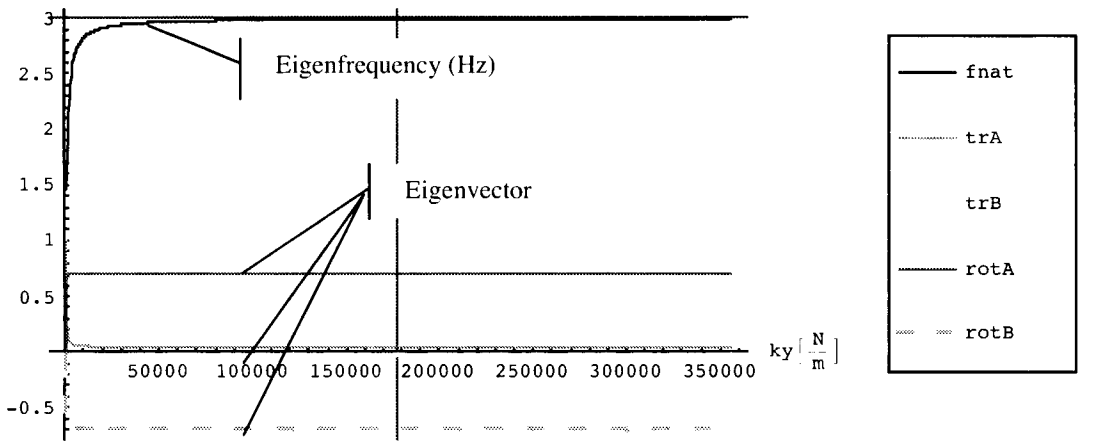

Figure 11 Dependence of first natural frequency on k_y

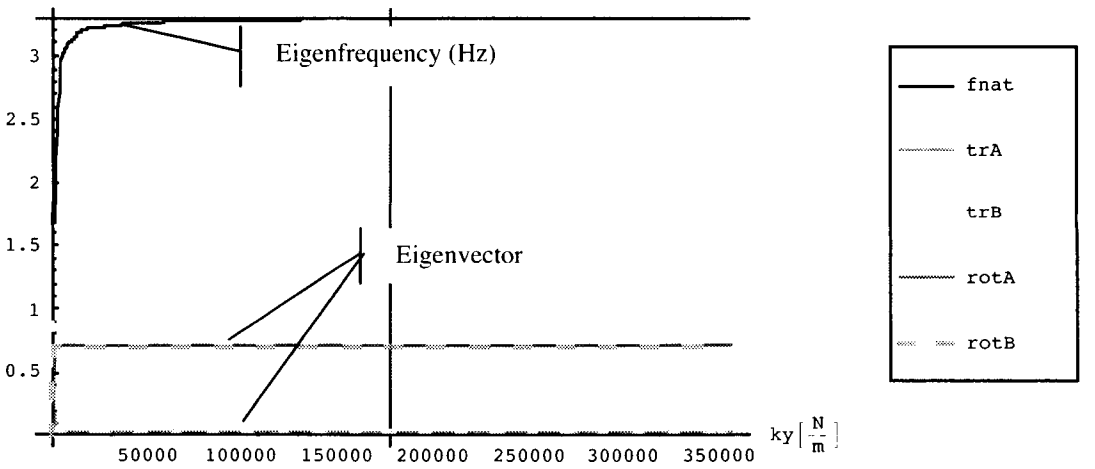

Figure 12 Dependence of second natural frequency on k_y

In the previous plots we can notice that the natural frequencies increase with k_y, having as asymptotes 2.99 and 3.29 Hz respectively. Increasing the value of k_y therefore contributes to separating the two frequencies up to the value of 0.3 Hz. The following plot shows the influence of k_y on the displacement of the constrained point.

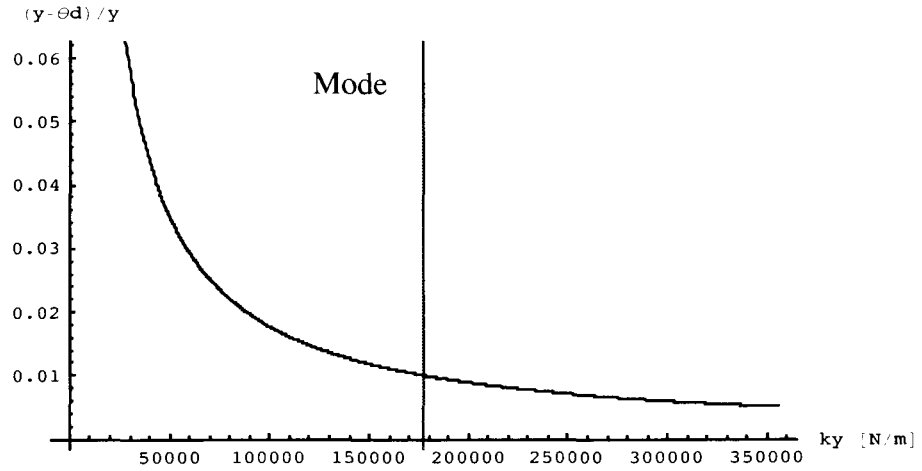

Figure 13 Dependence on k_y of translation of constrained point in first mode

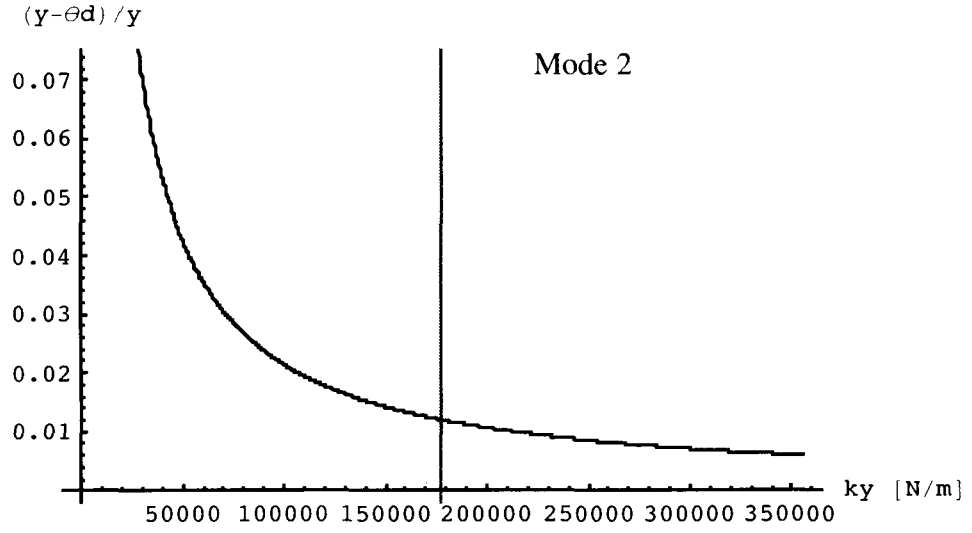

Figure 14 Dependence on k_y of translation of constrained point in second mode

It can be seen that as k_y increases, the displacement of the point S (constrained point) decreases, so that the differential displacement in mode 1 is reduced. Also for mode 2 the same behavior can be noticed below.

I_C influence

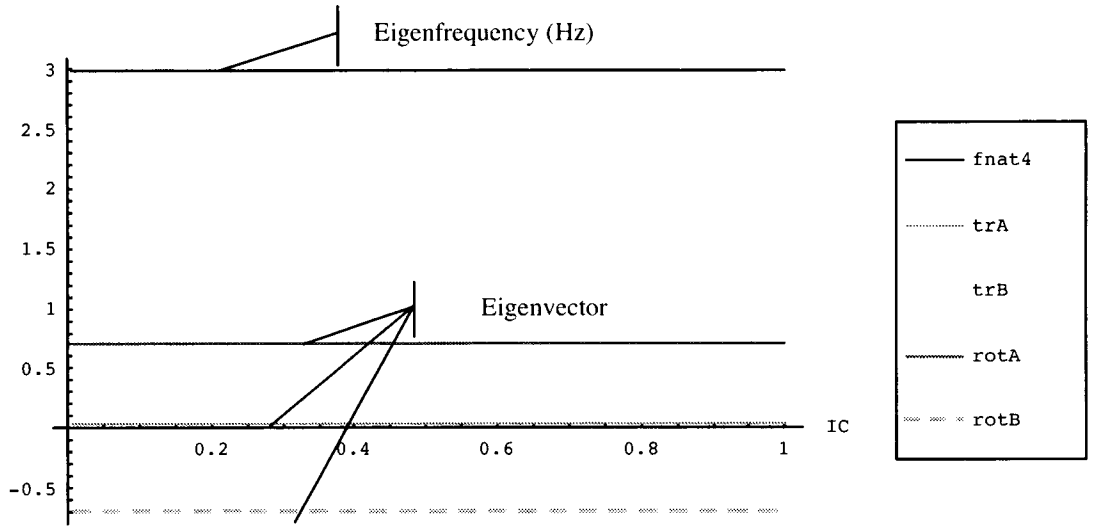

Figure 15 Dependence of first natural frequency on I_C

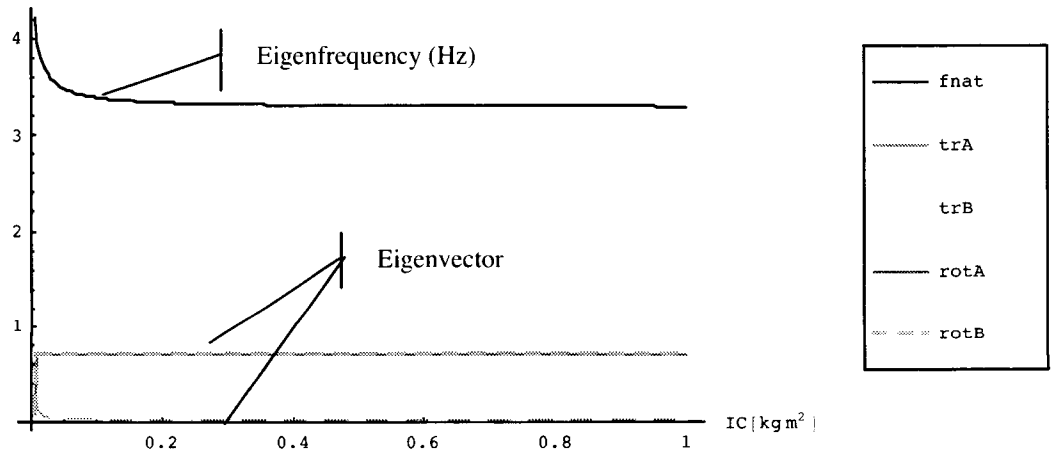

Figure 16 Dependence of second natural frequency on I_C

The influence of I_C is reflected in the frequency of the second mode; decreasing the value of I_C the natural frequency increases, yielding also to a larger separation between the two first frequencies. It can be observed that the separation of the frequencies decreases as I_C increases, having as asymptote the value of separation of 0.3 Hz, corresponding to the separation provided only by k_y for the specified k_y and m_C. I_C has no influence on the displacement of the pivot point.

m_C influence

The effect of m_C on the frequencies considered is to increase the separation of the frequencies as m_C decreases, similarly to the effect of I_C. The plot below shows this effect versus the m_C/m_A ratio.

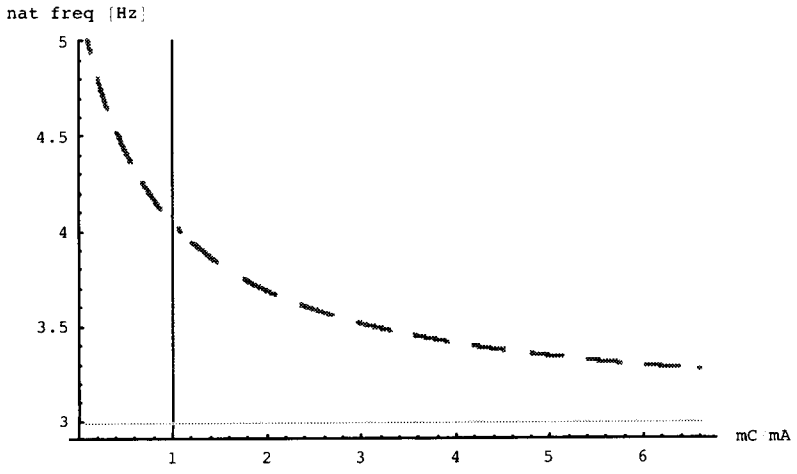

Figure 17 Dependence of natural frequency separation on m_C/m_A

Combining the effect of I_C and m_C, the separation of the frequencies increases from a value of 0.3 Hz when I_C and m_C are much greater than I_A and m_A, to a value of 2.17 Hz when the ratios I_C/I_A approaches unity.

Relative variation of I_A, m_A, k_{yA}, k_{tA}

The parameters k_{yA}, I_A, k_{tA}, d_A, m_A are now varied between the two sensing masses so to test the influence of possible imperfections in the mechanical and physical characteristics of the sensing masses and springs. The ratios p_A/p_B, where "p" indicates one of the above mentioned parameters have been varied between ±5% of the nominal value.

The main influence of these parameters is on the difference of displacement of the two sensing masses in the common mode (mode 2), resulting in a differential displacement that is detected. The plot below shows the differential displacement $(y_A - y_B)/y_A$ versus the p_A/p_B ratio.

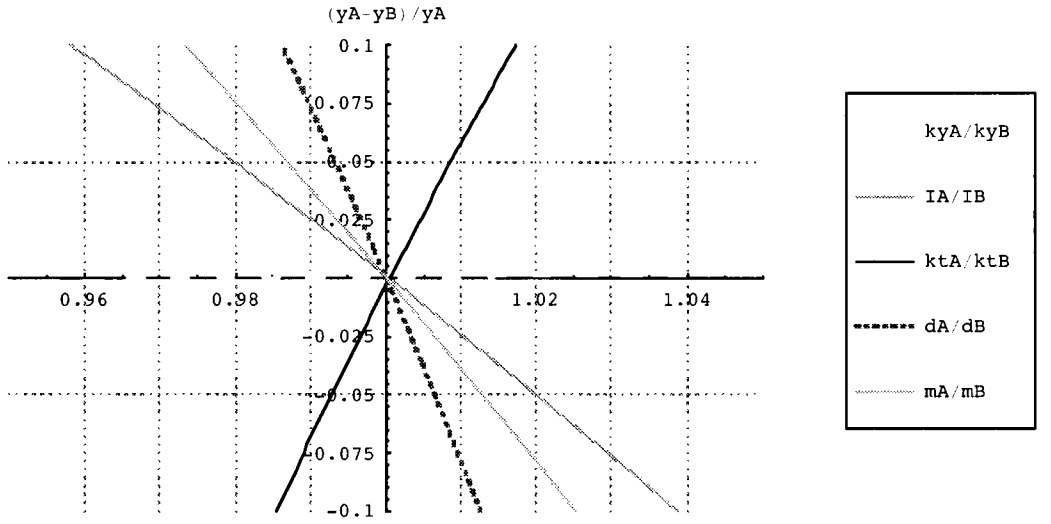

Figure 18 Influence of bodies A and B parameter's ratio on the differential displacement

As it can be seen, the most influent parameter is the distance of the constrained point, and subsequently the mass, and inertia ratio. This kind of dependence is explained by the fact that d_A changes the moment of inertia around the constrained axis with a squared dependence; m_A influences both the translational and the rotational motion, while I_A affects only the rotational DoF.

Concluding Remarks

The analysis performed allowed to describe the differential accelerometer's modes and frequencies and their dependence on the inertial and mechanical parameters. The system has been modeled using 6 DF, the rotation around the x axis and the translation along a radial axis for each body.

The first two frequencies and eigenvectors have been analyzed in detail because these modes of rotation around the pivot point affect the acceleration measurement the most. The separation of these two frequencies depends mostly on the mass and inertia moment of the C body, and slightly on the lateral stiffness of the springs. The lower C mass and inertia are, the more the first two frequencies are separated (if $I_C/I_A = 1 = m_C/m_A$ the difference is 2.17 Hz for a value of $k_y = 18000\pi^2$, while it is only 0.3 Hz if $I_C/I_A = 110$ and $m_C/m_A = 6$); increasing k_y contributes to reducing the displacement of the constrained point both for mode 1 and mode 2.

A relative variation of the parameters ratio between body A and B has then been performed, to evaluate the influence of possible imperfections of the inertial and mechanical characteristics of the testing masses.

The differential displacement of the CM of the sensing masses has been analyzed. The k_{tA}/k_{tB} ratio is the most influent, causing a Δy difference of 5% as the previous ratio varies by 0.7%. The k_{yA}/k_{tB} ratio has the same influence. The ratio m_A/m_B has roughly half the influence of the spring stiffness ratio, causing a 5% Δy as the ratio varies by 1.3%. The inertia ratio I_A/I_B produces a 5% variation in the y differential displacement as it varies by 2% from the unit value. Finally the lateral stiffness ratio k_{yA}/k_{yB} has a negligible influence compared to the others, i.e., approximately two orders of magnitude less, reaching a 0.025% Δy as the ratio varies by 1%.

DYNAMICS ANALYSIS OF INSTRUMENT PACKAGE/DETECTOR

Introduction

The following analysis is a study of the accelerometer and instrument package dynamics. Two different designs of sensor have been taken into consideration as follows: (1) a sensor with two sensing masses and a case (three bodies); and (2) a sensor with one sensing mass (made of two different materials) and a case. In both types the measurement is carried out by monitoring the differential displacements between masses, through the measurement of capacitance variations caused by those displacements.

In this study we derive the differential equations of motion for each sensor and carry out numerical integrations of cases of interest, starting from different initial conditions of the positions of the centers of mass (CM) and initial rotational velocities of the bodies in order to evaluate the influence of those parameters on the differential output of the accelerometer.

Each body is defined using all its six degrees of freedom (dof) and elastic forces and torques are applied to each of them at the attachment points of the constraining springs.

Description of sensor configurations

Three-body sensor.

The sensor is composed by two sensing masses having the CM coincident with the CM of the external case. One mass has a dumbbell shape, while the other is a hollow cylinder. These two masses are constrained to the case by means of elastic springs, having a pivot axis that is parallel to the longitudinal axis of symmetry of the sensor. All the bodies are spun about the symmetry axis x. Figure 20 shows a schematic of the 3-body sensor.

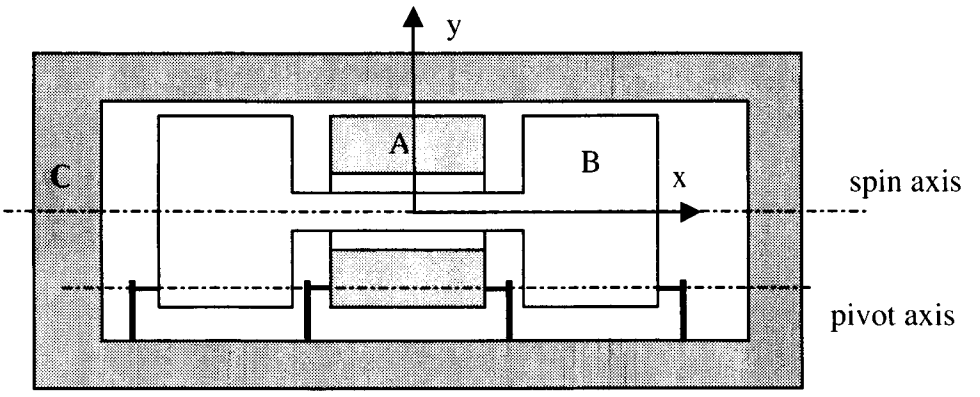

Figure 19 Schematic of three-body sensor

The motion of the sensor is essentially a rotation of the sensing masses about the pivot axis. The translational motion of the sensing masses, which depends on the high lateral stiffness of the springs is much smaller than the rotational motion. A rotation of the mass implies a variation of the distance between the sensing mass and the external case that changes the output capacitance.

Two-body sensor.

The two bodies sensor consists of an external case (body A) and an internal sensing mass. The internal mass is actually formed by two equal masses of different materials which are rigidly attached so as to behave like a single rigid body. The internal mass is connected to the external mass by means of elastic springs which have a lateral stiffness much higher than the torsional one. All the bodies are spun about the symmetry axis x.

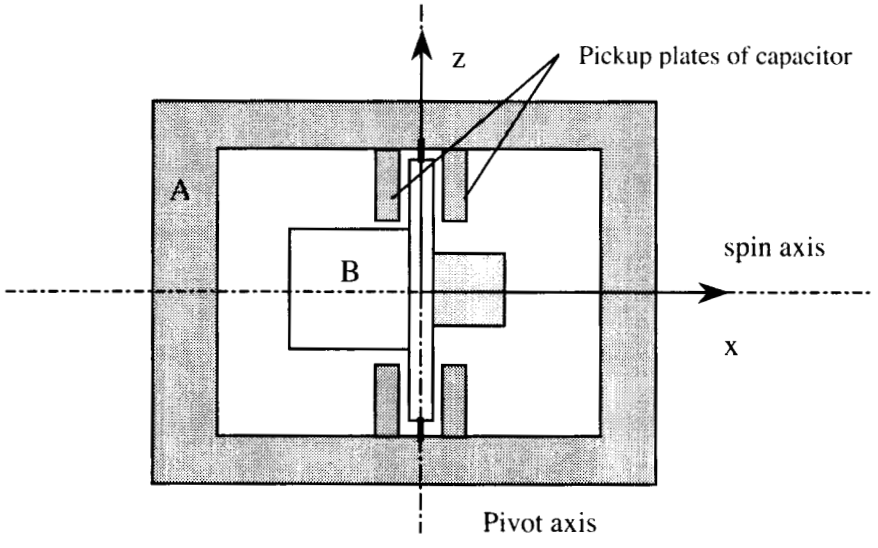

Figure 20 Schematic of two-body sensor

A violation of the EP during the fall would cause a rotation about the pivot axis of the sensing mass with respect to the sensor case. The measurement is then carried out by detecting the differential displacement (and therefore the capacitance variation) of the central disk of body B with respect to the four fixed capacitor plates attached to body A (see Fig. 21). The capacitor plates are arranged in such a way that a rotation of B about the pivot axis z unbalances the capacitive measurement bridge and produce an output signal.

Reference frames

A body reference frame has been attached to each body. The attitude of each body is identified by Euler's angles, following the sequence 1-2-3 (i.e. by building the rotation matrix using sequential rotations about x, y, and z axes).

The relationships between the different reference frames have been written by means of rotation matrices and translation vectors. All the matrices are described in details in the following. The R_{0A} matrix transforms the inertial frame (X_0, Y_0, Z_0) into the body A reference frame (X_A, Y_A, Z_A);

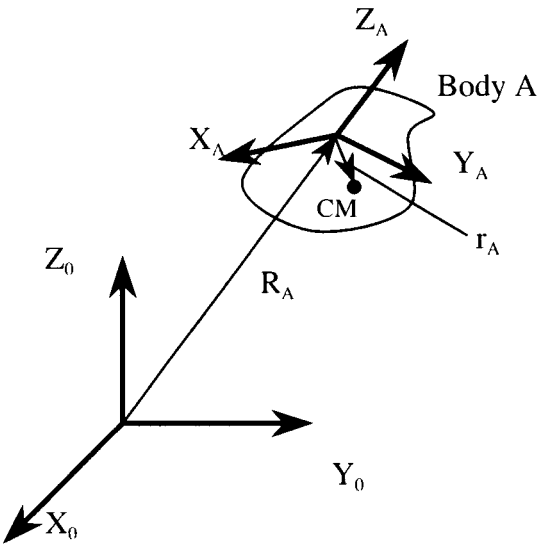

Figure 21 Inertial and body reference frames

The body frame is attached to the geometrical center of the body which, in ideal conditions, coincides with the CM of the body. The position of the CM (of body A for example) in the A reference frame is defined by $\{x_{CMA}, y_{CMA}, z_{CMA}\}$. The coordinates of the origin of the A frame (R_A) with respect to the inertial 0 frame are: $\{x_A(t), y_A(t), z_A(t)\}$.

The matrix yielding the transformation from system X_0, Y_0, Z_0 to X_A, Y_A, Z_A is composed by the following sequence of transformations:

- rotation $\theta_{xA}(t)$ around X axis;

- rotation $\theta_{yA}(t)$ around Y' axis (transformed Y_0 axis after $\theta_{xA}(t)$ rotation);

- rotation $\theta_{zA}(t)$ around Z'' axis (transformed Z_0 axis after $\theta_{xA}(t)$ and $\theta_{yA}(t)$ rotations);

- translation R_A projected along the three axes X_A, Y_A, Z_A.

The rotation matrix $[R_{0A}]$ and the translation vector $\{R_A\}$ from system 0 (inertial) to system A (body A) are the following:

$$[R_{0A}] = \begin{bmatrix} c(\theta_{yA})c(\theta_{zA}) & c(\theta_{zA})s(\theta_{xA})s(\theta_{yA}) + c(\theta_{xA})s(\theta_{zA}) & -c(\theta_{xA})c(\theta_{zA})s(\theta_{yA}) + s(\theta_{xA})s(\theta_{zA}) \\ -c(\theta_{yA})s(\theta_{zA}) & c(\theta_{xA})c(\theta_{zA}) - s(\theta_{xA})s(\theta_{yA})s(\theta_{zA}) & c(\theta_{zA})s(\theta_{xA}) + c(\theta_{xA})s(\theta_{yA})s(\theta_{zA}) \\ s(\theta_{yA}) & -c(\theta_{yA})s(\theta_{xA}) & c(\theta_{xA})c(\theta_{yA}) \end{bmatrix}$$

where the superscript identifies the relevant reference frame. The translation vector is the R_A vector, expressed in the A frame. This vector can be computed as follows:

$$R_A = [R_{0A}] \{-x_A \ -y_A \ -z_A\}^T$$

Where the vector $\{-x_A, -y_A, -z_A\}$ is the opposite of the vector $\{R_A\}$ expressed in the 0 frame.

We have:

$$\left\{R_A{}^A\right\} = \begin{Bmatrix} -c(\theta_{yA})c(\theta_{zA}).x_A - [c(\theta_{zA})s(\theta_{xA})s(\theta_{yA}) + c(\theta_{xA})s(\theta_{zA})]y_A + [c(\theta_{xA})c(\theta_{zA})s(\theta_{yA}) - s(\theta_{xA})s(\theta_{zA})]z_A \\ c(\theta_{yA})s(\theta_{zA}).x_A - [c(\theta_{xA})c(\theta_{zA}) - s(\theta_{xA})s(\theta_{yA})s(\theta_{zA})]y_A - [c(\theta_{zA})s(\theta_{xA}) + c(\theta_{xA})s(\theta_{yA})s(\theta_{zA})]z_A \\ -s(\theta_{yA}).x_A + c(\theta_{yA})s(\theta_{xA})y_A - c(\theta_{xA})c(\theta_{yA})z_A \end{Bmatrix}$$

For the opposite transformation, which leads from the body A coordinate system to the inertial frame, we use the transpose of the rotation matrix $[R_{A0}] = [R_{0A}]^T$ and the vector is simply the R_A vector expressed in the inertial coordinates $\{x_A, y_A, z_A\}$.

We have

$$[R_{A0}] = \begin{bmatrix} c(\theta_{xA})c(\theta_{yA}) & -c(\theta_{yA})s(\theta_{xA}) & s(\theta_{yA}) \\ c(\theta_{zA})s(\theta_{xA}) + c(\theta_{xA})s(\theta_{yA})s(\theta_{zA}) & c(\theta_{xA})c(\theta_{zA}) - s(\theta_{xA})s(\theta_{yA})s(\theta_{zA}) & -c(\theta_{yA})s(\theta_{zA}) \\ -c(\theta_{xA})c(\theta_{zA})s(\theta_{yA}) + s(\theta_{xA})s(\theta_{zA}) & c(\theta_{zA})s(\theta_{xA})s(\theta_{yA}) + c(\theta_{xA})s(\theta_{zA}) & c(\theta_{yA})c(\theta_{zA}) \end{bmatrix}$$

$$\left\{R_A^0\right\} = \begin{Bmatrix} x_A \\ y_A \\ z_A \end{Bmatrix}$$

In summary, we have the following transformations:

Inertial to body A:

$[R_{0A}].\{r^0\} + \{R_A{}^A\}$

Body to inertial:

$[R_{A0}]. \{r^A\} + \{R_A{}^0\}$

The same procedure is followed for the other bodies.

Degrees of Freedom and equations of motion

To determine the equation of motion for the different bodies the transformation matrices have been written for each body. The body coordinate systems are centered in the body's geometrical center, and fixed with the body itself. The position of the CM is described using three coordinates (x_{CMA}, y_{CMA}, z_{CMA} for body A). Each system has the x axis along the longitudinal axis of symmetry, corresponding also to the spin axis, the y and z axes are radial axes rotating with the body.

Each body has all the six degrees of freedom, i.e. the three translations of the body frame origin, and the three rotations according to the Euler's angles described above.

To derive the equations of motion the translation accelerations of the CM and elastic forces have been written in the inertial system. The rotational equations are then projected onto the body axes.

Translational accelerations

In the following we describe the procedure for deriving the equations of motion by taking the two-body sensor as an example. The procedure to derive the equations for the three-body sensor is exactly the same with the added complexity of a higher number of equations.

The CM vector in each body's reference frame is:

Body A: $\{r_A\} = \{x_{CMA}\ y_{CMA}\ z_{CMA}\}^T$

Body B: $\{r_B\} = \{x_{CMB}\ y_{CMB}\ z_{CMB}\}^T$

The translational acceleration expressed in the inertial reference is obtained using the formula:

$$\{a_A\} = \left[\ddot{R}_{A0}\right]\cdot\{r_A\} + 2\left[\dot{R}_{A0}\right]\cdot\{\dot{r}_A\} + \left[R_{A0}\right]\cdot\{\ddot{r}_A\} + \left\{\ddot{R}_A^0\right\}$$

Where

$\{a_A\}$ is the acceleration of body A in the inertial frame;

$[R_{A0}]$ is the rotation matrix from A to inertial frame;

$\{r_A\}$ is the coordinates vector of body A CM in the A frame;

$\{R_A^0\}$ is the translation vector expressed in inertial coordinates

$(\dot{})$ indicates the time derivative and the dot (.) matrix multiplication.

The same equations are used for the other bodies.

Elastic Forces

To evaluate the elastic forces we define first the points where the springs are attached to each body. The position of these points are expressed in body frame. The distance between connected points is then computed from the actual position during the motion, projected in the A frame, and multiplied by the stiffness vector $\{k_{xA}, k_{yA}, k_{zA}\}$. By following this procedure, it is possible to assign different stiffness to each degree of freedom. Finally the elastic forces are projected in the inertial coordinate system, and added to the equation of motion. The points connected by the springs are as follows (all distances are in meters):

$$\{p_{A1}\} = \{0, 0, -75x10^{-3}\}^T$$

$$\{p_{A2}\} = \{0, 0, 75x10^{-3}\}^T$$

$$\{p_{B1}\} = \{0, 0, -65x10^{-3}\}^T$$

$$\{p_{B2}\} = \{0, 0, 65x10^{-3}\}^T$$

The initial lengths of the two springs constraining the motion are as follows:

$$\{l_1\} = \{p_{A1} - p_{B1}\} = \{0, 0, -10x10^{-3}\}^T$$

$$\{l_2\} = \{p_{A2} - p_{B2}\} = \{0, 0, 10x10^{-3}\}^T$$

The figure below shows the position of the points where the forces are applied

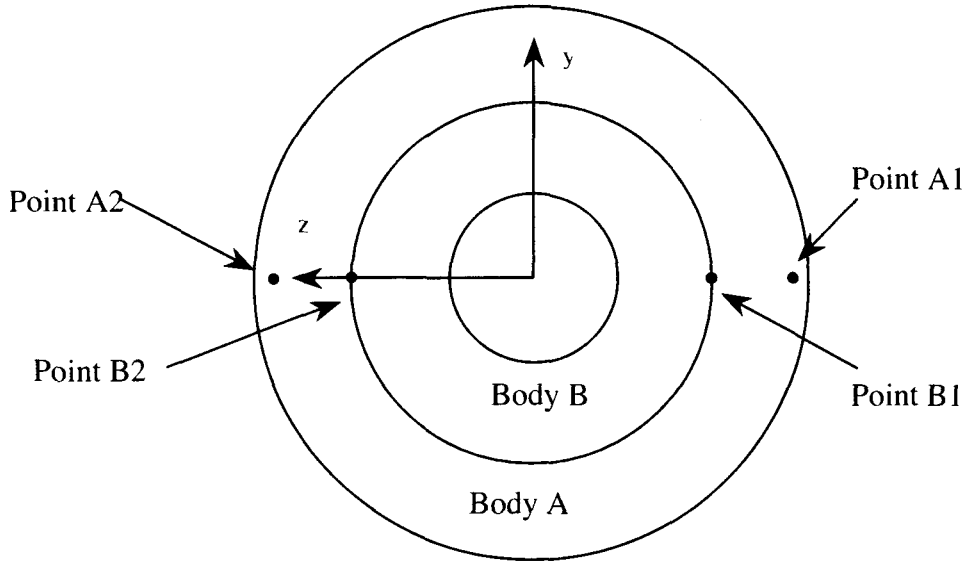

Figure 22 Locations of attachment points

$$\{F_{1A}\} = [R_{A0}] \cdot ([K] \cdot (\{p_{A1}\} - [T_{0A}].\{T_{B0}.p_{B1}\} - \{l_1\}))$$

$$\{F_{2A}\} = [R_{A0}] \cdot ([K] \cdot (\{p_{A2}\} - [T_{0A}].\{T_{B0}.p_{B2}\} - \{l_2\}))$$

$$\{F_A\} = \{F_{1A}\} + \{F_{2A}\}$$

In the above notation the operator "$T_{0A}.x$" indicates the combination of the multiplication for the rotation matrix $[R_{0A}]$ applied to the vector $\{x\}$ plus the translation of the vector $\{R_A{}^A\}$ which yields:

$$\{T_{0A}.x\} = [R_{0A}].\{x\} + \{R_A{}^A\}$$

The expression $T_{0A}.(T_{B0}.p_{B1})$ projects the coordinates of the point p_{B1} (expressed in the body B frame) onto the body A coordinate system. Subsequently, the force is projected onto the inertial frame using the $[R_{A0}]$ matrix. A similar procedure is used to evaluate the forces acting on any other body pairs.

The equations of translational motion for the two bodies A and B are:

$$m_A \{a_A\} - \{F_A\} = 0$$

$$m_B \{a_B\} - \{F_B\} = 0$$

where m_A and m_B are the masses of body A and B, a_A and a_B are the accelerations, and F_A and F_B are the elastic forces:

$$\{F_A\} = \{F_{1A}\} + \{F_{2A}\}$$

$$\{F_B\} = \{F_{1B}\} + \{F_{2B}\}.$$

Rotational accelerations:

The angular velocity of each body is computed by using the rotation matrices that transform the coordinate system from the inertial to the body frame and conversely for the opposite transformation. The rotational velocity matrices of bodies A and B are derived by using the Cartan's formula as follows:

$$[\omega_A] = [R_{0A}] \cdot [\dot{R}_{A0}]$$

$$[\omega_B] = [R_{0B}] \cdot [\dot{R}_{B0}]$$

where $[R_{0A}]$ and $[R_{A0}]$ are the rotation matrices from coordinate system 0 to A and vice-versa. $[R_{0B}]$ and $[R_{B0}]$ are the correspondent matrices for body B.

It should be noted that the former expression lead to the skew symmetric matrix of the angular velocity from which the components of the angular velocity vector $\{\omega_A\}$ can be readily extracted.

The rotational inertia forces are obtained using the formulas:

$$[I_A]\cdot\{\dot{\omega}_A\}+[\omega_A]\cdot[I_A]\cdot\{\omega_A\}$$

$$[I_B]\cdot\{\dot{\omega}_B\}+[\omega_B]\cdot[I_B]\cdot\{\omega_B\}$$

Where $\{\omega_A\}$ and $[\omega_A]$ represent the angular velocity vector and matrix, respectively, for body A (and similarly for body B), $[I_A]$ and $[I_B]$ are the inertia matrices for body A and B which, assuming principal axes, have the form

$$[I_A]=\begin{bmatrix} I_{Axx} & 0 & 0 \\ 0 & I_{Ayy} & 0 \\ 0 & 0 & I_{Azz} \end{bmatrix};\quad [I_B]=\begin{bmatrix} I_{Bxx} & 0 & 0 \\ 0 & I_{Byy} & 0 \\ 0 & 0 & I_{Bzz} \end{bmatrix}$$

Elastic torques

The elastic torques acting on each body are computed by using the definition of the attachment points and the expression of the elastic forces previously defined. The expressions of the torques in the body reference frame are the following:

$$\{T_A\} = \{p_{A1}\} \times ([R_{0A}] . \{F_{1A}\}) + \{p_{A2}\} \times ([R_{0A}] . \{F_{2A}\})$$

$$\{T_B\} = \{p_{B1}\} \times ([R_{0B}] .\{F_{1B}\}) + \{p_{B2}\} \times ([R_{0B}] . \{F_{2B}\})$$

where $\times$ indicates the external product of vectors.

The expressions of the rotational equations of motion are finally:

$$\begin{aligned} &[I_A]\cdot\{\dot{\omega}_A\}+[\omega_A]\cdot[I_A]\cdot\{\omega_A\}-\{T_A\}=0 \\ &[I_B]\cdot\{\dot{\omega}_B\}+[\omega_B]\cdot[I_B]\cdot\{\omega_B\}-\{T_B\}=0 \end{aligned} \qquad (\ )$$

The equations of motion for the three bodies sensor are evaluated at the same way as for the two bodies. The same quantities are derived and the same structure for the equations is followed. The following figure shows the positions of the constrained points for the three bodies sensor.

The points p_{CA1}, p_{CA2}, p_{CB1} and p_{CB2} are the points of the external case C connected with the points p_{A1}, p_{A2}, p_{B1}, p_{B2}, respectively. In this case four springs are used to connect the two bodies to the case (two springs per each body).

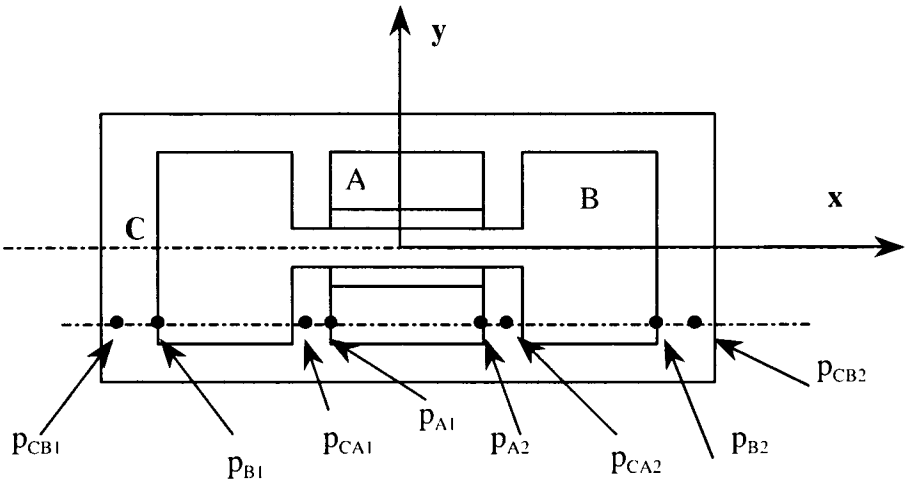

Figure 23 Locations of attachment points

The coordinates of the points are the following (each point is expressed in its own body system):

$\{p_{A1}\} = \{-40x10^{-3}, -60x10^{-3}, 0\}^T$

$\{p_{B1}\} = \{-250x10^{-3}, -60x10^{-3}, 0\}^T$

$\{p_{CA1}\} = \{-50x10^{-3}, -60x10^{-3}, 0\}^T$

$\{p_{CB1}\} = \{-270x10^{-3}, -60x10^{-3}, 0\}^T$

$\{l_{A1}\} = \{p_{A1} - p_{CA1}\}$

$\{l_{B1}\} = \{p_{B1} - p_{CB1}\}$

$\{p_{A1}\} = \{40x10^{-3}, -60x10^{-3}, 0\}^T$

$\{p_{B1}\} = \{250x10^{-3}, -60x10^{-3}, 0\}^T$

$\{p_{CA1}\} = \{50x10^{-3}, -60x10^{-3}, 0\}^T$

$\{p_{CB1}\} = \{270x10^{-3}, -60x10^{-3}, 0\}^T$

$\{l_{A2}\} = \{p_{A2} - p_{CA2}\}$

$\{l_{B2}\} = \{p_{B2} - p_{CB2}\}$

Two Bodies

The integration of the equations of motion has been performed using different values for the CM position and initial angular velocity of body A.

A frequency analysis has been performed for each result, to evaluate the frequency content of the differential rotation around the z axis, which leads to the detection of a differential signal by the capacitors.

The parameters in the equations are the following:

m_A = mass of body A
m_B = mass of body B
I_{Ax} = moment of inertia of body A about the x axis
I_{Ay} = moment of inertia of body A about the y axis
I_{Az} = moment of inertia of body A about the z axis
I_{Bx} = moment of inertia of body B about the x axis
I_{By} = moment of inertia of body B about the y axis
I_{Bz} = moment of inertia of body B about the z axis
k_x = lateral stiffness of spring connecting bodies A and B (in A coordinates)
k_y = lateral stiffness of spring connecting bodies A and B (in A coordinates)
k_z = lateral stiffness of spring connecting bodies A and B (in A coordinates)
$k_{\theta z}$ = torsional stiffness of spring connecting bodies A and B
x_{CMA} = x position of CM of body A (in body A coordinates)
y_{CMA} = y position of CM of body A (in body A coordinates)
z_{CMA} = z position of CM of body A (in body A coordinates)
x_{CMB} = x position of CM of body B (in body B coordinates)
y_{CMB} = y position of CM of body B (in body B coordinates)
z_{CMB} = z position of CM of body B (in body B coordinates)

The variables for the equations (dof) are:

$x_A(t)$ = x coordinate of the geometrical center of body A (in inertial coordinates)
$y_A(t)$ = y coordinate of the geometrical center of body A (in inertial coordinates)
$z_A(t)$ = z coordinate of the geometrical center of body A (in inertial coordinates)
$x_B(t)$ = x coordinate of the geometrical center of body B (in inertial coordinates)
$y_B(t)$ = y coordinate of the geometrical center of body B (in inertial coordinates)
$z_B(t)$ = z coordinate of the geometrical center of body B (in inertial coordinates)
$\theta_{xA}(t)$ = x rotation of body A
$\theta_{yA}(t)$ = y rotation of body A
$\theta_{zA}(t)$ = z rotation of body A
$\theta_{xB}(t)$ = x rotation of body A
$\theta_{yB}(t)$ = y rotation of body A
$\theta_{zB}(t)$ = z rotation of body A

Numerical values have been assigned to the parameters and then a study of the influence of the position of the CM with respect to the geometrical center of each body (CM parameters), also combined with an initial angular velocity of body B. The values used for the fixed parameters are in the following.

We analyze in the following representative cases with prograde precession (i.e., ICx > ICy). The reason for favoring prograde precession over retrograde precession is that prograde precession brings about significantly smaller accelerations due to imperfect release (see later on) than retrograde precession.

Two-Body Dynamics Simulation

Prograde precession

mA = 30 kg, mB = 1 kg,
IAx = 95/100 kgm^2, IAy = 146/100 kgm^2, IAz = 146/100 kgm^2,
IBx = 17/100, IBy = 17/100, IBz = 17/100,
kx = 45000 N/m, ky -> 35000 N/m, kz -> 35000 N/m,
kx2 = 45000 N/m, ky2 = 35000 N/m, kz2 = 35000 N/m,
kθx = 1000 Nm/rad, kθy = 1000 Nm/rad, kθz = 54 Nm/rad;

spin frequency -> 0.3 Hz
initial vel theta z body A = 10^{-2} rad/s
initial nutation angle = 0

xCMA = 0, yCMA = 0, zCMA = 0,
xCMB = 10^{-6} m, yCMB = 0, zCMB = 10^{-6} m

$$\begin{pmatrix} 2.99716 \\ 7.38688 \\ 8.08957 \\ 42.8045 \\ 42.8045 \\ 48.5357 \end{pmatrix}$$

Figure 24 Natural frequencies

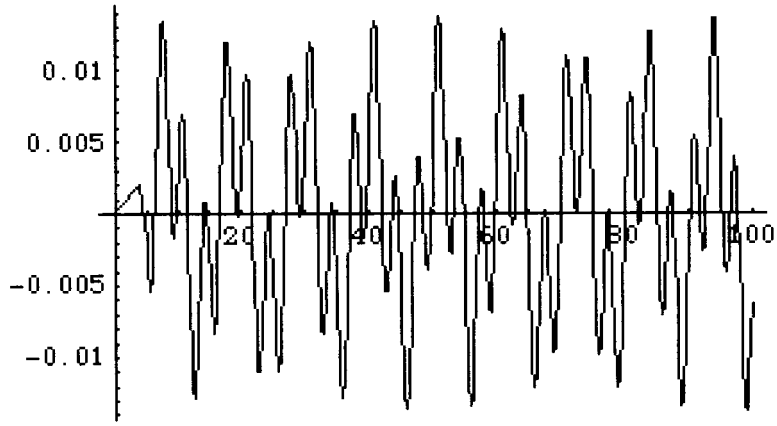

Figure 25 θ_{zA} (rad) vs. time (s)

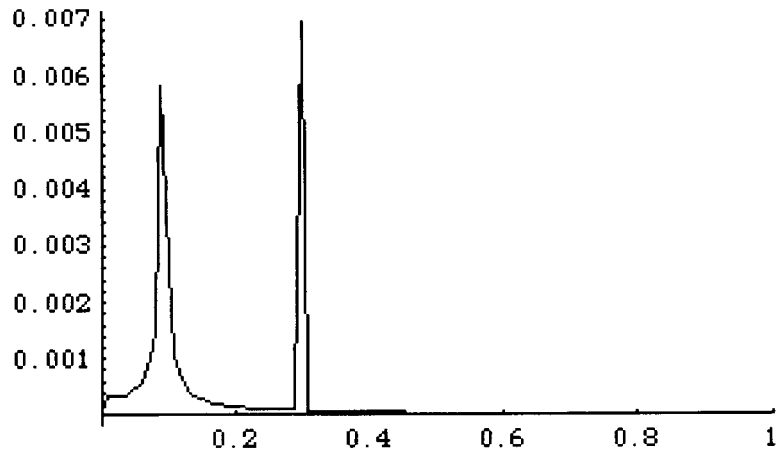

Figure 26 FFT of θ_{zA} vs. frequency (Hz)

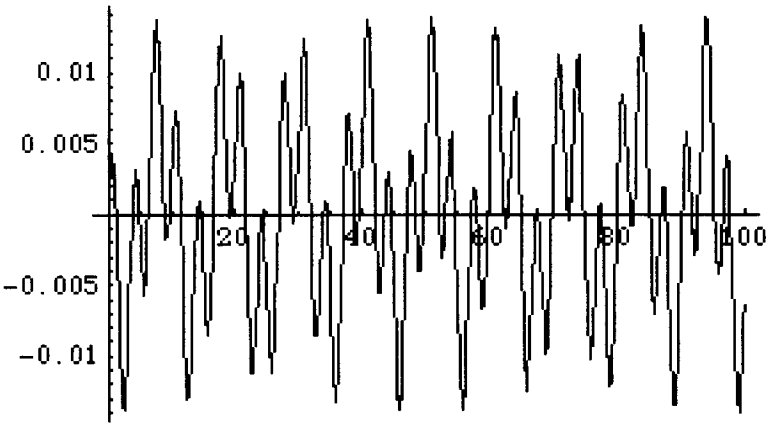

Figure 27 θ_{zB} (rad) vs. time (s)

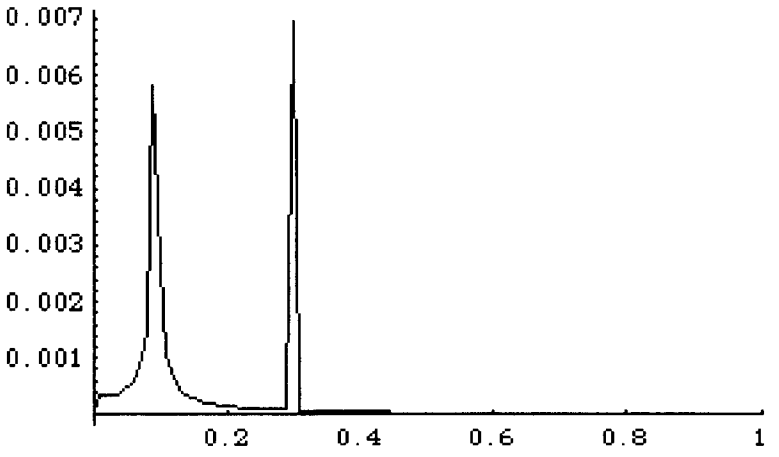

Figure 28 FFT of θ_{zA} vs. frequency (Hz)

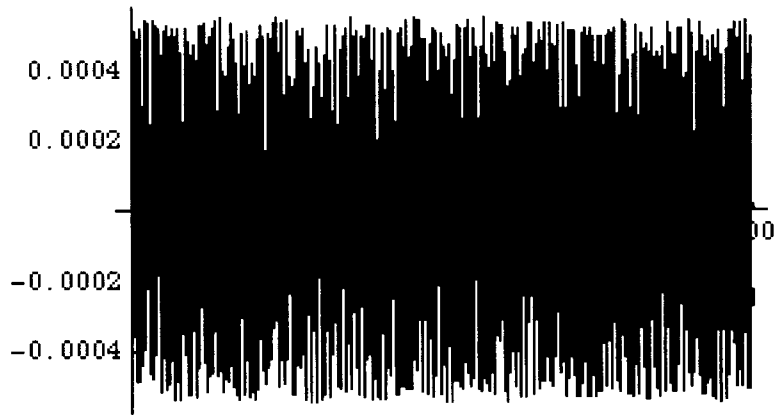

Figure 29 θ_{zB} - θ_{zA} (rad) vs. time (s)

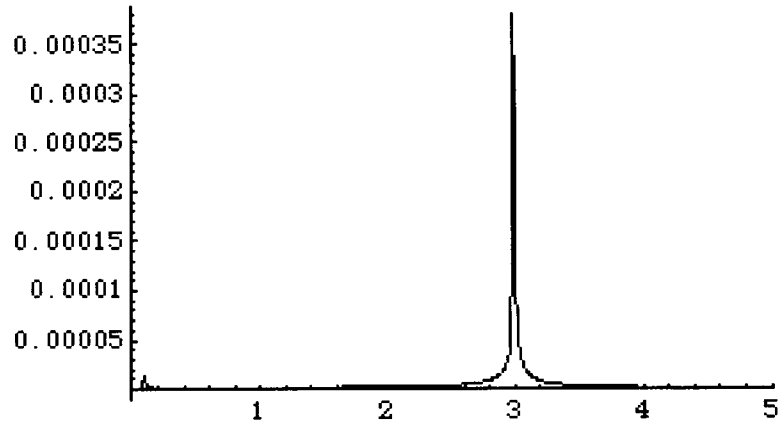

Figure 30 FFT of θ_{zB} - θ_{zA} vs. frequency (Hz)

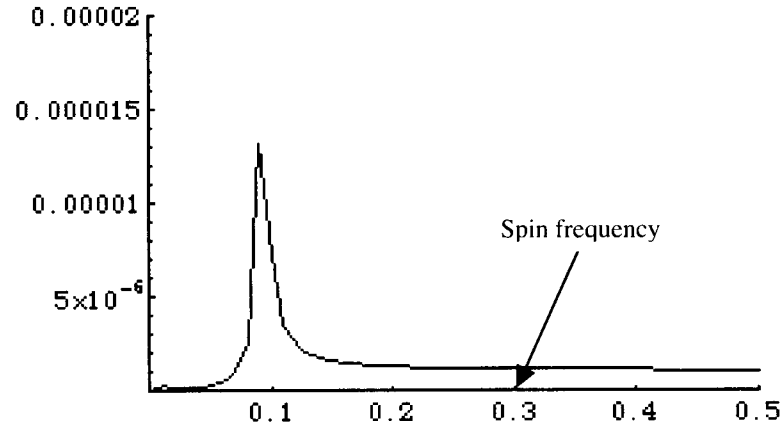

Figure 31 Zoom of θ_{zB} - θ_{zA} FFT vs. frequency (Hz)

Three Body Dynamics Simulations

The parameters in the equations are the following:

m_A = mass of body A
m_B = mass of body B
m_C = mass of body C
I_{Ax} = moment of inertia of body A about the x axis
I_{Ay} = moment of inertia of body A about the y axis
I_{Az} = moment of inertia of body A about the z axis
I_{Bx} = moment of inertia of body B about the x axis
I_{By} = moment of inertia of body B about the y axis
I_{Bz} = moment of inertia of body B about the z axis
I_{Cx} = moment of inertia of body C about the x axis
I_{Cy} = moment of inertia of body C about the y axis
I_{Cz} = moment of inertia of body C about the z axis
k_{Ax} = lateral stiffness of spring connecting bodies A and C (in C coordinates)
k_{Ay} = lateral stiffness of spring connecting bodies A and C (in C coordinates)
k_{Az} = lateral stiffness of spring connecting bodies A and C (in C coordinates)
k_{Bx} = lateral stiffness of spring connecting bodies B and C (in C coordinates)
k_{By} = lateral stiffness of spring connecting bodies B and C (in C coordinates)
k_{Bz} = lateral stiffness of spring connecting bodies B and C (in C coordinates)
$k_{\theta xA}$ = torsional stiffness of spring connecting bodies A and C
$k_{\theta xB}$ = torsional stiffness of spring connecting bodies B and C
x_{CMA} = x position of CM of body A (in body A coordinates)
y_{CMA} = y position of CM of body A (in body A coordinates)
z_{CMA} = z position of CM of body A (in body A coordinates)
x_{CMB} = x position of CM of body B (in body B coordinates)
y_{CMB} = y position of CM of body B (in body B coordinates)
z_{CMB} z position of CM of body B (in body B coordinates)
x_{CMC} x position of CM of body C (in body C coordinates)
y_{CMC} y position of CM of body C (in body C coordinates)
z_{CMC} z position of CM of body C (in body C coordinates)

The variables for the equations (dof) are:

$x_A(t)$ = x coordinate of the geometrical center of body A (in inertial coordinates)
$y_A(t)$ = y coordinate of the geometrical center of body A (in inertial coordinates)
$z_A(t)$ = z coordinate of the geometrical center of body A (in inertial coordinates)
$x_B(t)$ = x coordinate of the geometrical center of body B (in inertial coordinates)
$y_B(t)$ = y coordinate of the geometrical center of body B (in inertial coordinates)
$z_B(t)$ = z coordinate of the geometrical center of body B (in inertial coordinates)
$x_C(t)$ = x coordinate of the geometrical center of body C (in inertial coordinates)
$y_C(t)$ = y coordinate of the geometrical center of body C (in inertial coordinates)
$z_C(t)$ = z coordinate of the geometrical center of body C (in inertial coordinates)
$\theta_{xA}(t)$ = x rotation of body A

$\theta_{yA}(t)$ = y rotation of body A
$\theta_{zA}(t)$ = z rotation of body A
$\theta_{xB}(t)$ = x rotation of body A
$\theta_{yB}(t)$ = y rotation of body A
$\theta_{zB}(t)$ = z rotation of body A
$\theta_{zC}(t)$ = z rotation of body C
$\theta_{xC}(t)$ = x rotation of body C
$\theta_{yC}(t)$ = y rotation of body C

Prograde precession

ICx > ICy
spin freq = 0.3 Hz

values:

mA = 1 kg, mB = 1 kg, mC = 30 kg,
IAx = 17/100 kgm^2, IAy = 17/100 kgm^2, IAz = 17/100 kgm^2,
IBx = 17/100 kgm^2, IBy = 17/100 kgm^2, IBz = 17/100 kgm^2,
ICx = 95/100 kgm^2, ICy = 146/100 kgm^2, ICz = 146/100 kgm^2,
kA1x = 45000 N/m, kA1y = 35000 N/m, kA1z = 35000 N/m,
kA2x = 45000 N/m, kA2y = 35000 N/m, kA2z = 35000 N/m,
kAθx = 61.68 Nm/rad, kAθy = 1000 Nm/rad, kAθz = 1000 Nm/rad,
kB1x = 45000 N/m, kB1y = 35000 N/m, kB1z = 35000 N/m,
kB2x = 45000 N/m, kB2y = 35000 N/m, kB2z = 35000 N/m,
kBθx = 6168/100 Nm/rad, kBθy = 1000 Nm/rad, kBθz = 1000 Nm/rad

initial vel theta z body C = 10^{-2} rad/s
Initial nutation angle = 0

xCMA = 10^{-6} m, yCMA = 0, zCMA = 10^{-6} m,
xCMB = 0, yCMB = 0, zCMB = 0,
xCMC = 0, yCMC = 0, zCMC = 0

$$\begin{pmatrix} 42.1084 \\ 43.4894 \\ 4.39904 \\ 27.2175 \\ 2.99982 \\ 42.5542 \\ 3.48568 \\ 44.0754 \\ 48.344 \\ 50.0619 \\ 4.34997 \\ 26.7789 \end{pmatrix}$$

Figure 32 Natural frequencies

The simulations have been run for 100 s to provide a good frequency resolution for the FFT plots.

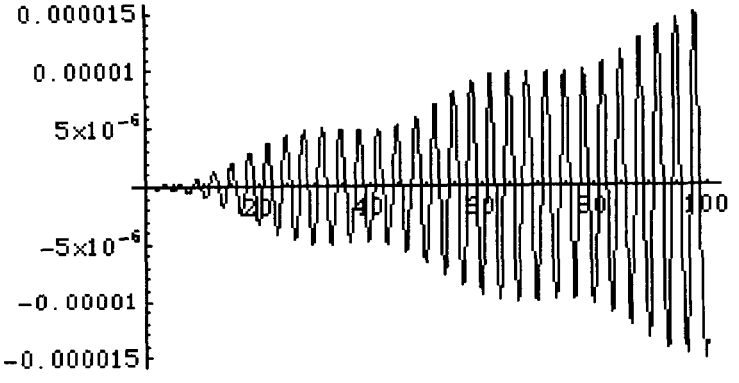

Figure 33 z_A (m) projected in body C frame vs. time (s)

Figure 34 z_A - z_C (m) projected in body C frame vs. time (s)

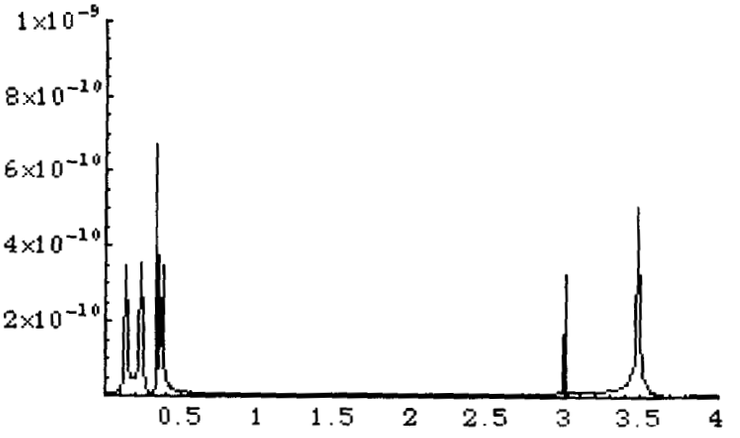

Figure 35 FFT of z_A - z_C vs. frequency (Hz)

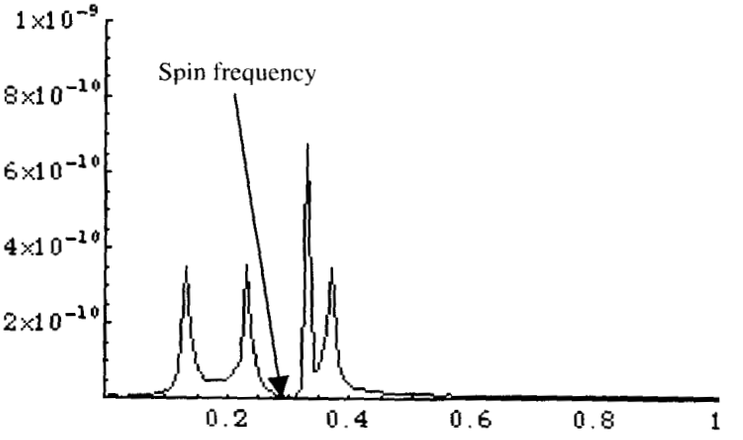

Figure 36 Zoom of z_A - z_C FFT vs. frequency (Hz)

Figure 37 z_B - z_C (m) in C frame vs. time (s)

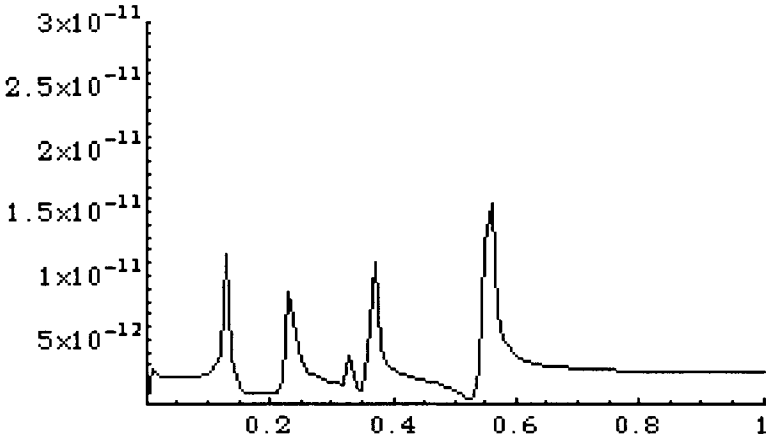

Figure 38 FFT of z_B vs. frequency (Hz)

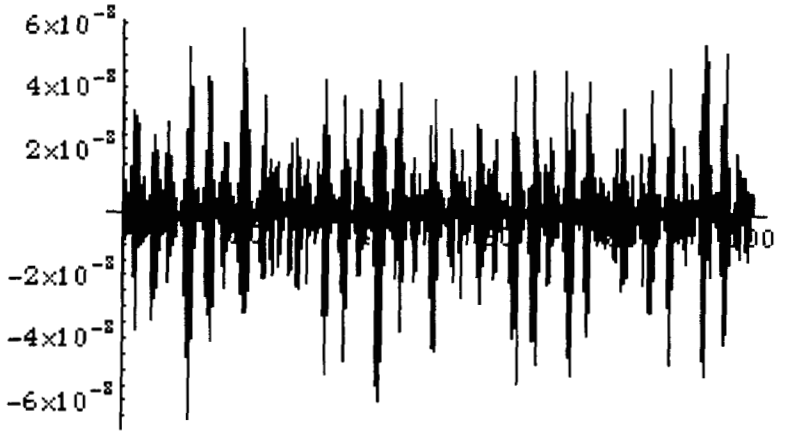

Figure 39 $z_A - z_B$ (m) in C frame vs. time (s)

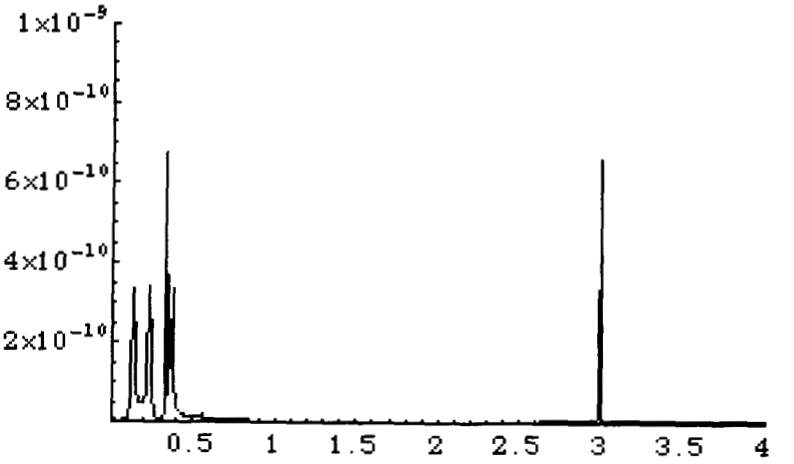

Figure 40 FFT of $z_A - z_B$ vs. frequency (Hz)

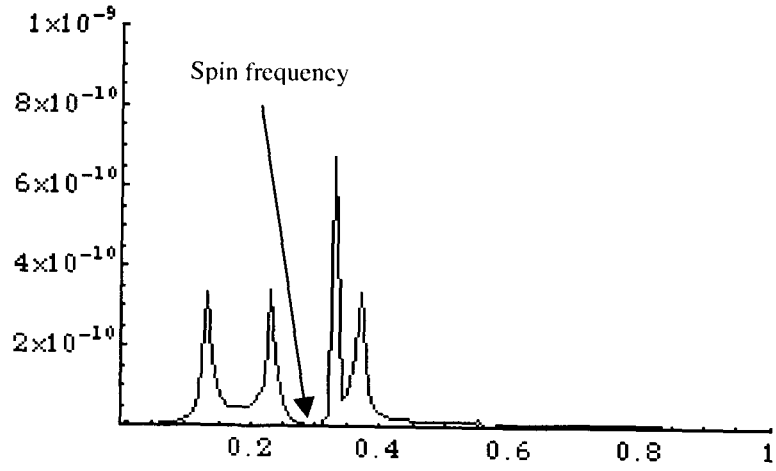

Figure 41 Zoom of z_A - z_B FFT vs. frequency (Hz)

Concluding Remarks

The analysis carried out allowed to evaluate the influence of CM position and initial angular velocity errors in the dynamic of the 2 bodies and the 3 bodies sensor. The two systems have been modeled using 12 DoF, and 18 DoF respectively (six dof for each body).

2-body results

The position of the CM for body A (external case) did not affect the rotation about the z axis (measurement axis), while the initial nonzero condition on the angular velocity of the same body caused a differential signal to be detected.

Analyzing the frequency content of the signal, though, no frequency peak was noticed at the spin frequency (0.5 Hz), while the natural frequency for the rotation about the z axis (3 Hz) and the precession frequency (0.18 Hz) were present.

These frequencies can easily be changed modifying the torsional stiffness about z axis and changing the inertia ratio (IAz - IAx)/IAz, to which the precession frequency is directly related.

It has to be noted that the spin frequency appears in the single θzA or θzB starting from an initial angular velocity of body A about y or z axes, but it is rejected when the difference between the two signals is performed.

Also combining the initial conditions together (both CM positions and angular velocities) leaded to analogous results, resulting in a rejection of the spin frequency in the differential rotation.

3-body results

Also in the case of the three bodies the position of the CM of the external case (body C) along the spin axis does not influence any of the variables; the displacement of the CM along the axes y and z cause the excitation of the y and z variables only, while the rotations are not affected. Moreover the differential displacement is not excited.

An initial condition on the angular velocity (both along the y or z directions) excites all the dof of the system, both global and differential; the frequency pattern of the variables doesn't show evidence of peaks at the spin frequency, neither in the global, nor in the differential component of the displacements.

Applying all the different conditions together again all the dof are involved, and the frequency analysis evidences that the measurement differential signal (along z direction) doesn't show any peak at the spin frequency, even if these peaks are present in other global variables (y and z) due to initial displacement of the CM of body C along y and/or z directions.

DETECTOR REQUIREMENTS DEVELOPMENT

Model for the Gravitational Perturbations Acting on Test Bodies

Overview

The test body (proof mass), falling inside the capsule, is subjected to non-negligible gravitational attraction by the capsule. In particular, the higher order gravitational potential plays a major role because of the elimination of the zero-order potential due to the equivalence principle. The model consists of a spinning test body inside a capsule: hollow cylinder covered with flat caps. The test body is released at the axis of the cylinder, and deviates from the axis during its fall. Therefore, our task is to compute the gravitational force and torque acting at the neighborhood of the fall. The fact that both the test mass and the capsule are closed finite bodies, increases the complexity of the problem. We took advantage of the size of the test mass; smaller than the cylinder radius, to derive an asymptotic analytical solution. We mostly concern with the force/torque at the modulation frequency. In other words, our model should evaluate the force/torque in a rotating body frame, rather than the static field in the capsule frame of reference. For that purpose we built a semi-analytical model. The main advantage of our model is its robustness. It can handle any configuration of test mass as well as any additional mass distribution in the test chamber.

The purpose of this work is two folds. We need a working gravitational model for future simulation for the dynamics of the test body. We also need to choose the best inertia properties of the test body, in order to minimize the gravitational disturbance.

The following report presents the analytical approach and the analytical results, and shows numerical investigations and the analysis of the results. In addition, we include few appendixes. Appendix A explains the computer code. Appendix B and C present analytical solutions for the gravitational attraction due to the cylinder and the caps, and check the validation of our numerical model. Appendix D proposes the approximation of the gravitational field and its gradient by using radial basis functions.

General Approach

The purpose of this work is to model and to analyze the gravitational attraction between the capsule and the test body. There are at least three ways to approach this problem. The first approach is to compute the force between each capsule mass element and a test body mass element, and to perform a double summation on these forces. If N is the number of capsule mass elements, and N_B is the number of test body mass elements, then the cardinality of the computation is $N \otimes N_B$. (The complexity of the computation is the product of the complexity of a single element computation by the cardinality). The second approach is a double integration over the bodies. The drawback of the first approach is the heavy computational effort, especially when we need an online computation in a dynamical process. The weakness of the second approach is in the

cumbersome analytical computation. Moreover, the integration will result in an asymptotic series of complicated functions. This will require intense computation. In addition, asymptotic series introduce a truncation error into the computation. We adopted a third approach for this model.

Our computational approach is to consider the capsule as a discrete ensemble of lumped mass, where the resultant force and torque acting on the test body are the cumulative force and torque due to each capsule mass element. In other words, the interaction is between a finite body and a point mass. This approach is a tradeoff between the previous approaches, its cardinality is N. The main advantage is due to the flexibility of modeling any capsule shape, according to future requirements.

The purpose of the following computation is to come up with simple closed-form analytical expressions, for the force and torque acting on the spinning test mass due to the capsule gravitational attraction.

Gravitational Model

The gravitational potential for finite size bodies, is:

$$V = -G \int_{\Re_o} \int_{\Re_B} \frac{dM_B}{r} dM_o$$

Where in our case, $\Re_B$ is the test mass (proof mass), and $\Re_0$ represents the attracting bodies, as the capsule (cylinder and caps) and the Earth.

For the purpose of simplicity we will proceed with a representation of the test body, and a single element of the attracting mass, M_i.

The gravitational potential at a representative element mass M_i due to the test body is: $V(M_i) = -GM_i \int_{M_B} \frac{dM_B}{r}$, where $\vec{r}$ is the radius vector between an element mass of the test body and dM_oas shown in Figure 53.

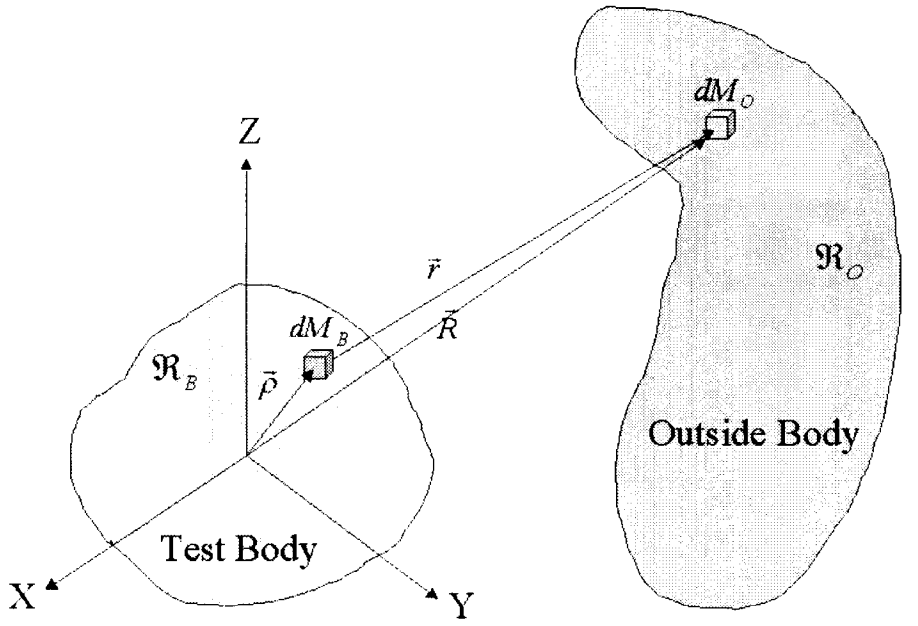

Figure 42 Gravitation model for test mass and outer attracting bodies

Assuming a sufficient discretization, the total force acting on the test body due to all outer mass elements is: $\vec{F}_B \cong \sum_{i=1}^{N} \nabla V(M_i)$, where N is the number of outer mass elements.

The model utilizes two coordinate systems. The first is the capsule frame, denoted by: $\{X,Y,Z\}$. X,Y are so far arbitrary, while Z coincides with the symmetry axis of the main cylinder. The test body frame is denoted by $\{x,y,z\}$, is attached to the test mass. So far, the origin and the orientation of the coordinate system are arbitrary. The gravitational potential will be expressed in body frame. The inertia coefficients of the body are constants in this frame.

The analytical procedure is to express $\vec{r}$ as $\vec{r} = \vec{R} - \vec{\rho}$, and to expand the potential by the following power series: $\frac{1}{r} = \frac{1}{R} \sum_{n=0}^{\infty} \left(\frac{\rho}{R}\right)^n P_n\left(\frac{\vec{R}\cdot\vec{\rho}}{R\rho}\right)$.

Here P_n is the Legendre polynomial of degree n.

The derivation consists of the following steps. Substituting the inverse radius approximation into the potential, carrying out the integration, while expressing vectors in body frame, as follows. $\vec{R} = (l e_x + m e_y + n e_z) R$ and $\vec{\rho} = x e_x + y e_y + z e_z$, where $\{e_x, e_y, e_z\}$ are body unit directions, and $\{l, m, n\}$ are direction cosines between $\vec{R}$ and the body axes.

The resulting potential is a summation over all mass elements M_i:

$$
\begin{aligned}
V = \sum_{i=1}^{N} \{ & -\frac{GM_1M_2}{R} - \frac{GM_1M_2}{R^2}\left[l\bar{x} + m\bar{y} + n\bar{z}\right] \\
& - \frac{GM_1}{2R^3}[(3l^2 - 1)\,J_{xx} + (3m^2 - 1)\,J_{yy} + (3n^2 - 1)\,J_{zz} + 6(lm\,J_{xy} + l\,n\,J_{xz} + mn\,J_{yz})] \\
& - \frac{GM_1}{2R^4}[l(5l^2 - 3)\,J_{xxx} + m(5m^2 - 3)\,J_{yyy} + n(5n^2 - 3)\,J_{zzz} \\
& + 3m(5l^2 - 1)\,J_{xxy} + 3n(5l^2 - 1)\,J_{xxz} + 3l(5m^2 - 1)\,J_{xyy} \\
& + 3n(5m^2 - 1)\,J_{yyz} + 3l(5n^2 - 1)\,J_{xzz} + 3m(5n^2 - 1)J_{yzz} \\
& + 6lmn\,J_{xyz}] + O(\frac{1}{R^5})\}
\end{aligned}
$$

where $j_{x^p y^q z^r}$ are the inertia integrals defined as:

$$j_{x^p y^q z^r} = \int_{M_B} x^p y^q z^r \, dm$$

For the second order, it is common to work with the moment of inertia. The following relations relate it to the inertia integrals:

$$J_{xx} = \frac{1}{2}(\mathrm{I}_{yy} + \mathrm{I}_{zz} - \mathrm{I}_{xx})$$

$$J_{yy} = \frac{1}{2}(\mathrm{I}_{xx} + \mathrm{I}_{zz} - \mathrm{I}_{yy})$$

$$J_{xx} = \frac{1}{2}(\mathrm{I}_{xx} + \mathrm{I}_{yy} - \mathrm{I}_{zz})$$

$$J_{xy} = I_{xy}$$

$$J_{xz} = I_{xz}$$

$$J_{yz} = I_{yz}$$

We define $\vec{\delta} = \{\overline{\mathrm{x}}, \overline{\mathrm{y}}, \overline{\mathrm{z}}\}$ as the offset between the origin and the center of mass. It should be emphasized at this point that the origin does not necessarily coincide with the center of mass. Although the test bodies are typically axisymmetric, and ideally the geometrical center is the center of mass, a mass perturbation can divert the center of mass from the geometrical center.

Note that if the origin is at the center of mass, the body frame coincides with the principal axes, and $O(1/R^4)$ is neglected, then the resulting potential is the so-called MacCullagh formula:

$$V \cong -\frac{GM_1M_2}{R} - \frac{GM_1}{2R^3}\left(tr\,\mathrm{I} - 3\mathrm{I}_R\right), \quad \text{where} \quad \mathrm{I}_R = \hat{e}_R \cdot \vec{\mathrm{I}} \cdot \hat{e}_R = l^2\mathrm{I}_{xx} + m^2\mathrm{I}_{yy} + n^2\mathrm{I}_{zz}$$

is the projection of the second order inertia tensor $\vec{\mathrm{I}}$ on $\vec{R}$.

The force acting on the body is the gradient of the potential (the negative gradient is the force acting on M_i).

The resulting total force components, in body frame, are:

$$F_x = G\sum_{i=1}^{N} M_i\{\frac{M_B l}{R_i^2} + \frac{M_B}{R_i^3}\left[(3l_i^2-1)\bar{x} + 3l_i m_i \bar{y} + 3l_i n_i \bar{z}\right]$$

$$+ \frac{1}{R_i^4}[(\frac{5}{2}\Gamma_i - I_{yy} - I_{zz} + 2I_{xx})l_i + 3m_i(5l_i^2-1)I_{xy} + 3n_i(5l_i^2-1)I_{xz} + 15l_i m_i n_i I_{yz}]$$

$$+ \frac{1}{R_i^5}[\frac{1}{2}(35l_i^4 - 30l_i^2 + 3)J_{xxx} + \frac{5}{2}(7m_i^2-3)l_i m_i J_{yyy} + \frac{5}{2}(7n_i^2-3)l_i n_i J_{zzz}$$

$$+ \frac{15}{2}(7l_i^2-3)l_i m_i J_{xxy} + \frac{15}{2}(7l_i^2-3)l_i n_i J_{xxz} + \frac{3}{2}(35l_i^2 m_i^2 - 5l_i^2 - 5m_i^2 + 1)J_{xyy}$$

$$+ \frac{15}{2}(7m_i^2-1)l_i n_i J_{yyz} + \frac{3}{2}(35l_i^2 n_i^2 - 5l_i^2 - 5n_i^2 + 1)J_{xzz} + \frac{15}{2}(7n_i^2-1)l_i m_i J_{yzz}$$

$$+ 3(7l_i^2-1)m_i n_i J_{xyz}] + H.O.T\}$$

$$F_y = G\sum_{i=1}^{N} M_i\{\frac{M_B m_i}{R_i^2} + \frac{M_B}{R_i^3}\left[3l_i m_i \bar{x} + (3m_i^2-1)\bar{y} + 3m_i n_i \bar{z}\right]$$

$$+ \frac{1}{R_i^4}[(\frac{5}{2}\Gamma_i - I_{xx} - I_{zz} + 2I_{yy})m_i + 3l_i(5m_i^2-1)I_{xy} + 15l_i m_i n_i I_{xz} + 3n_i(5m_i^2-1)I_{yz}]$$

$$+ \frac{1}{R_i^5}[\frac{5}{2}(7l_i^2-3)l_i m_i J_{xxx} + \frac{1}{2}(35m_i^4 - 30m_i^2 + 3)J_{yyy} + \frac{5}{2}(7n_i^2-3)m_i n_i J_{zzz}$$

$$+ \frac{3}{2}(35l_i^2 m_i^2 - 5m_i^2 - 5l_i^2 + 1)J_{xxy} + \frac{15}{2}(7l_i^2-1)m_i n_i J_{xxz} + \frac{15}{2}(7m_i^2-3)l_i m_i J_{xyy}$$

$$+ \frac{15}{2}(7m_i^2-3)m_i n_i J_{yyz} + \frac{15}{2}(7n_i^2-1)l_i m_i J_{xzz} + \frac{3}{2}(35m_i^2 n_i^2 - 5m_i^2 - 5n_i^2 + 1)J_{yzz}$$

$$+ 3(7m_i^2-1)l_i n_i J_{xyz}] + H.O.T\}$$

$$F_z = G\sum_{i=1}^{N} M_i\{\frac{M_B l}{R_i^2} + \frac{M_B}{R_i^3}\left[3l_i n_i \bar{x} + 3m_i n_i \bar{y} + 3(n_i^2-1)\bar{z}\right]$$

$$+ \frac{1}{R_i^4}[(\frac{5}{2}\Gamma_i - I_{xx} - I_{yy} + 2I_{zz})n_i + 15l_i m_i n_i I_{xy} + 3l_i(5n_i^2-1)I_{xz} + 3m_i(5n_i^2-1)I_{yz}]$$

$$+ \frac{1}{R_i^5}[\frac{5}{2}(7l_i^2-3)l_i n_i J_{xxx} + \frac{5}{2}(7m_i^2-3)m_i n_i J_{yyy} + \frac{1}{2}(35n_i^4 - 30n_i^2 + 3)J_{zzz}$$

$$+ \frac{15}{2}(7l_i^2-1)m_i n_i J_{xxy} + \frac{3}{2}(35l_i^2 n_i^2 - 5l_i^2 - 5n_i^2 + 1)J_{xxz} + \frac{15}{2}(7m_i^2-1)l_i n_i J_{xyy}$$

$$+ \frac{3}{2}(35m_i^2 n_i^2 - 5m_i^2 - 5n_i^2 + 1)J_{yyz} + \frac{15}{2}(7n_i^2-1)l_i n_i J_{xzz} + \frac{15}{2}(7n_i^2-3)m_i n_i J_{yzz}$$

$$+ 3(7n_i^2-1)l_i m_i J_{xyz}] + H.O.T\}$$

where

$$\Gamma_i = (I_{yy} + I_{zz} - 2I_{xx}) l_i^2 + (I_{xx} + I_{zz} - 2I_{yy}) m_i^2 + (I_{xx} + I_{yy} - 2I_{zz}) n_i^2$$

Note that the force has the following order of magnitude:

$$F \propto \sum_i G \frac{M_i M_B}{R_i^2} \{O(1) + O(\frac{\overline{\rho}}{R_i}) + O(\frac{L_B^2}{R_i^2}) + O(\frac{L_B^3}{R_i^3}) + H.O.T\}$$

Where L_B is a typical length of the test body, $\frac{L_B}{R_i} << 1$, and $\frac{\overline{\rho}}{R_i} << 1$.

The torque, acting on the test body, can be computed with respect to the center of mass or with respect to the geometrical center. Both coincide when the body has perfect symmetries. In reality there are mass imperfections that cause the center of mass to deviate from the geometrical center.

Since we have no a-priori knowledge of the imperfections, our reference point for computing the torque is the geometrical center. The effect of the imperfection in demonstrated for a simple case. Let $\vec{\delta}$ be the radius vector between the reference point to C.M. The bias is due to a disturbing mass m_P at a radius vector $\vec{\delta}_P$ relative to the reference point. Therefore, the value of $\vec{\delta}$ is:

$$\vec{\delta} = \frac{m_P}{M_B} \vec{\rho}_P$$

Thus, the effect of imperfections is proportional to its disturbing mass and to its deviation from the center of mass.

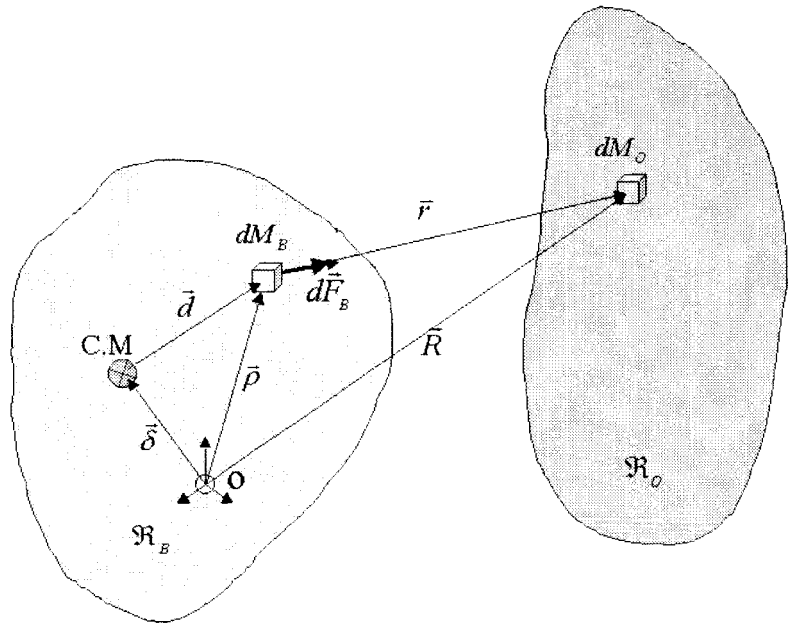

Figure 43 A Model for the Torque

There are few approaches for computing the torque. Our approach is to integrate the torque due to mass element in each body. The torque with respect to an arbitrary point is, therefore:

$$\vec{T}_o = \vec{T}_{C.M} + \vec{\delta} \times \vec{F}_B$$

where,

$$\vec{T}_{C.M} = G \int_{\Re_O} \int_{\Re_B} \vec{d} \times \frac{\vec{r}}{r^3} dM_B \, dM_O \cong G \sum_{i=1}^{N} m_i \int_{\Re_B} \frac{\vec{d} \times \vec{R}}{r^3} dM_B$$

$$\vec{F}_B = G \int_{\Re_O} \int_{\Re_B} \frac{\vec{r}}{r^3} dM_B \, dM_O = G \sum_{i=1}^{N} m_i \int_{\Re_B} \frac{\vec{r}}{r^3} dM_B$$

There are three approaches to compute the integrals. The choice of the approach depends on the size of each body. If both $\Re_B$ and $\Re_O$ are small compared with R, than we can expand r, and obtain an analytical approximation. If only $\Re_B$ is small, as in our

case, we can approximate $\Re_B$ but have to integrate numerically in $\Re_O$. If both are large relative to r, then the only way is to perform a double numerical integration. In our case, not only $\Re_O$ is large, it is also surrounded by $\Re_B$, so there is no topologically way to expand r in $\Re_O$.

$$
\begin{aligned}
T_x &= 3G\sum_{i=1}^{N} M_i\{\frac{1}{R_i^3}[m_i n_i (I_{zz} - I_{yy}) + l_i n_i I_{xy} - l_i m_i I_{xz} + (n_i^2 - m_i^2) I_{yz}] \\
&+ \frac{1}{2R_i^4}[n_i (5m_i^2 - 1)J_{yyy} - m_i (5n_i^2 - 1)J_{zzz} + n_i (5l_i^2 - 1)J_{xxy} + 10 l_i m_i n_i J_{xyy} \\
&- m_i (5l_i^2 - 1)J_{xxz} - 10 l_i m_i n_i J_{xzz} + m_i (10n_i^2 - 5m_i^2 + 1)J_{yyz} \\
&- n_i (10m_i^2 - 5n_i^2 + 1)J_{yzz} + 10 l_i (n_i^2 - m_i^2)J_{xyz}] + \text{H.O.T}\} \\
T_y &= 3G\sum_{i=1}^{N} M_i\{\frac{1}{R_i^3}[l_i n_i (I_{xx} - I_{zz}) - m_i n_i I_{xy} + l_i m_i I_{yz} + (l_i^2 - m_i^2) I_{xz}] \\
&+ \frac{1}{2R_i^4}[-n_i (5l_i^2 - 1)J_{xxx} + l_i (5n_i^2 - 1)J_{zzz} - 10 l_i m_i n_i J_{xxy} - n_i (5m_i^2 - 1)J_{xyy} \\
&- l_i (10n_i^2 - 5l_i^2 + 1)J_{xxz} + n_i (10l_i^2 - 5n_i^2 + 1)J_{xzz} + l_i (5m_i^2 - 1)J_{yyz} + 10 l_i m_i n_i J_{yzz} \\
&+ 10 m_i (l_i^2 - n_i^2)J_{xyz}] + \text{H.O.T}\} \\
T_z &= 3G\sum_{i=1}^{N} M_i\{\frac{1}{R_i^3}[l_i m_i (I_{yy} - I_{xx}) - (m_i^2 - l_i^2) I_{xy} + m_i n_i I_{xz} - l_i n_i I_{yz}] \\
&+ \frac{1}{2R_i^4}[m_i (5l_i^2 - 1)J_{xxx} - l_i (5m_i^2 - 1)J_{yyy} + l_i (10m_i^2 - 5l_i^2 + 1)J_{xxy} \\
&- m_i (10l_i^2 - 5m_i^2 + 1)J_{xyy} + 10 l_i m_i n_i J_{xxz} + m_i (5n_i^2 - 1)J_{xzz} - 10 l_i m_i n_i J_{yyz} \\
&- l_i (5n_i^2 - 1)J_{yzz} + 10 n_i (m_i^2 - l_i^2)J_{xyz}] + \text{H.O.T}\}
\end{aligned}
$$

The order of magnitude of the torque is:

$$T \propto \sum_i G \frac{M_i M_B}{R_i} \{ O(\frac{L_B^{\,2}}{R_i^{\,2}}) + O(\frac{L_B^{\,3}}{R_i^{\,3}}) + H.O.T \}$$

If the origin is at the center of mass and the body frame coincides with the principal axes, then the resulting torque is reduced the well-known expression (based on MacCullagh formula):

$$T_x \cong 3G\,(\mathrm{I_{zz}} - \mathrm{I_{yy}}) \sum_{i=1}^{N} \frac{M_i}{R_i^{\,3}} m_i\, n_i$$

$$T_y \cong 3G\,(\mathrm{I_{xx}} - \mathrm{I_{zz}}) \sum_{i=1}^{N} \frac{M_i}{R_i^{\,3}} l_i\, n_i$$

$$T_z \cong 3G\,(\mathrm{I_{yy}} - \mathrm{I_{xx}}) \sum_{i=1}^{N} \frac{M_i}{R_i^{\,3}} l_i\, m_i$$

We would like to propose a more general approach for a closed-form solution of the force/torque in terms of their frequencies.

Let us expand the force in potential orders as well as a Fourier series in the spin angle, assuming a pure spin around the axial axis of the test body.

$$\vec{F} = G \int_{\Re_o} \frac{1}{R^{d+2}} \sum_{d=0}^{d_{\max}} \{ \vec{a}_0^{(d)} + \sum_{n=1}^{d+1} [\vec{a}_n^{(d)} \cos n\varphi + \vec{b}_n^{(d)} \sin n\varphi] \} dM_0$$

where d is the degree of the inertia. Let $J_{x^i y^j z^k} = \int x^i y^j z^k dM_B$ than $d = i + j + k$. Assuming that we have carried out the integration (analytically or by numerical means), $\vec{F}$ can be expressed as:

$$\vec{F} = G \sum_{d=0}^{d_{\max}} \{ \vec{A}_0^{(d)} + \sum_{n=1}^{d+1} [\vec{A}_n^{(d)} \cos n\varphi + \vec{B}_n^{(d)} \sin n\varphi] \}$$

where $\vec{A}_n^{(d)} = \int_{\Re_0} \frac{\vec{a}_n^{(d)}}{R^{d+2}} dM_o$, and $\vec{B}_n^{(d)} = \int_{\Re_0} \frac{\vec{b}_n^{(d)}}{R^{d+2}} dM_o$.

These coefficients may be viewed as a generalization of the inertia coefficients of $\Re_O$. If $\Re_O$ is topologically connected (i.e., $\Re_B$ is outside $\Re_O$), and if $\Re_O$ is sufficiently small, then one may asymptotically expand these integrals. This will result in the inertia coefficients of $\Re_O$. In our case, these coefficients can be computed numerically, or sometimes analytically, when $\Re_O$ is simple enough.

For a more general rotation, one needs to express the direction cosines in terms of the general transformation matrix (rather than the single-axis rotation).

Order of Magnitude and Similarity Analysis

The dominant sources of the gravitational attraction are the capsule, the Earth, and to a lesser degree the Moon. Let us perform a qualitative comparison of each source. First, we should note that the force acting on the test mass is not a homogeneous function of the mass and the radius (as a force acting on a point mass). This is because the parameters R and M_B contribute as: $F \propto O\left(\frac{M_B}{R^2}\right) + O\left(\frac{M_B}{R^3}\right) + O\left(\frac{M_B}{R^4}\right) + O\left(\frac{M_B}{R^5}\right)$, or

$F \propto F^{(0)} + F^{(1)} + F^{(2)} + F^{(3)}$, where $F^{(0)}$ represents the 2-Body term, and so on (the order enumeration is according with the corresponding Inertia order). Therefore, it is impossible to express the ratio of forces from different sources as $F(M1,R1)/F(M2,R2) \propto f((M1/M1)^m, (R1/R1)^n)$.

On the other hand, each order is homogeneous, that is

$$F^{(k)}(M1,R1)/F^{(k)}(M2,R2) = (M1/M2)(R2/R1)^{(k)}$$

Therefore, in order to compare different sources of attraction, we must consider each order separately.

The following qualitative discussion concerns the force difference between the two test bodies. Let us denotes $f()$ as a generic function, then a generic expression for the force acting on test mass B_j is:

$$F^{B_j} = f(M_j;)O\left(\frac{1}{R^2}\right) + f(\bar{\rho}_j;)O\left(\frac{1}{R^3}\right) + f(I_{2j};)O\left(\frac{1}{R^4}\right) + f(I_{3j};)O\left(\frac{1}{R^5}\right)$$

We present two models for the force difference. In the first model the two test bodies are centered, and the inertia components of the bodies are different. In the second model, the bodies are of equal inertia, but are not centered. These two models are idealization of the two sources of difference, while the reality is probably a combination of these.

The force difference for the first model is:

$$\Delta F = F^{B_2} - F^{B_1} = f(\Delta M;)O\left(\frac{1}{R^2}\right) + f(\Delta\bar{\rho};)O\left(\frac{1}{R^3}\right) + f(\Delta I_2;)O\left(\frac{1}{R^4}\right) + f(\Delta I_3;)O\left(\frac{1}{R^5}\right)$$

The force difference for the second model is represented by a differential. For central deviation ε, the force differential is:

$$dF \cong F^{B_2} - F^{B_1} \cong \nabla F \cdot \varepsilon = f(M;)O\left(\frac{1}{R^3}\right) + f(\bar{\rho};)O\left(\frac{1}{R^4}\right) + f(I_2;)O\left(\frac{1}{R^5}\right) + f(I_3;)O\left(\frac{1}{R^6}\right)$$

The ratio between force terms of order k from two different sources 1 and 2, is:

$$\frac{F^{(k)}(M_1,R_1)}{F^{(k)}(M_2,R_2)} = \frac{M_1}{M_2}\left(\frac{R_2}{R_1}\right)^k$$

The following table compares the force order of magnitude due to different sources. Note that we eliminated order 0 (2-Body), since the test body is in free fall.

Table 1 Ratio of force terms for few orders for the dominant gravitational sources

Inertia order	Capsule / Earth	Capsule / Moon	Earth / Moon
1	$4*10^{-3}$	$8*10^{4}$	$2*10^{7}$
2	$3*10^{4}$	$3*10^{13}$	$1*10^{9}$
3	$2*10^{11}$	$1*10^{22}$	$6*10^{10}$
4	$1*10^{18}$	$4*10^{30}$	$4*10^{12}$

It is obvious that the effect of the Moon is negligible. The Earth is dominant only with respect to the gravity gradient. Again, as the order under consideration becomes higher, the effect of the capsule increases.

To gain more insight into the nature of gravitational attraction let us examine the force. It can be rewritten in the following form:

$$F = O\left(\frac{1}{R^2}\right)O(c) + O\left(\frac{1}{R^3}\right)O(c^E) + O\left(\frac{1}{R^4}\right)O(c^O) + O\left(\frac{1}{R^5}\right)O(c^E)$$

Where c represents the direction cosines. The notations c^O and c^E show the nature of the degree of the direction cosines (odd or even). For example, a square of a particular direction cosine has an even degree, while a product of the three direction cosines has an odd degree. Now, suppose that the test mass is at the center of the cylinder. Since for each direction cosine to a mass element there is an opposite direction cosine, all the odd terms are cancelled out. Therefore, the only non-zero contribution is due to the even terms.

Another important engineering issue is the role of the test body mass and size. For this purpose we perform a similarity analysis, as shown in the following.

We formulated the gravitational potential as an asymptotic series in $1/R^n$. Each term in the series has an inertial tensor of degree $n - 1$. For example, the first term is of order n = 1 and its inertia tensor is of order 0 (the test body mass). The third term is of degree n = 3 and its inertia tensor is of order 2. This non-uniformity introduces a problem, as mentioned earlier, when one computes the forces for a particular test mass, and wants to deduct the forces for a different scale of test mass. Mathematically speaking, if $F(M_{B1})$ and $F(M_{B2})$ are the forces due to two different test masses, then the ratio between the forces is not a homogeneous function, that is, $F(M_{B1})/F(M_{B2}) \neq g((M_{B1}/M_{B2})^m)$ where g is a function and m is the degree of the homogeneity. Note however that each term of the series is homogeneous by itself. For example, the first term is homogeneous of degree one, that is, the ratio between forces equals the ratio between the masses.

We will distinguish between two cases. In both, the mass distribution of the different test masses can be scaled. The first case is when the difference in masses is due to a different density. Since the forces are homogeneous of degree one in density, the ratio between the forces is equal to the ratio between the masses. In the second case the density is the same, and the different mass is due to different sizes. In this case we will apply a different similarity to each term. Let L and M be scaling factors for the length and the mass, respectively. If the density of different test bodies is the same, then $L \propto M^{1/3}$. Let $m = n - 1$ be the order of the moment of inertia. Its similarity dimension is $L^m M$, or $M^{1+m/3}$, or L^{m+3}. The acceleration similarity is $M^{m/3}$ or L^m. The following table summarizes the similarity dimension for each term in the potential.

Table 2 Similarity relations for the gravitational potential terms

Potential Order $n: 1/R^n$	Inertia Order $m = 1 - n$	Inertia Similarity	Acceleration Similarity
1	0	$M \quad (L^3)$	$1 \quad (1)$
2	1	$M^{4/3} \ (L^4)$	$M^{1/3} \ (L)$
3	2	$M^{5/3} \ (L^5)$	$M^{2/3} \ (L^2)$
4	3	$M^2 \ (L^6)$	$M \ (L^3)$
5	4	$M^{7/3} \ (L^7)$	$M^{4/3} \ (L^4)$

To summarize, given the force (or the acceleration) due to a particular test body, we can deduct the force (acceleration) due to another geometrically scaled test mass. The acceleration ratio (of two different test masses) versus similarity dimensions (mass and length) is illustrated in the following plot.

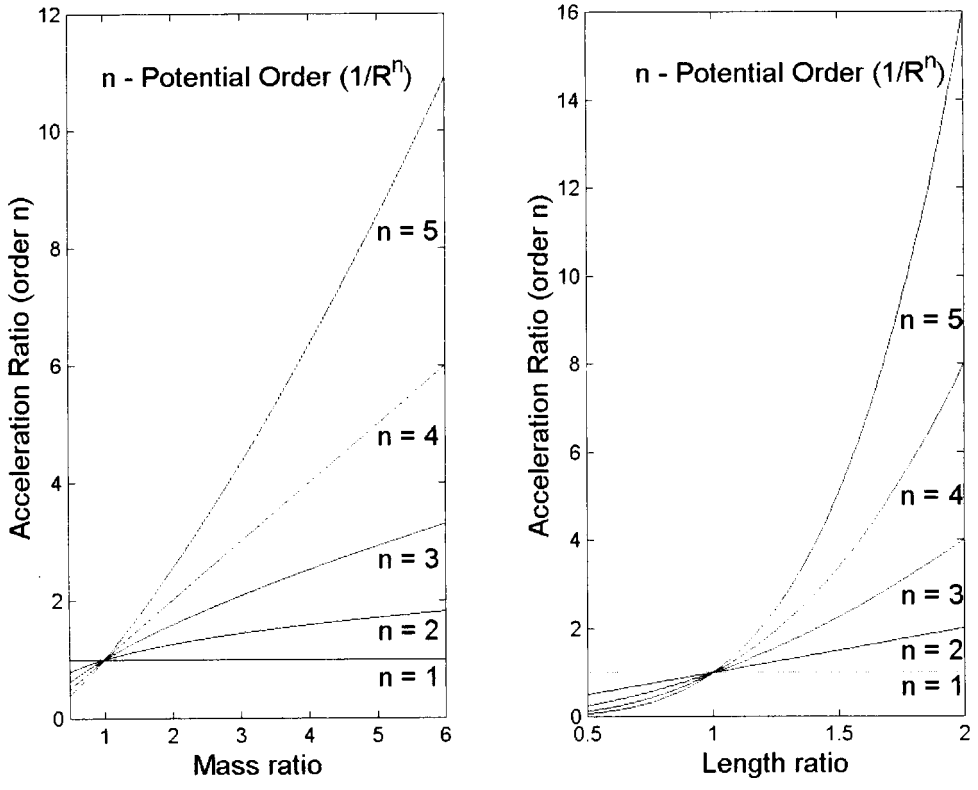

Figure 44 Scaling of Acceleration of Test Mass

The maximum potential order considered in this analysis is the hexadecapole (n = 5) which involves the fourth-order inertia integrals. We computed numerically the forces associated with the hexadecapole for a body with equal second-order inertia integrals (in order to minimize the quadrupole term). The results show that, at the worst expected location inside the capsule, the maximum acceleration associated with the hexadecapole term for a 1-kg proof mass are less than 10^{-16} g. In other words, for the accuracy goal of this experiment there is no need for belted cylinders (which reduce the hexadecapole component even further). Proof masses with equal second-order inertia integrals (or alternatively moments of inertia) and construction accuracy of order a few microns are sufficient to make the contributions of all the higher-order gravity terms negligible.

EFFECT OF INERTIA IMPERFECTION ON THE SPINNING TEST BODY

Our goal is to minimize the gravitational forces acting on the test mass. Observing the force equations reveals that the dominant term under our control is the term corresponding to the second order inertia. The offset effect may be bigger to start with but it can be reduced by centering. The direct way to minimize the forces is to require equal second moments of inertia. The left over forces is due to the imperfection, and to higher order inertia integrals. The purpose of the following discussion is to explore the effect of each term for a spinning test body.

First we will evaluate the mixed-inertial terms due to the imperfection.

We assume that the imperfection is due to disturbance in mass and in length. The nominal test body is a perfect cylinder, with radius R_B and length L_B. In order to minimize the force we require that $I_{XX} = I_{YY} = I_{ZZ}$. This constraint results in a given aspect ratio of the cylinder as follows: $L_B = \sqrt{3}\,R_B$. Given the mass density, the mass or the sizes of the cylinder are now functions of a single free parameter. For example, given the mass, M_B, and the density, ρ_B, the length is: $L_B = \left(\frac{3M_B}{\pi\rho_B}\right)^{\frac{1}{3}}$

The similarity dimension of the k-order inertia is: $[I] = ML^k$. Thus, the perturbed k-ordered inertia is: $[\delta I] = L^k\,\delta M + kML^{k-1}\delta L$, or

$$\left[\frac{\delta I}{I}\right] = \left[\frac{\delta M}{M}\right] + k\left[\frac{\delta L}{L}\right]$$

Next we consider the effect of the spin. The test body is spinning about its x-axis with a frequency that will be regarded as a fundamental frequency, or P1 (period one). We are primarily concerned with P1 which is the period of the measured signal. For that purpose we will analyze Fy by substituting the direction cosines, shown below, into the force expression.

$$l_i = l_i(t; P1); \quad m_i = m_i(t; P1); \quad n_i = n_i(t; P1)$$

It is important to note that the forces are expressed in body frame. The direction cosines are P1-periodic. Moreover, if the body fall such that the body x-axis is parallel to the capsule X-axis, only m and n are periodic, as will be seen from the following discussion.

The periodicity in time is introduced through the direction cosines that represent the orientation of the body frame relative to the capsule frame. The transformation between the two is:

$$\begin{bmatrix} x \\ y \\ z \end{bmatrix} = \begin{bmatrix} 1 & 0 & 0 \\ 0 & c\theta & s\theta \\ 0 & -s\theta & c\theta \end{bmatrix} \begin{bmatrix} X \\ Y \\ Z \end{bmatrix}$$

The resulting direction cosines are:

$$l = \frac{x}{R} = \frac{X}{R} \neq l(\theta)$$

$$m = \frac{y}{R} = \frac{Y c\theta + Z s\theta}{R}$$

$$n = \frac{z}{R} = \frac{-Y s\theta + Z c\theta}{R}$$

l is a cyclic function only if the body deviates from the X-axis. If the test body is perfect, then only the point mass term and the first term of $O(1/R^4)$ contribute to Fy. Otherwise, m, n introduce higher harmonics. If the power of the direction cosines is even (N_E), than the additional harmonics are: $P_0, P_2, \cdots, P_{N_E}$. For odd power ($N_O$) the additional harmonics are: $P_1, P_3, \cdots, P_{N_O}$. The dominant time dependency of a perfect body is introduced through the first order attraction on a point mass. It results in a fundamental frequency, because the gravitational attraction is static in capsule frame, while the measurement is in the rotating body frame.

The expected frequencies are the following. P1 from the point mass term $O(1/R^2)$. P1 and P2 from the offset term $O(1/R^3)$. Since Γ_i contributes P2, the term of $O(1/R^4)$ contributes P1 and P2. However, because of the almost axial-symmetricity of the test body, Γ_i is almost a constant, so the dominant frequency of $O(1/R^4)$ should be P1. The term of $O(1/R^5)$ contributes P1, P2, P3 and P4, where P2 should be dominant.

The analysis above is depends whether the x-axis is parallel to the X-axis. If it is, then l = constant. Otherwise $l = l(\theta)$ and higher frequencies would be involved. In this

case, higher frequencies would be invoked. The explicit orientation dependency of period one becomes:

$$F_y^{Body}(\theta;P_1) = G\sum_{i=1}^{N} M_i \left\{ \frac{1}{R_i^2}\tilde{F}_y^{(2)} + \frac{1}{R_i^3}\tilde{F}_y^{(3)} + \frac{1}{R_i^4}\tilde{F}_y^{(4)} + \frac{1}{R_i^5}\tilde{F}_y^{(5)} \right\}$$

where

$$\tilde{F}_y^{(2)} = M_B(\hat{Y}_i\cos\theta + \hat{Z}_i\sin\theta)$$

$$\tilde{F}_y^{(3)} = 3M_B\hat{X}_i(\hat{Y}_i\cos\theta + \hat{Z}_i\sin\theta)\bar{x}$$

$$\tilde{F}_y^{(4)} = \left\{\frac{5}{2}[A\hat{X}_i^2\hat{Y}_i + \frac{1}{4}(3B+C)(\hat{Y}_i^3 + \hat{Y}_i\hat{Z}_i^2)] - B\hat{Y}_i\right\}\cos\theta + \left\{\frac{5}{2}[A\hat{X}_i^2\hat{Z}_i + \frac{1}{4}(3B+C)(\hat{Y}_i^2\hat{Z}_i + \hat{Z}_i^3)] - B\hat{Z}_i\right\}\sin\theta$$

$$\tilde{F}_y^{(5)} = \frac{5}{2}(7\hat{X}_i^2 - 3)(\hat{Y}_i\cos\theta + \hat{Z}_i\sin\theta)\hat{X}_i I_{XXX}$$

and $\hat{X}_i = X/R$, $\hat{Y}_i = Y/R$, $\hat{Z}_i = Z/R$ are the direction cosines in the capsule frame.

An interesting case is the effect of the attraction of a point mass located on the Z-axis. It may represent the Earth attraction on horizontally falling body, or the caps on the top or the button of the capsule.

Let the attracting mass M_1 be at $Z1 = \mp R_1$ in the plan $X = Y = 0$. Using the relations: $Z_1 = R_1\,\mathrm{sgn}(Z_1)$, $\hat{Z}_1 = \mathrm{sgn}(Z_1)$, $\hat{Z}^2 = 1$, and substituting the attracting mass coordinates results in the following simple equation:

$$F_y^{Body}(\theta;P_1, I=0) = GM_i\left\{\frac{M_B}{R_i^2} + \frac{1}{8}\frac{1}{R_i^4}(7B+5C)\right\}\mathrm{sgn}(Z_1)\sin\theta$$

Again, the relations above are the terms corresponding to P1. The other frequencies may be observed from analytical expansions, or from a numerical frequency analysis, as demonstrated in the next section.

Numerical Investigation of an Imperfect Spinning Test Body

The scenario under investigation is shown in Figure 56. The capsule consists of a hollow cylinder, covered by two flat caps and a total mass of 500 kg. The test body mass is 1 kg with sizes: $R_B = 0.0412m$ and $L_B = 0.0713m$. The geometrical and mass inhomogeneity errors are: $\delta L/L = 10^{-4}$ and $\delta M/M = 10^{-5}$. Consequently, the offset components are: $\bar{x} = 1.7 \times 10^{-6} m$, $\bar{y} = 2 \times 10^{-6} m$, $\bar{z} = 1.7 \times 10^{-6} m$. The components of the inertial matrix are: $I_{XX} = 8.5 \times 10^{-4}$, $I_{YY} = 8.501 \times 10^{-4}$, $I_{ZZ} = 8.5015 \times 10^{-4}$. Note that the nominal values of those are the same. The perturbations prevent the elimination of the following inequalities: $I_{XX} + I_{YY} - 2I_{ZZ} \neq 0$, $I_{XX} + I_{ZZ} - 2I_{YY} \neq 0$, $I_{YY} + I_{ZZ} - 2I_{XX} \neq 0$.

$I_{XY} = 3 \times 10^{-8}$, $I_{XZ} = 3 \times 10^{-8}$, $I_{YZ} = 4 \times 10^{-8}$. The components of the third-order inertia tensor are: $I_{XXX} = 5 \times 10^{-10}$, $I_{YYY} = 8 \times 10^{-10}$, $I_{ZZZ} = 8 \times 10^{-10}$, $I_{XXY} = 6 \times 10^{-10}$, $I_{XXZ} = 6 \times 10^{-10}$, $I_{XYY} = 7 \times 10^{-10}$, $I_{YYZ} = 8 \times 10^{-10}$, $I_{XZZ} = 6 \times 10^{-10}$, $I_{YZZ} = 8 \times 10^{-10}$, $I_{XYZ} = 7 \times 10^{-10}$.

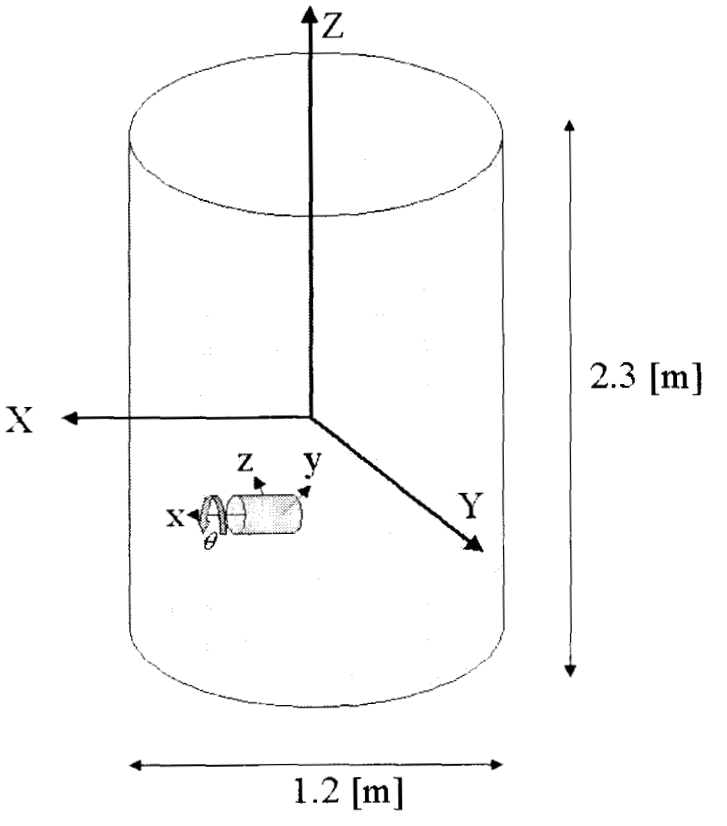

Figure 45 Coordinate systems for the test body and the capsule

The gravitational force and the torque acting on the test mass were computed at 9 points inside the capsule. Three points along the axial axis, three points along an axis deviated by 0.1 m from the axial axis, and three points along an axis deviated by 0.2 m from the axial axis. The ninth point is the farthest away, thus representing the worst case.

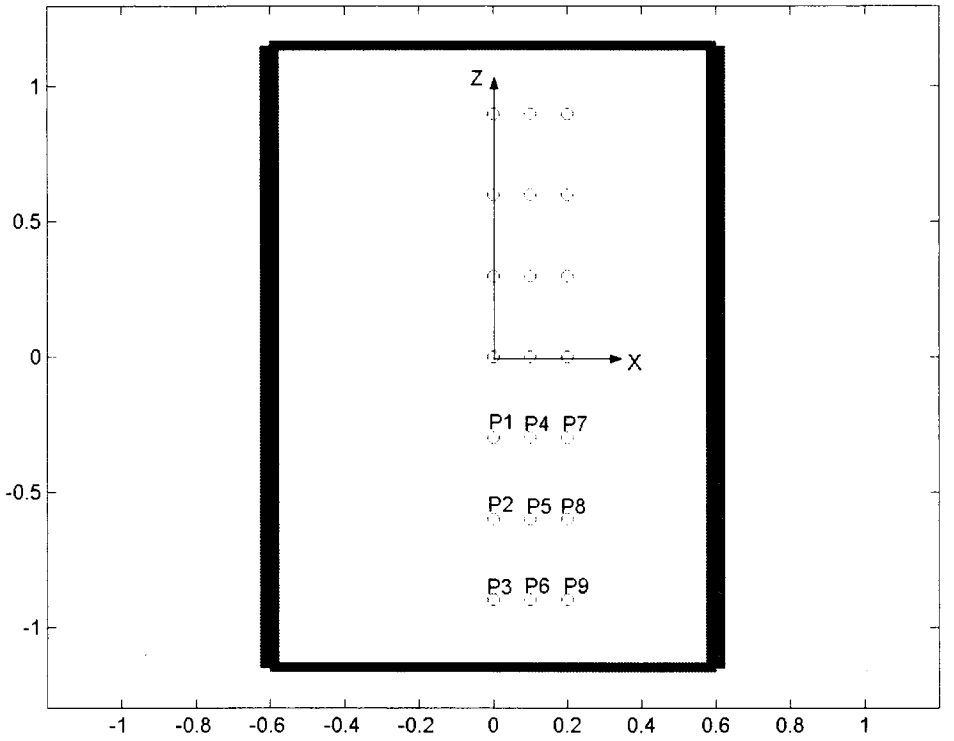

Figure 46 Tested Points inside the Capsule

We are mostly interested in F_Y (F_Y is in phase with F_Z) and in T_X. Because of the free fall, we exclude the 2-Body terms. The following plots show the angular history of the force/torque for a single revolution with respect to the x-axis, and the corresponding Fast Fourier Transform. The latter is normalized, such that the highest amplitude is one. The results are given in the following 18 plots. The analysis of the frequency spectrum requires a closed look at the equations for the force and torque, considering the particular location of the test mass relative to the capsule. Some of the results are non intuitive. The general approach to estimate the results is to specify each term according to the degree of the direction cosines (odd or even), and consider possible cancellations due to anti-symmetricity with respect to the radius vector between the test mass and each capsule element. The results are shown in the following figures.

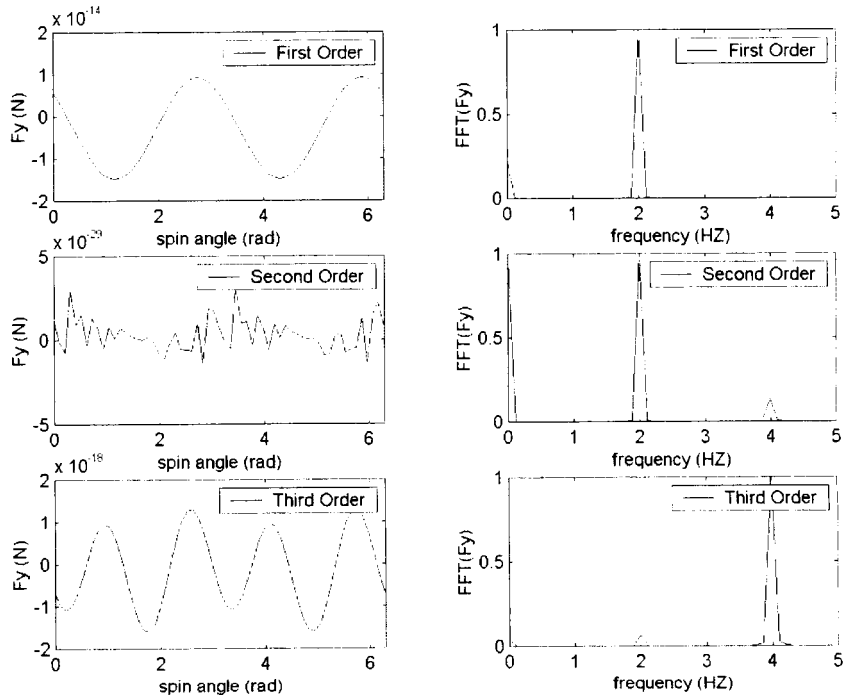

Figure 47 Ordered Force and harmonics at Point 1 due to Capsule Attraction

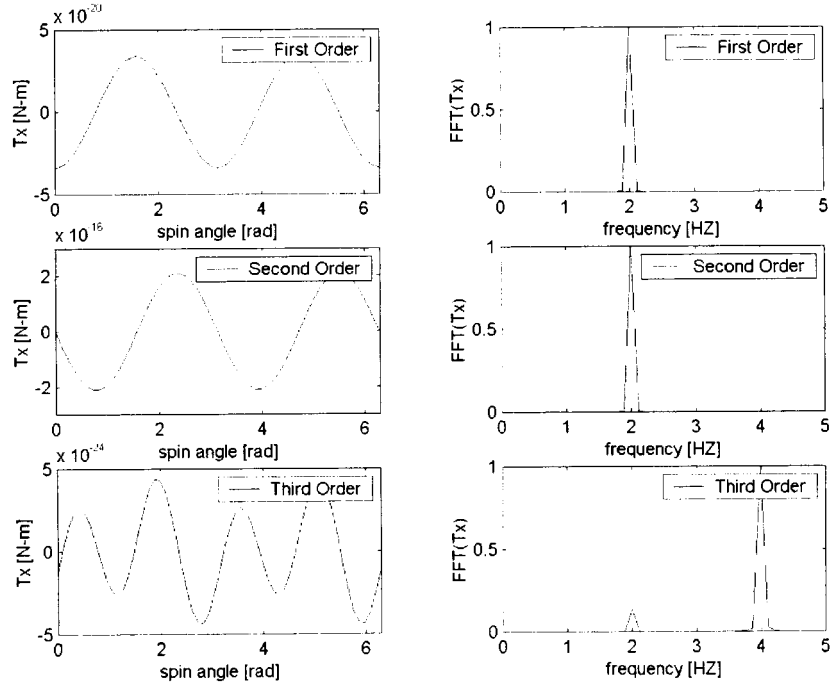

Figure 48 Ordered Torque and harmonics at Point 1 due to Capsule Attraction

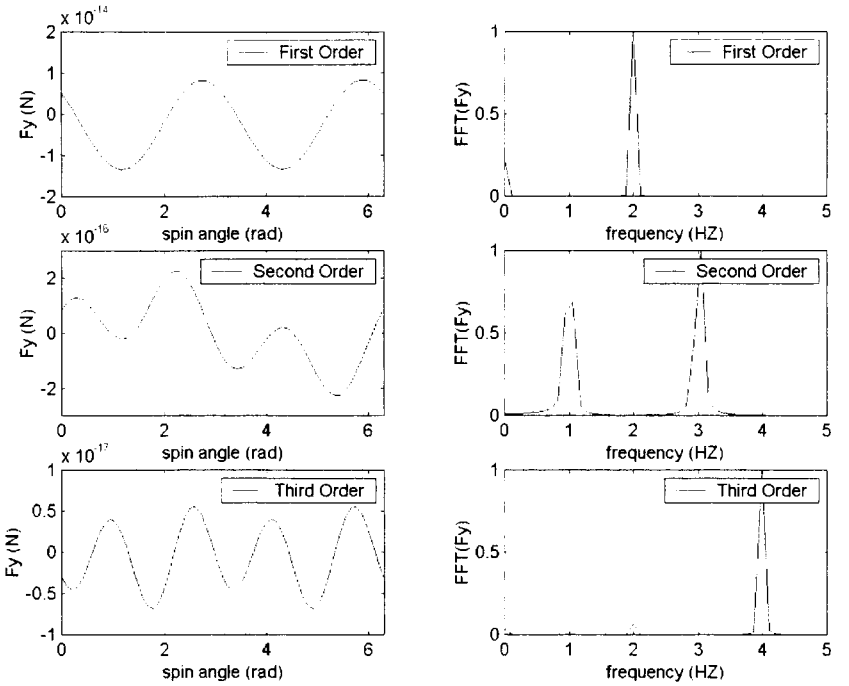

Figure 49 Ordered Force and harmonics at Point 2 due to Capsule Attraction

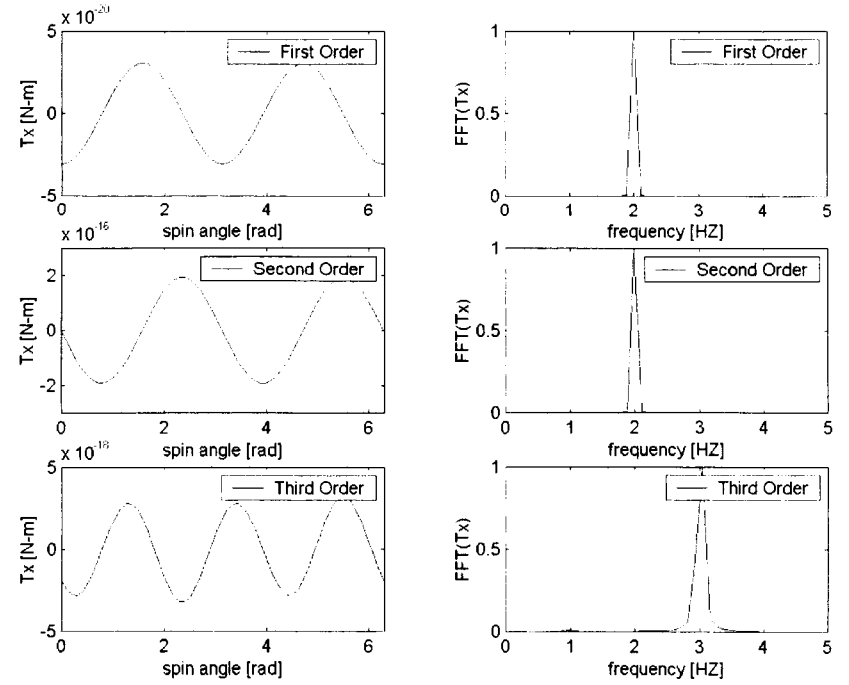

Figure 50 Ordered Torque and harmonics at Point 2 due to Capsule Attraction

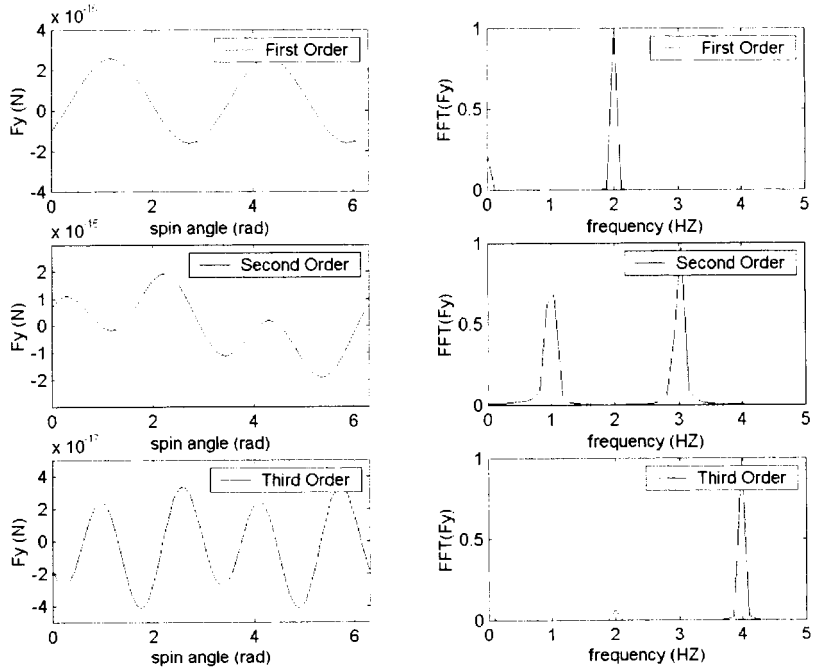

Figure 51 Ordered Force and harmonics at Point 3 due to Capsule Attraction

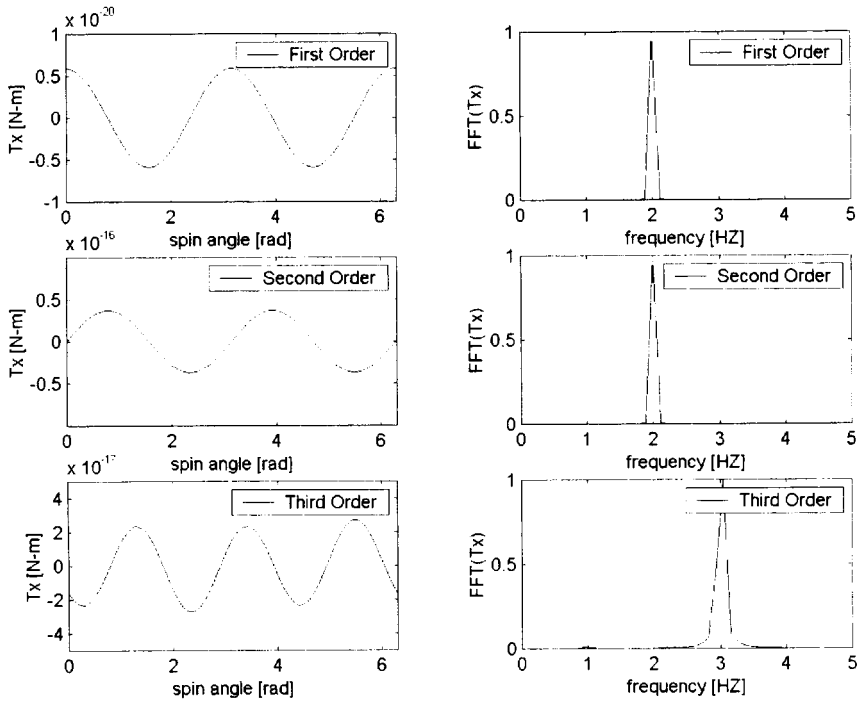

Figure 52 Ordered Torque and harmonics at Point 3 due to Capsule Attraction

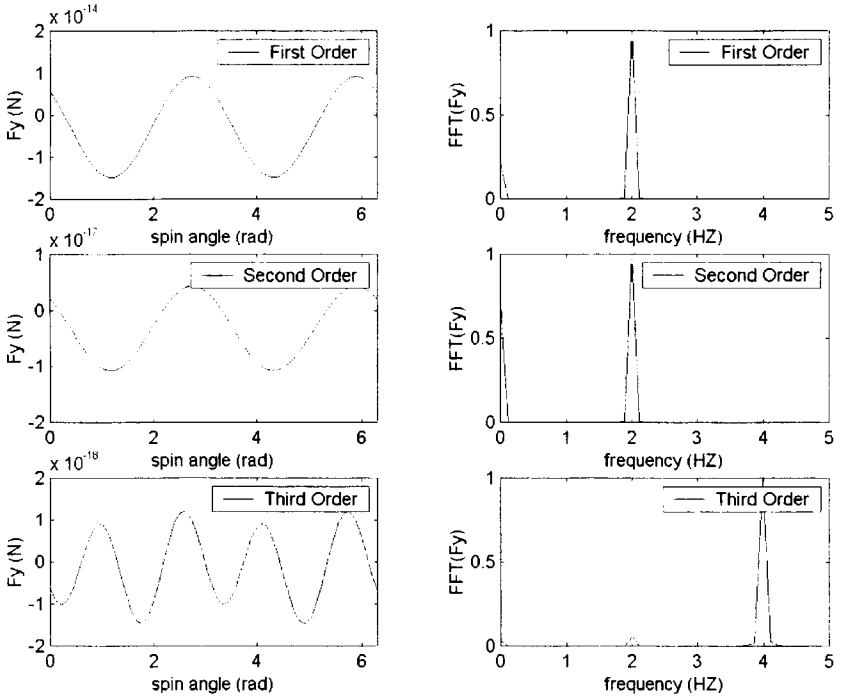

Figure 53 Ordered Force and harmonics at Point 4 due to Capsule Attraction

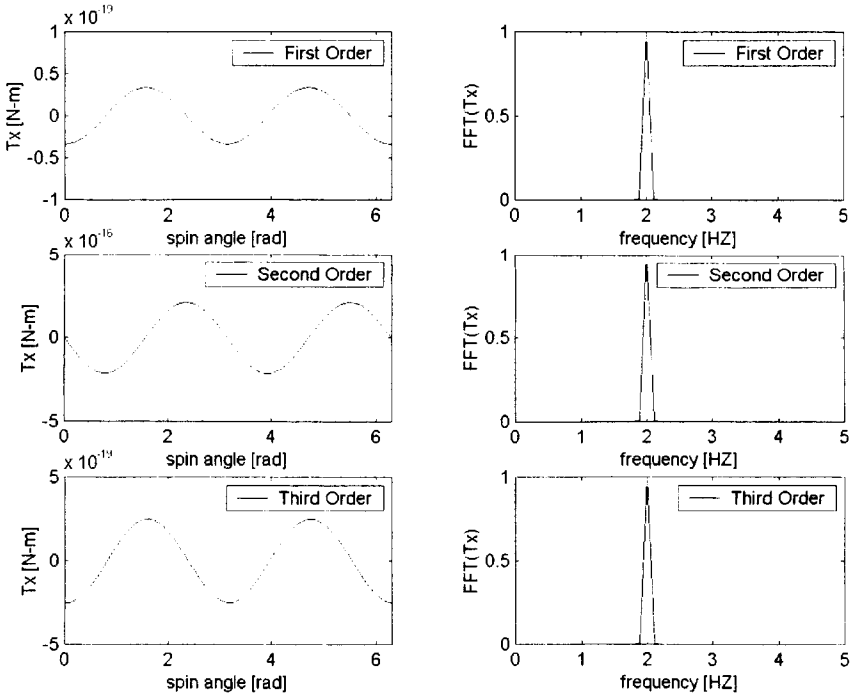

Figure 54 Ordered Torque and harmonics at Point 4 due to Capsule Attraction

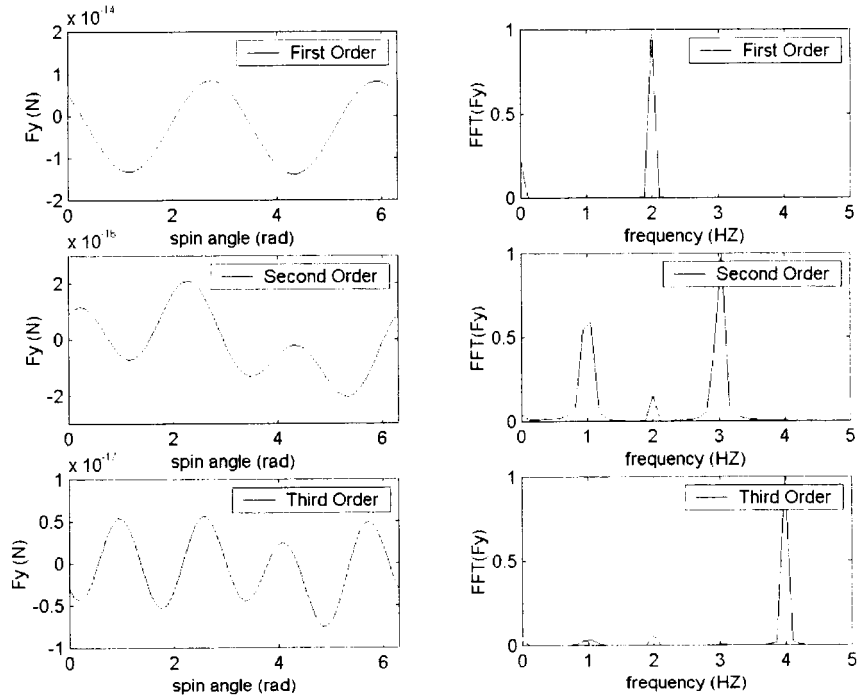

Figure 55 Ordered Force and harmonics at Point 5 due to Capsule Attraction

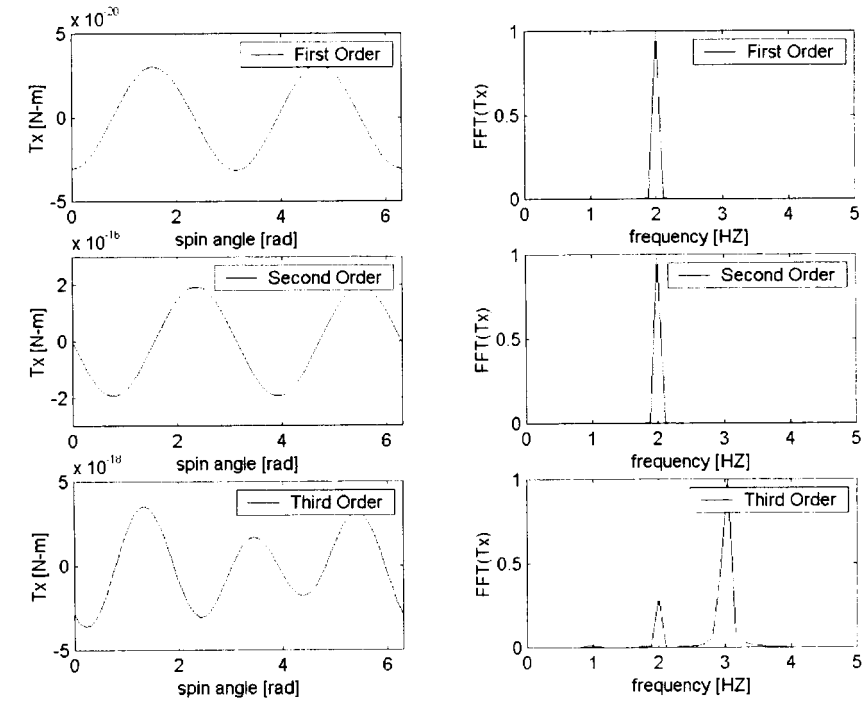

Figure 56 Ordered Torque and harmonics at Point 5 due to Capsule Attraction

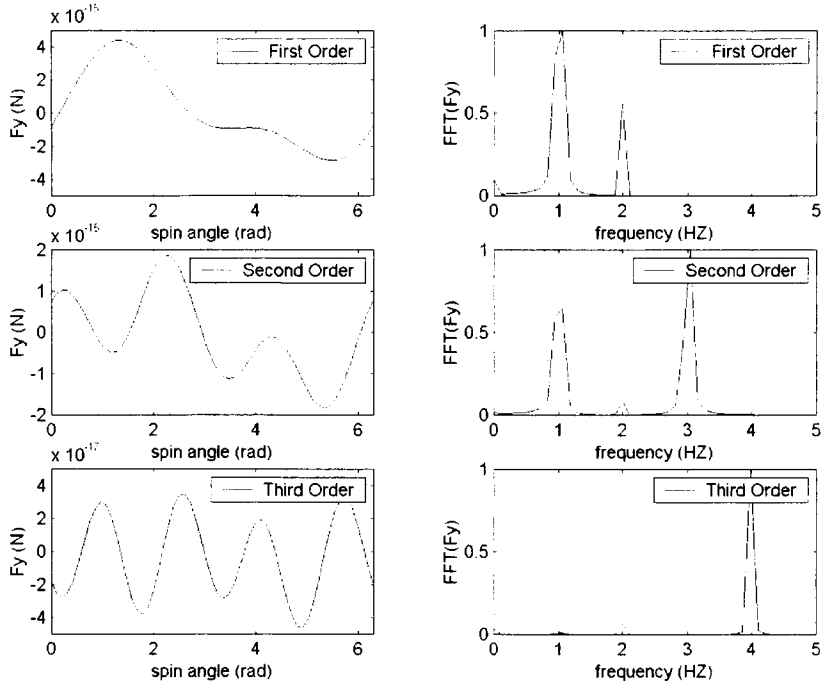

Figure 57 Ordered Force and harmonics at Point 6 due to Capsule Attraction

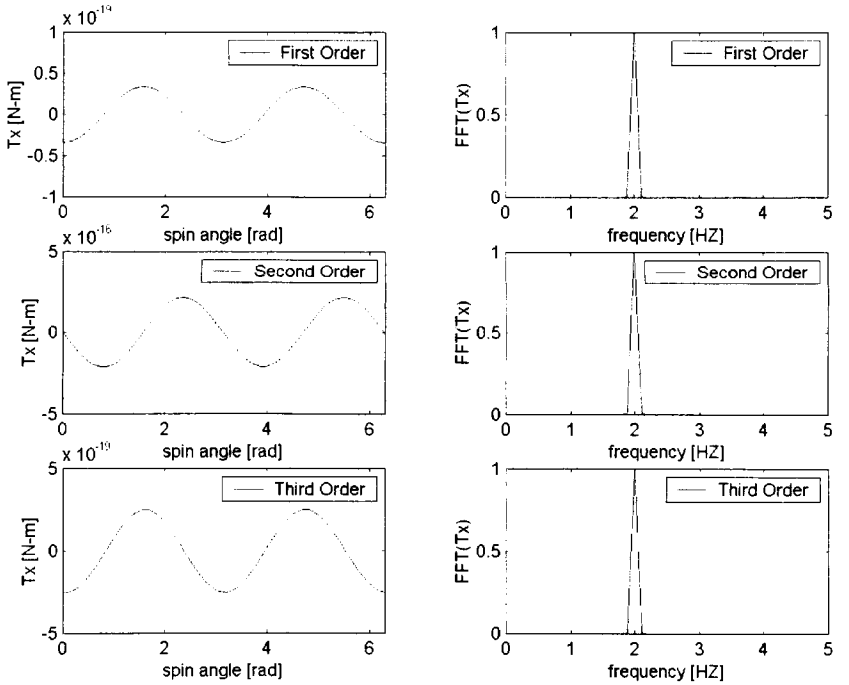

Figure 58 Ordered Torque and harmonics at Point 6 due to Capsule Attraction

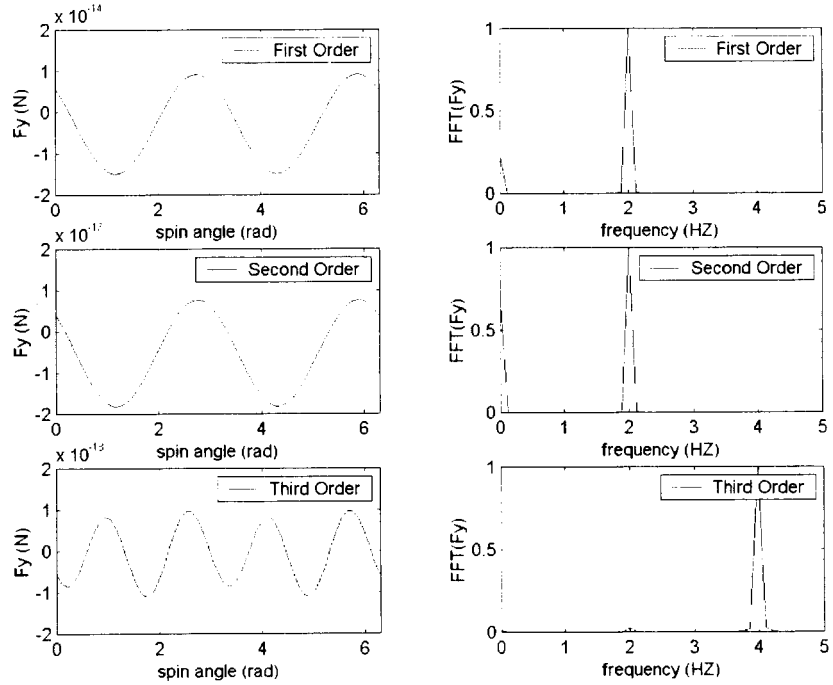

Figure 59 Ordered Force and harmonics at Point 7 due to Capsule Attraction

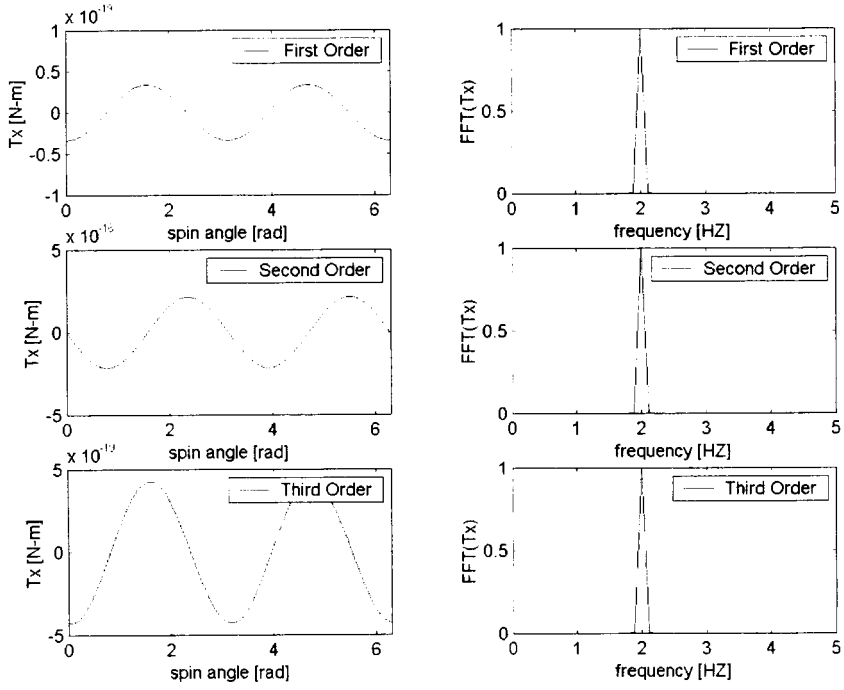

Figure 60 Ordered Torque and harmonics at Point 7 due to Capsule Attraction

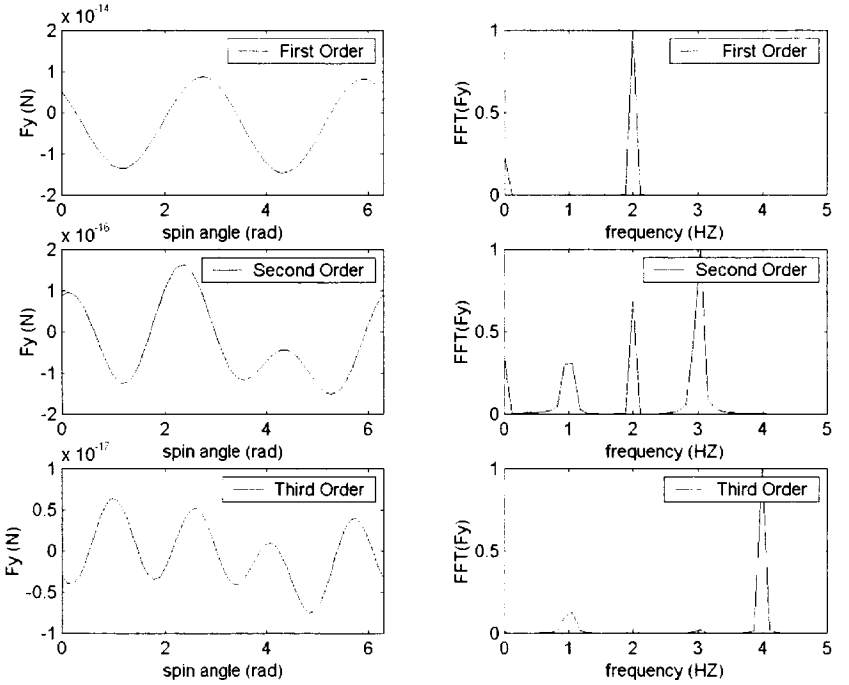

Figure 61 Ordered Force and harmonics at Point 8 due to Capsule Attraction

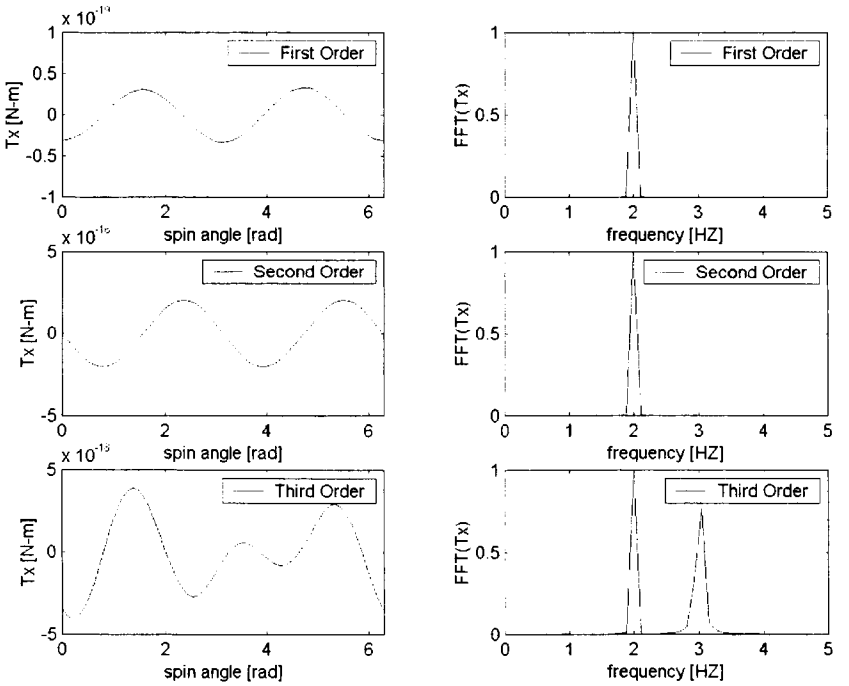

Figure 62 Ordered Torque and harmonics at Point 8 due to Capsule Attraction

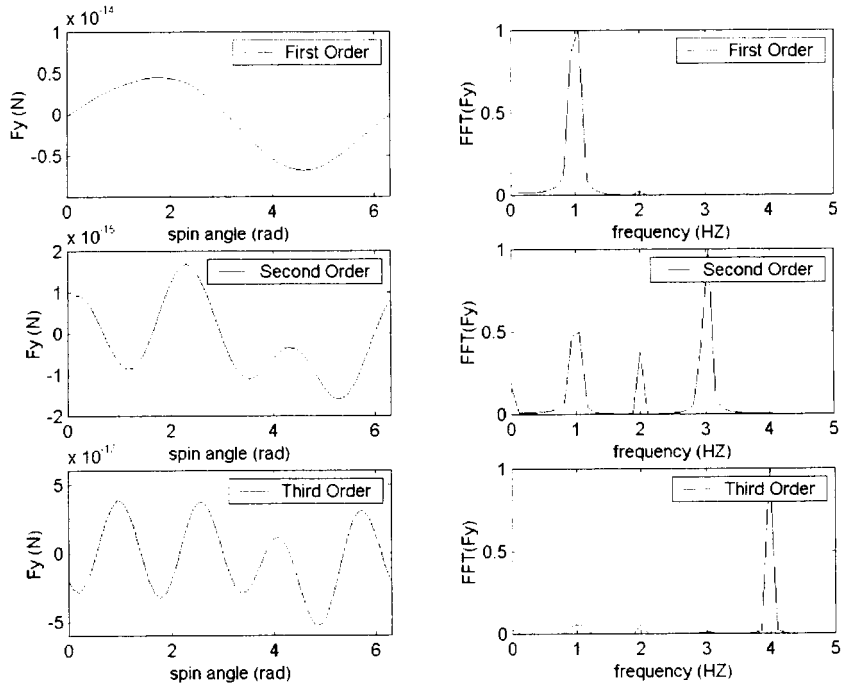

Figure 63 Ordered Force and harmonics at Point 9 due to Capsule Attraction

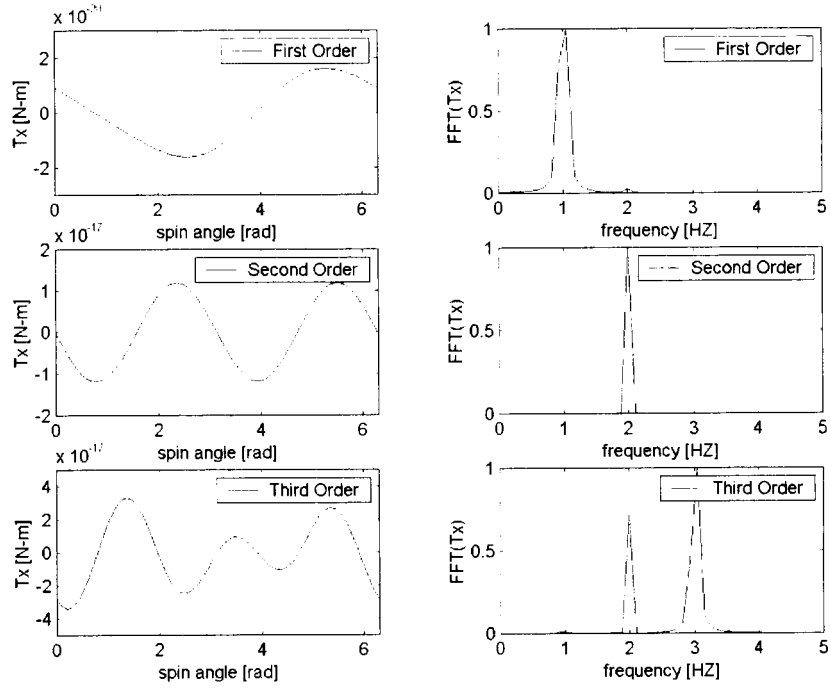

Figure 64 Ordered Torque and harmonics at Point 9 due to Capsule Attraction

The frequency spectrum for the force and the torque are shown in the following tables. The dominant frequencies are in bolded face.

Table 3 Frequency spectrum along the capsule axis

	First Order	Second Order	Third Order
F_x	P0, **P2**	P0, P1, **P2**, **P3**	P2, **P4**
T_x	**P2**	**P2**	P2, **P3**, P4

Table 4 Frequency spectrum to the side of the capsule axis

	First Order	Second Order	Third Order
F_x	P0, **P2**	P0, P1, **P2**, **P3**	P1, P2, P3, **P4**
T_x	**P2**	**P2**	P1, **P2**, **P3**

Table 5 Frequency spectrum close to the cap

	First Order	Second Order	Third Order
F_x	**P1**, **P2**	P1, P2, **P3**	P1, P2, P3, **P4**
T_x	**P1**, **P2**	P2	P1, **P2**, **P3**

The orders in the above tables are the following. Order 1- offset or inertia order 1, $O(1/R^3)$ in force. Order 2- inertia order 2, degenerates to MacCullagh formula for a perfect body (or with respect to the principal axes), $O(1/R^4)$ in force. Order3- inertia order 3, $O(1/R^5)$ in force.

It is important to emphasize that the relative orders depend on the mass imperfection. For example, we should not rush to a conclusion regarding the contribution of the offset. The dominant contribution for a perfectly symmetrical body is from the second order. In

this case the torque is in agreement with the MacCullagh formula. The spectrum related to the second order can be deducted by noticing that the direction cosines, m and n, have period one: $m \rightarrow P1$, $n \rightarrow P1$. Therefore,

$$Tx \approx (Izz - Iyy)\,m\,n \rightarrow P2,\ Ty \approx (Ixx - Izz)\,n \rightarrow P1,\ Tz \approx (Iyy - Ixx)\,m \rightarrow P1.$$

Note that Iyy~Izz, thus both the offset term and MacCullagh term are amplified by the offset. Tx is null for a perfectly symmetrical body. Ty and Tz show various frequencies. However, Ty and Tz acting on a perfectly symmetrical body contribute P1 according to MacCullagh formula. Also note that order 4 may play a role as well, because we assumed equal principal inertia of order 2. This assumption nulls the perfect body contribution of the second order but it does not cancel completely the term of order 4.

The frequency P1 is dominant only at the extreme location (point 9), due to the offset. We investigated the vicinity of this point, and found that the amplitude of P1 decreases as we move farther from the cap.

Concluding Remarks

We presented an analytical and a numerical analysis of the gravitational perturbations acting on the test mass due to the capsule. The outcome of this work is a closed-form formulation for the force/torque as well as a robust and interactive computer code.

Our analysis predicts that the gravitational perturbations, acting on the test mass due to the capsule attraction, are safely within the limit required by the experiment. Moreover, along most of the test mass trajectory, the perturbations are far smaller than the limit, and their frequencies are different from the modulation frequency.

The conclusions from our investigations, concerning the test masses are:

- The test masses should be smaller than about 10 cm and lighter than about 2 kg.
- The second order principal moments of inertia should be equal within construction tolerances $\delta L/L < 10^{-4}$.
- There is no need for belted cylinders (as used in the STEP satellite experiment) for the accuracy target of this experiment.
- The test masses should be as perfect as possible in terms of their mass distribution ($\delta M/M \sim 10^{-4}$).

The investigation carried out is essential for the definition of the tolerable sizes, masses, characteristics of the moments of inertia, and construction accuracy of the sensing masses.

RELEASE/LEVELING MECHANISM DEVELOPMENT

Introductory remarks

The leveling and release mechanism must be able to release the detector with initial conditions that do not impair the accuracy of the science measurement. Once the effects of the higher-order mass moments on the proof masses are made negligible through the right shapes and sizes, the most important external perturbation is the Earth's gravity gradient. Other perturbations are of course present but they can be made negligible through thermal design, reducing the pressure inside the detector, and shielding the detector from magnetic disturbances. The noise components associated with the Earth's gravity gradient manifest themselves at twice the spin frequency and (depending on the orientation of the spin axis) at the spin frequency. The latter are the damaging components. The gravity component of importance to us is the g_{xy} where x is the spin axis and y the sensitive axis of the accelerometer. As shown in Ref. x, this component is proportional to the product $\phi\delta_x$ where ϕ is the elevation angle of the (body) symmetry axis with respect to the horizontal plane (defined by the local gravity) and δ_x is the centering error along the spin axis between the CMs of the proof masses. The formulas derived in Ref. x for the Earth's gravity gradient components will be utilized at the end of this section to set a limit on the tolerable tilt angle at release.

Additional harmonic components come from the rotational dynamics of the instrument package. These harmonics are related to the inertia characteristics of the package and the rotational velocity errors at release. In summary, the leveling and release mechanisms must provide an orientation of the spin axis close to horizontal (to reduce the Earth's gravity gradient component) and rotational velocity errors sufficiently low to avoid saturation of the accelerometer output.

The detector has also its own elastic dynamics (as shown in previous section) which is excited by the conditions at release. We can conservatively assume that the release will excite the elastic dynamics of the detector up to its end of scale. The experiment strategy is to damp the elastic oscillations through electrical dissipative forces (see later on for experimental results) exercised for a few seconds after release. Once the elastic (natural) oscillations are abated to a level well within the dynamic range of the instrument, the electrical dissipative forces are removed and the detector operates as a high-Q detector. After the natural oscillations are abated, the oscillations of the proof masses will be forced by the rotational dynamics of the detector during the fall.

In order to understand the effects of initial errors at release upon the differential accelerometer output, we need to develop a simplified model of the accelerometer. This model must contain the key dynamical elements but must also have a sufficiently simple formulation that shows analytically the origin and frequency content of the proof masses acceleration.

Simplified dynamical model

The differential accelerometer consists of proof masses that are about twenty times lighter than the mass of the instrument package. Moreover, the proof masses are expected to move with respect to the CM of the whole package by only microns during the early transient phase and by nanometers during most of the fall. Consequently, the rotational dynamics of the package is unaffected (and this will be confirmed in follow-up analyses) by the tiny motions of the proof masses. On the contrary, the rotational dynamics of the package drives the motion of the proof masses. In summary and with a good degree of approximation, the rotational dynamics of the package can be assumed to be steady. The solution of the attitude motion of the rigid body is available in close form for a free spinning body. We need to right the equation of a proof mass that is mechanically constrained to the rotating (and wobbling) instrument package in order to understand the origin and frequency content of the acceleration output of a single proof mass. The analysis can be readily extended to two proof masses.

The general expression for the acceleration of a test mass at point **P** with respect to **O** in a rotating system F can be written in matrix form as:

$$[\dot{\omega}]\begin{Bmatrix} x \\ y \\ z \end{Bmatrix} + [\omega][\omega]\begin{Bmatrix} x \\ y \\ z \end{Bmatrix} + 2[\omega]\begin{Bmatrix} \dot{x} \\ \dot{y} \\ \dot{z} \end{Bmatrix} + \begin{Bmatrix} \ddot{x} \\ \ddot{y} \\ \ddot{z} \end{Bmatrix} = \{a_P - a_O\} \tag{7}$$

where $[\omega]$ is the angular rate matrix of the reference system and $\{x\ y\ z\}^T$ the position of the point **P** with respect to the center of the reference system **O** (placed at the instrument package CM).

For a rigid body the equations are projected onto the axes attached to F itself (body axes) where the position vector is assumed fixed with respect to the center of F.

Consequently, eqn. (7) transforms into:

$$[\dot{\omega}]^B \cdot \begin{Bmatrix} x \\ y \\ z \end{Bmatrix}^B + [\omega]^B[\omega]^B \begin{Bmatrix} x \\ y \\ z \end{Bmatrix}^B = \{a_P - a_O\}^B \tag{8}$$

Where the angular rate matrix projected onto the body axes can be computed from the rotation matrix that relates the body axes to an inertial system:

$$[\omega]^B = R_{IB}\dot{R}_{BI} = \begin{bmatrix} 0 & -\omega_z & \omega_y \\ \omega_z & 0 & -\omega_x \\ -\omega_y & \omega_x & 0 \end{bmatrix} \tag{3}$$

After substituting eqn. (9) into (8), we derive the well-known acceleration matrixes that provide the acceleration gradient at the point **P** with respect to **O** as observed by the rotating observer (or equivalently a proof mass of the detector):

$$[C] = \begin{bmatrix} \omega_y{}^2 + \omega_z{}^2 & -\omega_x\omega_y & -\omega_x\omega_z \\ -\omega_x\omega_y & \omega_z{}^2 + \omega_x{}^2 & -\omega_y\omega_z \\ -\omega_x\omega_z & -\omega_y\omega_z & \omega_x{}^2 + \omega_y{}^2 \end{bmatrix} \quad \text{centrifugal acceleration matrix}$$

$$[E] = \begin{bmatrix} 0 & \dot{\omega}_z & -\dot{\omega}_y \\ -\dot{\omega}_z & 0 & \dot{\omega}_x \\ \dot{\omega}_y & -\dot{\omega}_x & 0 \end{bmatrix} \quad \text{Euler acceleration matrix}$$

Consequently, the (apparent) acceleration gradient tensor (in body axes) between a point **P** and the system CM at **O** is:

$$[A] = [C] + [E] \tag{10}$$

In order to compute the expression of ω_x, ω_y, ω_z we need to consider the dynamics of the instrument package that houses the detector. In other words, we must solve the Euler equations for the free-torque case of a rigid body. We will consider an inertially axisymmetric body and regard x as the longitudinal axis of inertial symmetry. The non-symmetric body also has a known solution but it is more complicated as it involves elliptic integrals.

After setting v = component of the angular rate along the axis of symmetry, the well-known solution of the Euler equations is obtained as follows:

$$\begin{cases} \omega_x = \nu \\ \omega_y = -\omega_t \cos(\Omega t) \\ \omega_z = \omega_t \sin(\Omega t) \end{cases} \tag{11}$$

in which the origin of t is at the time when ω_y attains its maximum value and where:

$$\Omega = \frac{I_t - I_x}{I_t}\nu \quad \text{(body precession rate)}$$

$$\omega_t = \sqrt{\omega_y^2 + \omega_z^2} = \sqrt{\omega_{y0}^2 + \omega_{z0}^2} \qquad \text{transverse angular velocity}$$

The quantities ω_{y0} and ω_{z0} are the initial components of the angular velocity orthogonal to the symmetry axis. In our case, they can be interpreted as the rotational velocity errors at release of the instrument package.

After substituting eqn. (11) into the matrices [C] and [E], we obtain the component of the overall acceleration gradient matrix:

$$a_{xx} = -\omega_t^2$$

$$a_{xy} = a_{yx} = -\omega_t \cos(\Omega t)(\Omega - v)$$

$$a_{xz} = a_{zx} = -\omega_t \sin(\Omega t)(\Omega - v)$$

$$a_{yy} = \frac{1}{2}\omega_t^2\left[1 - \cos(2\Omega t)\right] + v^2$$

$$a_{yz} = a_{zy} = -\frac{1}{2}\omega_t^2 \sin(2\Omega t)$$

$$a_{zz} = \frac{1}{2}\omega_t^2\left[1 + \cos(2\Omega t)\right] + v^2$$

The acceleration vector a measured at P and projected onto the body axes, is simply:

$$\{a\} = [A]\{d\} \tag{12}$$

where $\{\delta\} = [\delta_x, \delta_y, \delta_z]^T$ is the position vector from **O** to **P** (we have changed the notation to the δs to highlight the fact that we are dealing with very small distances). The component of the acceleration orthogonal to the symmetry axis (i.e., along the sensitive axis of the accelerometer) is as follows:

$$a_z = -\omega_t(v - \Omega)\cos(\Omega t)\delta_x + \frac{1}{2}\omega_t^2 \sin(2\Omega t)\delta_y + \left[v^2 + \frac{1}{2}\omega_t^2\left(1 + \cos(2\Omega t)\right)\right]\delta_z \tag{13}$$

This acceleration is the dominant acceleration experienced by the proof mass once the natural oscillations have been abated. In fact the amplitude of the residual natural oscillations can be made orders of magnitude smaller than the magnitude of the δ vector through the initial damping. Equation (13) highlights several important points as follows: (1) the rotational velocity errors at release (encapsulated into ω_t) combine with the displacement error δ to produce an acceleration output along the sensitive axis; and (2) this acceleration component is modulated by the body precession rate and not by the spin frequency. This fact was observed previously in the results of the general elastic model of the detector. The conclusion is very important because it implies that the errors at

release do not impact directly the harmonic component of a possible EP signal violation (that appears at the spin frequency). The overall advantage of the gyroscopic body (with non-spherical inertia ellipsoid) is that the precession rate is different from the spin rate. Moreover, the precession rate can be chosen at will by selecting the ratio of the moment of inertia of the instrument package in order to be less damaging to the ability of extracting the signal from the noise. Since both ω_p and 2 ω_p appear in the expression of the acceleration, it is advisable to make ω_p non commensurate with v (the spin rate). The selection of the moments of inertia ratio (and hence ω_p) and the ability to extract a signal with a strength at the threshold sensitivity of the detector will be carried out in next year analysis.

Derivation of requirements

The first requirement derives directly from the analysis carried out in Ref. x and it is related to the strength of the components of the Earth's gravity gradient at the spin frequency. The resulting acceleration component (from Ref. x) is

$$\delta a_z < 3\frac{\mu}{R^3}\cos(\phi)\sin(\phi)\sin(vt)\delta_x + \frac{3}{2}\frac{\mu}{R^3}\cos^2(\phi)\left[\sin(2vt)\delta_y + \cos(2vt)\delta_z\right] + \frac{\mu}{R^3}\left[\frac{3}{2}\cos^2(\phi) - 1\right] \quad (14)$$

for an instrument package spinning about x, a sensitive axis along z, and ϕ the elevation angle of the symmetry axis with respect to the horizontal plane defined by the local (gravity) vertical. Equation (14) highlights the three components produced by the Earth's field at the spin frequency, at twice the spin frequency, and a dc term. The strength of the gravity gradient component at the spin frequency must be less than the threshold signal at $5x10^{-15}$ g. A product $\phi\delta_x$ of 0.1 deg-micron will safely meet the previous condition. Consequently, we can either be more relaxed on the leveling/release mechanism (i.e., $\phi <$ 1 deg and $\delta_x < 0.1$ micron) or on the centering between the two proof masses along the spin axis (i.e., $\phi < 0.1$ deg and $\delta_x < 1$ micron). Both options will be kept open for the time being because they involve several technical considerations related to the mechanization of the leveling/release mechanism and the calibration of the differential accelerometer. A choice between the two options will be searched for after a dynamic analysis of the release mechanism and laboratory tests on the differential accelerometer prototype to assess the difficulties involved with the accurate centering of the proof masses along the spin axis.

The requirement on the rotational velocity errors at release can be readily obtained from the following considerations. First, the rotational velocity error must be sufficiently small not to saturate the instrument output. In this case we do not have to worry about the instrument sensitivity because with appropriate inertia characteristics there will be no components at the spin frequency related to the precession dynamics of the instrument package. In this case the stronger component is associated with the first term of eqn. (14).

A rotational velocity of 1 deg/s will only produce a signal of order 10^{-9} g which is well within the dynamic range for the expected values of spin and precession frequencies.

However, we must also worry about the amplitude of the precession (i.e., the nutation angle) because through coning of the body axis the accelerometer will sense the Earth's gravity gradient. The frequency sensed through coning is not exactly the spin frequency because the coning adds a frequency modulation at the precession frequency. Nevertheless, we will assume conservatively that the amplitude of the nutation angle must be less than previously indicated for the gravity gradient related noise. For an axisymmetric body the amplitude of the body-axis coning (i.e., the nutation angle) is as follows:

$$\tan(\theta) = \frac{I_t}{I_a}\frac{\omega_t}{v} \tag{15}$$

where ω_t is the transverse angular velocity at release, I_a and I_t are the moments of inertia about the transverse and the symmetry axis (x-axis in our case), respectively. If we assume an upper bound for the nutation angle of 1 deg, a spin frequency of 0.5 Hz and a (worst-case) inertia ratio $I_t/I_a \approx 3$, we obtain $\omega_t < 1$ deg/s. Likewise, if we had assumed a maximum $\theta < 0.1$ deg then we would have obtained $\omega_t < 0.1$ deg/s. In summary, we will establish the following two sets of requirements

a) $\delta_x < 1$ μm (centering error between proof masses CMs along the spin axis)
   $\phi < 0.1$ deg (verticality)
   $\omega_t < 0.1$ deg/s (angular rate error at release)

b) $\delta_x < 0.1$ μm (centering error between proof masses CMs along the spin axis)
   $\phi < 1$ deg (verticality)
   $\omega_t < 0$ deg/s (angular rate error at release)

We will start by base lining the release and leveling mechanism according to option a while keeping option b open if the tight centering of the proof masses of the detector turns out to be feasible.

Release sequence

The release of the package takes place in 2 stages. Initially the overall instrument is released from the balloon. Then, very soon after, the sensor package is released, in two steps, within the vacuum chamber.

Overall Instrument Release

The combination of wind shear during ascent, the extremely low air resistance at float, and the limited time at float make it necessary to assume that the balloon will be rocking at the time of package release. Since it is required that the package be vertical, and non-spinning through out the experiment, the release strategy must account for this. The present concept, developed in the reporting period, is to actively separate the orientation dynamics of the instrument from the behavior of the balloon. That is, we have placed a 3-axis gimbals between the instrument release mechanism and the portion of the gondola that stays with the balloon.

As the balloon rockets back and forth, and rotates, the gimbals will be driven to ensure that the instrument package angular orientation is unchanged. The sole effect being that the package will be translating back and forth, and moving up and down slightly. During this process the linear motion will be tracked from the ground. In order to ensure that we release the package when it is as close to unaccelerated as possible, we will release it at one of the extremes of the balloon pendulum swing.

Since the sensor release does not have any orientation adjustment capability, the overall instrument release mechanism must be designed to meet all the alignment and stability requirements that cover the release of both the instrument capsule and the sensor.

Sensor Release

The sensor release concept involves a two stage support. The first stage is a simple spit that holds the sensor package through release of the overall instrument from the balloon. Once the capsule is in free-fall the sensor release mechanism pulls back far enough to disengage the spit, and draw it to a position that the sensor will not hit it on the way down. At this point the sensor is held between 6 springs, 3 on each side. These springs will be sized so that they can not impart more force than is allowed by the rotation stability requirements. Any transient sensor motion induced in the spit-support release will be allowed to damp out in the 6 spring. Once the instrument package is spinning at a stable rate, and oscillation from the initial stage of the release have damped, the mechanism second stage will pull back further, and the instrument will drop.

The next stage of the work on this design will be to create a detailed simulation of the entire system, in order to examine its behavior in detail.

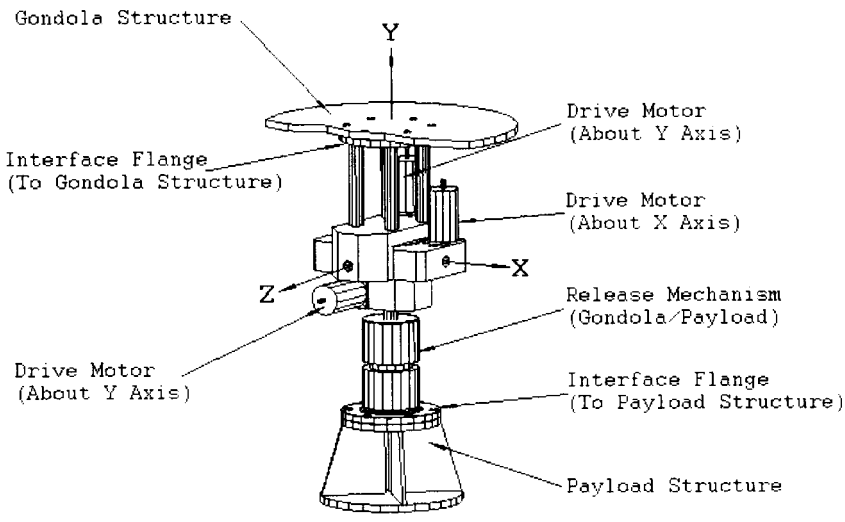

Figure 65 Schematic of leveling mechanism

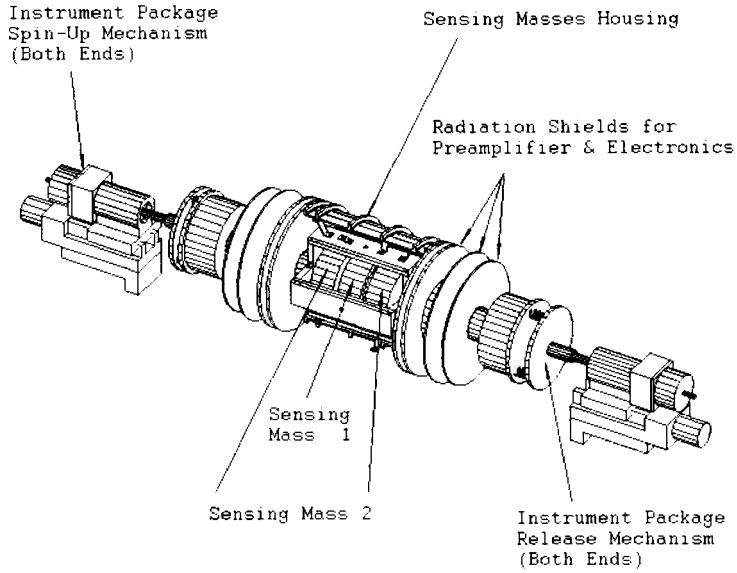

Figure 66 Instrument package spin-up and release mechanism

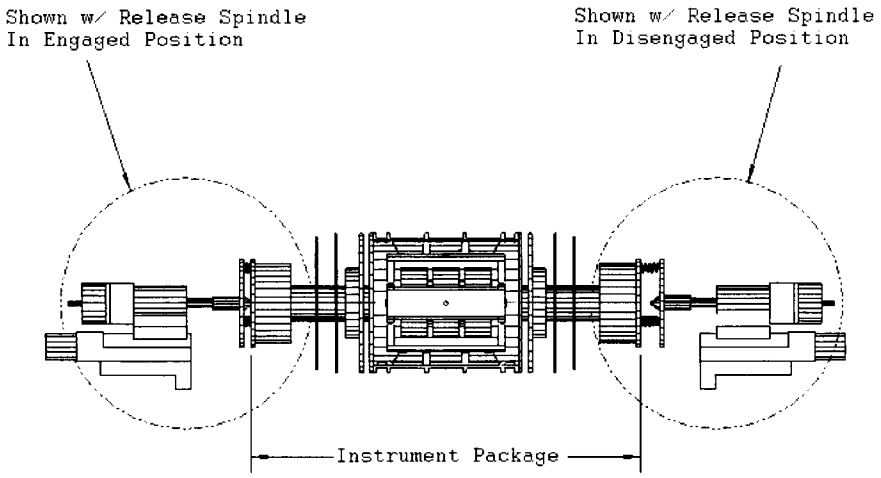

Figure 67 Front view of release mechanism

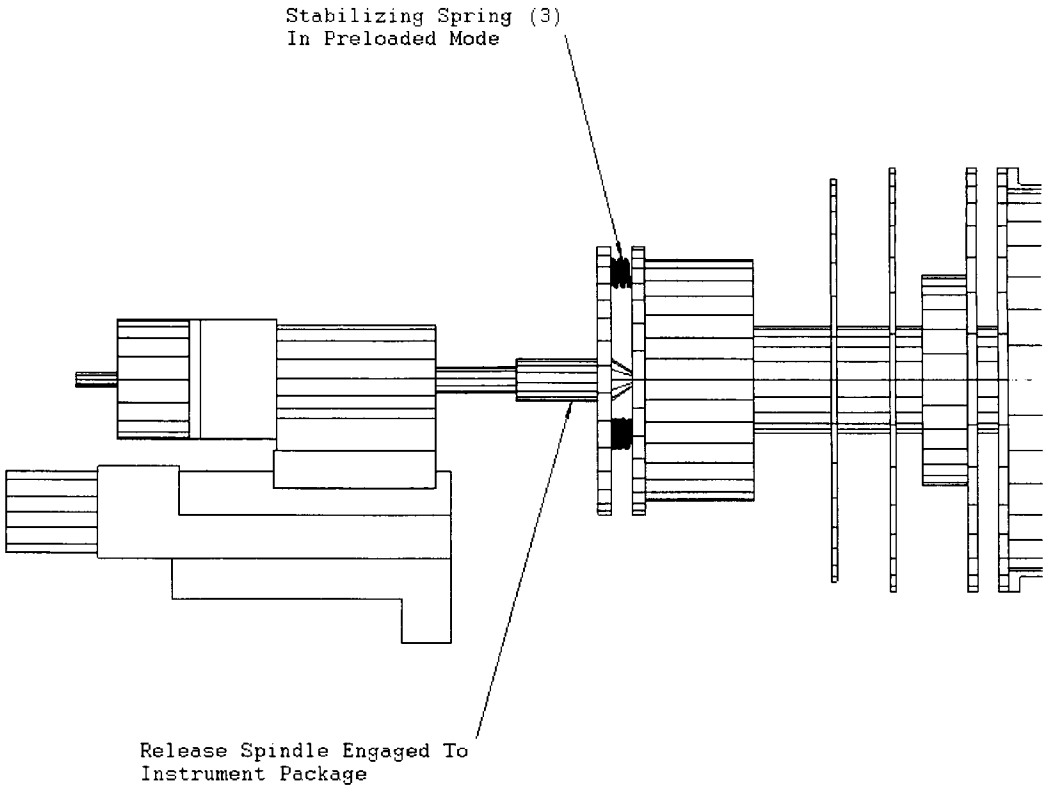

Figure 68 Detail of release mechanism (with spindle engaged)

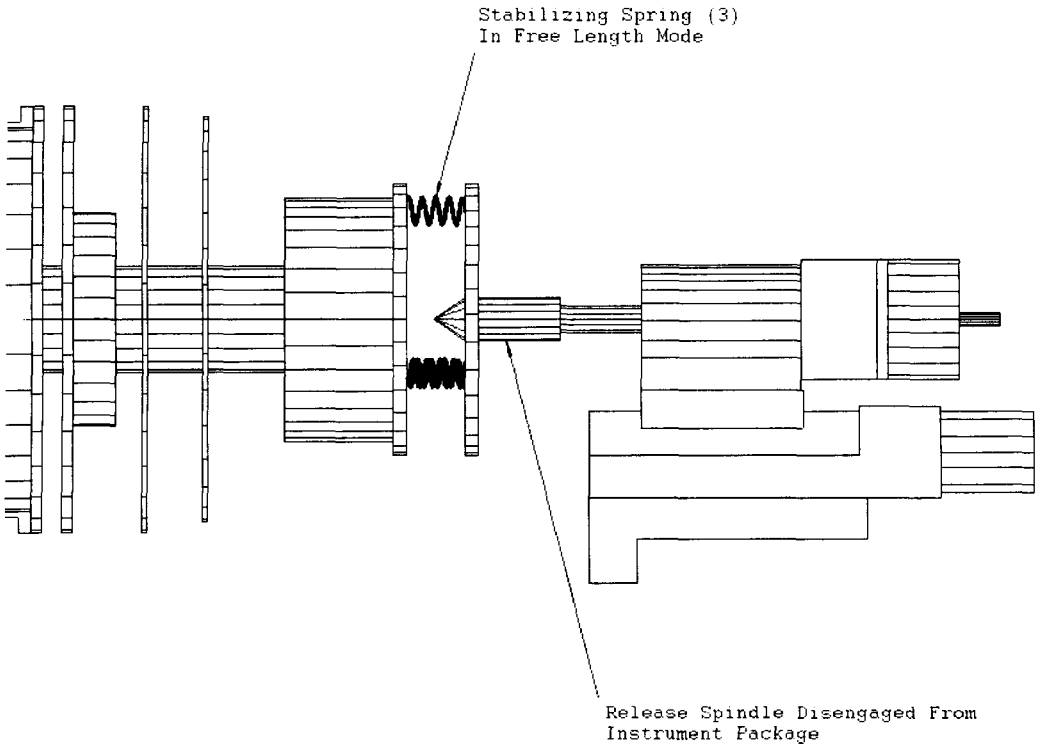

Figure 69 Detail of release mechanism with spindle disengaged and springs still engaged

Thermal Design

One of the key advances this year was in the area of the thermal design and increased detail in the thermal model. In order to assist in this area the main supporting structure for the sensor package had to be sized. Though most of the instrument design remains at the concept level, it became important to examine the design forces that controlled this component's dimensions. The sizing involved balancing the need to minimize the heat transfer, and therefore the support's cross sectional area, while at the same time minimize the support deflection, or therefore the support's structure moment. Studies of viable cryogenic materials suggested that a Kevlar composite would be the best material to use. Since we intent to use a composite material, and by the nature of the design, one with a thin wall, a further constraint on the design was a limitation on the allowable compression load. Coupling these requirements we were able to size the main shaft in such a way that is can support the instrument without allowing out-of-spec instrument deflection, while dropping thermal conductivity well below the allowable level.
Below are the present support parameters:

- Length = 0.12m
- Diameter = 0.05m
- Wall thickness = 0.0012m
- Kt/m = 1.9×10^{-5} W*m/K, at 10°K

Cool down Techniques

Though this will be covered in more detail in the thermal section, the preferred method for lowering the instrument temperature to 10K has been re-examined and changed. Initially we had examined using radiation alone to reduce the instrument operation temperature to 10K. It was quickly clear that this approach was inadequate. Next we examined having a cold strap in place prior to launching the balloon. We would then rely on just radiation from the cold Dewar walls to maintain the temperature. Though this is effective, it introduces issues related to manipulating the cold strap.

To avoid this we have since base lined a third approach, one involving cooling the instrument down by flowing cooled GHe through the vacuum chamber until the instrument is cool. We would then pumping out the remaining GHe from the inside of the Dewar. This give us a fast way to cool the instrument without having to manipulate a cold strap.

Dewar Operation Techniques

One of the larger instrument dynamics stability issues that needs to be addressed is the effects of the liquid cryogens during free fall:

- the fact that they may slush during the fall
- the fact that they will continue to boil during the fall
- the fact that they needs to be vented, which will cause a propulsion effect.

In order to avoid these effects we are beginning to examine novel Dewar operation techniques. The standard approach for maintaining temperatures at this level is a Dewar with a vacuum shroud and 2 cryogen shrouds, LN2 and LHe. But the LN2 is heavy. It can slush, it tends to boil similarly to water, and when it is vented it produces some propulsion, all of which will cause some dynamic reaction in the Dewar that could disrupt the experiment. The LHe, on the other hand is quite light and is far less likely to cause a dynamic disturbance.

For these reasons we have decided to examine operating the Dewar, at least through the experiment phase, without LN2. The first approach that we examined was allowing the LN2 to completely vent prior to dropping the experiment package from the balloon. This is an acceptable approach, though it does produce some limitation on system timing. We would rather be able to begin the experiment when the system is settled, rather than waiting longer for the LN2 to boil off. Instead we are going to examine the possibility of allowing the LN2 boil off on the ground, and then flowing the boiled off LHe into LN2 shroud.

Dewar Layout

We have moved the Dewar opening from the top of the chamber to the bottom. The initial Dewar design had the opening for inserting the instrument package into the top of the Dewar. This meant that all the feedthroughs into the system, as well as all the service feedthroughs for the Dewar itself were broken anytime the Dewar was opened. In addition, the load path from the balloon to most of the instrument mass goes through this connection. By moving the opening to the bottom, all the feedthroughs remain intact when loading the system, and only the instrument crash protection is supported through the Dewar cover (bottom plate).

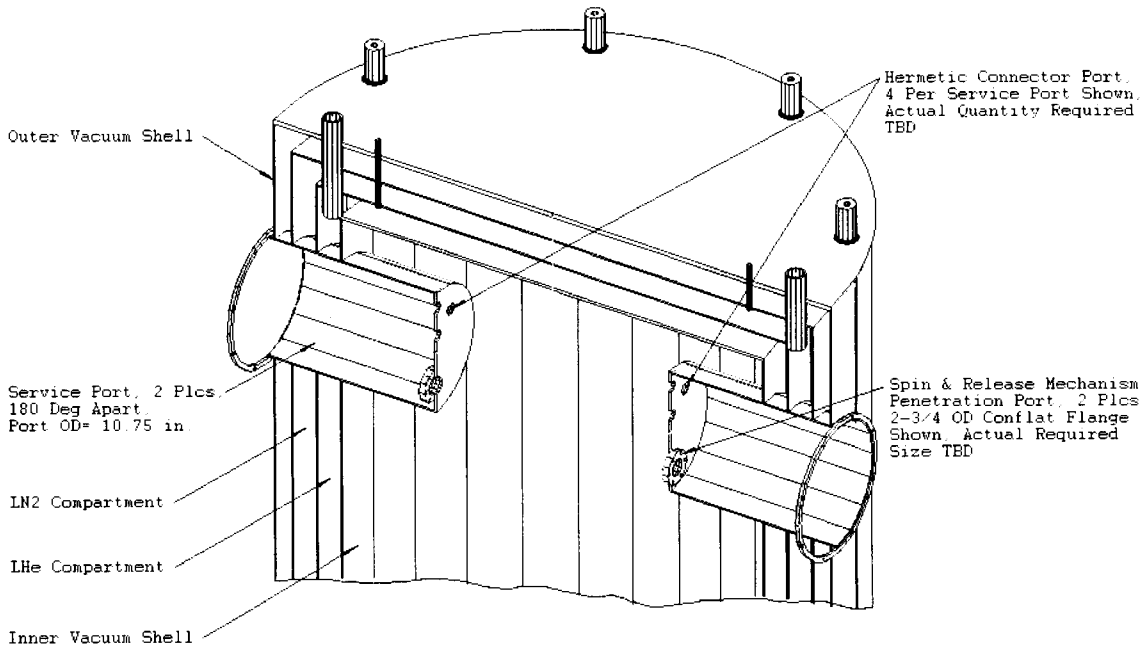

Figure 70 Cryostat top detail with feedthrough interfaces

THERMAL ANALYSIS

The simplified model discussed previously has been further developed, particularly in the area of isolation of the sensor from the (relatively) warmer preamp and electronics module. In fact, the electronics has to be kept above a minimum temperature (for this model, we have assumed –65C) to prevent damage to the components, and possibly needs to be warmed further to a "cold-start" temperature at the initiation of experiment calibration.

The design consists of a sensor supported by a Kevlar-reinforced shaft (discussed previously) that is suspended by the rotation fittings across the dewar diameter. We have assumed the electronics module and preamp are balanced disks supported by this same shaft, both to one side of the centrally located sensor module. Between these various elements we have places radiation shields to minimize views of the warmer elements to the sensor. The model representation is shown in Figure 71.
The electronics are shown in red as a result of their maintained temperature; the preamp is just visible between the two largest disks.

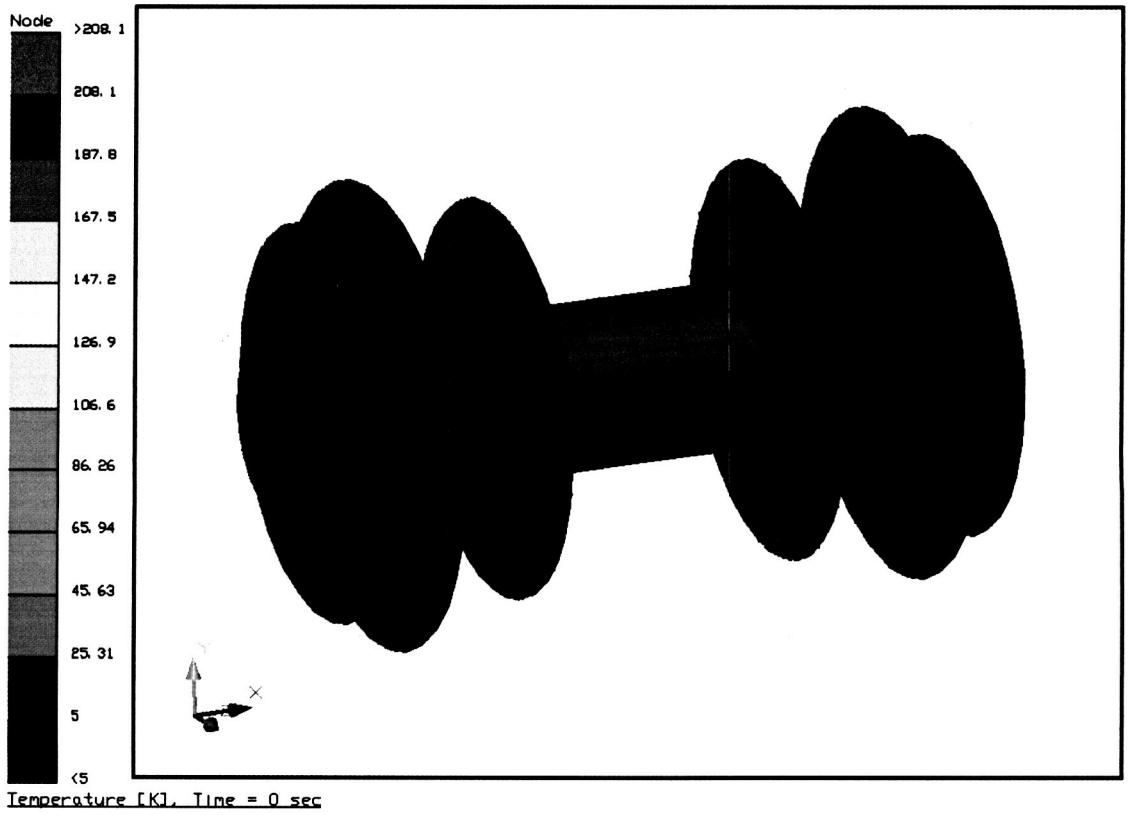

Figure 1 Thermal model representation

We have assumed that during the entire process (including cool down of the experiment) that the electronics is maintained above –65C, as illustrated by the red disk at the left end of the figure.

There are two fundamental conductive paths between the various elements in the model: the supporting shaft and the wires connecting the electronic elements. The hollow shaft has been sized to support the masses with sufficient stiffness to allow the experiment to be balanced. The wires (currently assumed to be 4 pairs between each module) have been sized to provide less than 1-ohm resistance per circuit. Pure-metal wire like copper or silver have sharply peaked thermal conductivity in this temperature regime (10-25K) as well as rapidly changing electrical conductivity, so we have assumed for this analysis that the wires are Constantan, which has very little change in electrical characteristics from room temperature down to 4K, but its thermal conductivity drops by a factor of 100, providing effective thermal isolation at the experiment temperature. The conductors in the model have been sized to accurately represent the shaft and wires, and all the important materials are modeled with temperature-varying conductivity and specific heat.

It has been shown in earlier studies that the experiment cannot be cooled effectively by radiative exchange with the dewar alone – it requires the addition of a thermal strap to achieve the desired starting temperature in a reasonable period of time. However, a mechanical strap (or straps) adds several complications to the design. The largest mass is the sensor itself, yet this is the least desirable location to affix a strap. We are currently considering an alternative approach: to flow gaseous helium over the experiment to cool it. This has the advantage that after starting conditions are achieved; the helium can be pumped out, allowing us to take advantage of the effective isolation of the mechanical hardware.

We have run a study of the warm-up of the preamp and experiment with nominal power inputs and the previously mentioned initial condition of the electronics module at 208K (-65C). Using an assumed cooling of the preamp based on area ratio to the sensor and heat flow through the wires, the equilibrium temperature of the preamp prior to startup is approximately 20K. Using these initial conditions, and wires and support tube modeled as described above, the temperature rise of the preamp and the temperatures and estimated gradients in the sensor are shown in Figures 72 and 73.

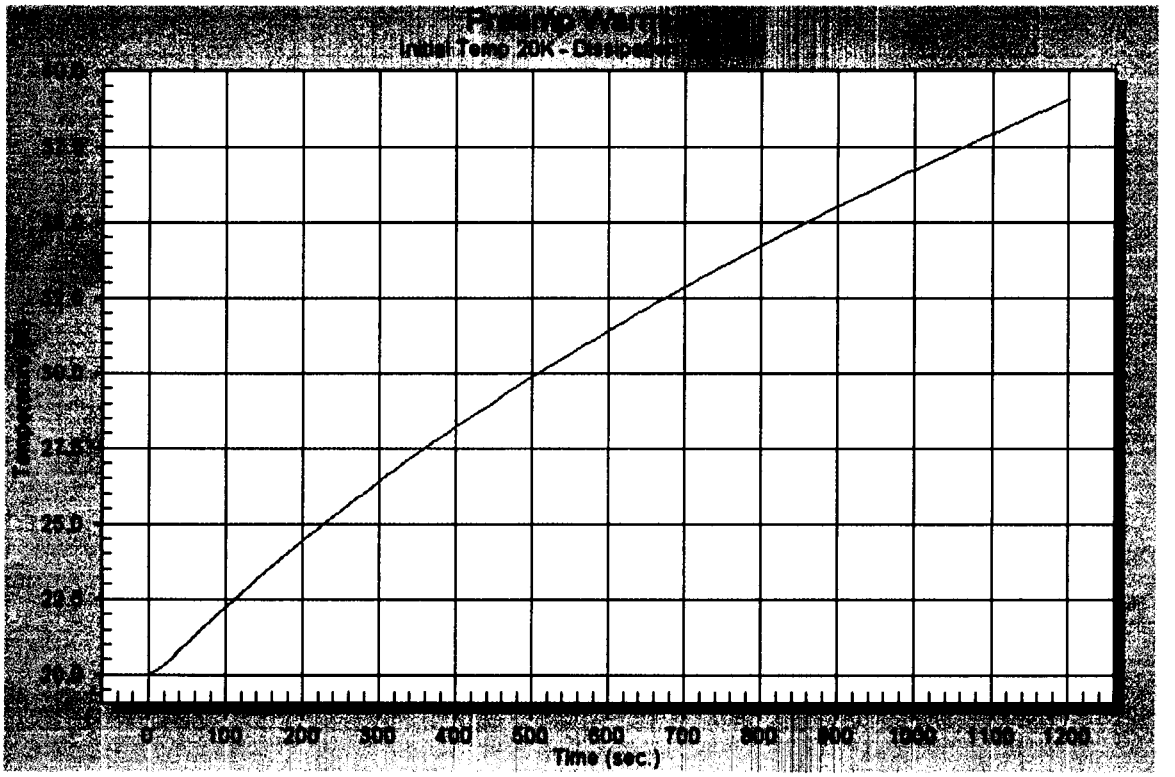

Figure 2 Temperature rise of preamplifer during calibration

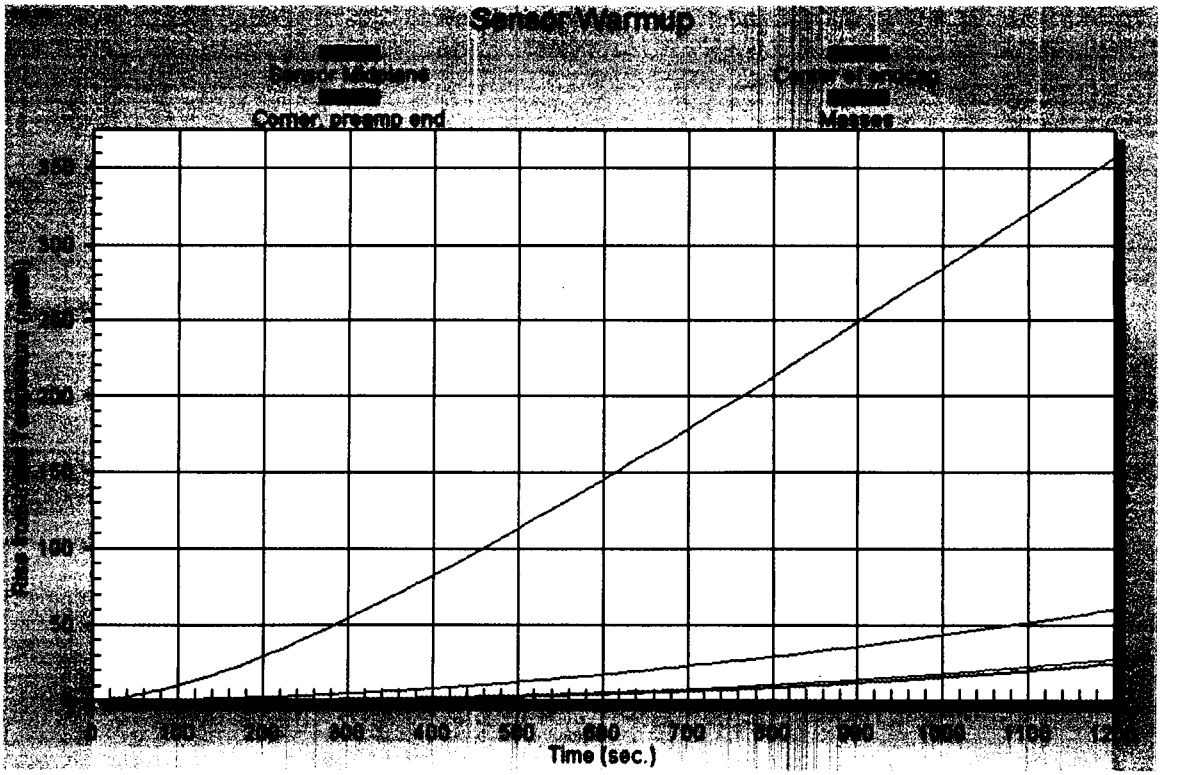

Figure 3 Temperature rise at various locations of sensor

This study has yielded several significant conclusions for the design of the experiment:

- Properly sized alloy wires provide sufficient electrical conductance without significant impact on the thermal performance
- The most significant thermal conductance is the shaft supporting the sensor and other modules.
- Radiative heating of the sensor can be well controlled with concentric disks between modules. These disks, if of significant thickness, also provide thermal mass to slow the heating of the sensor.

It should be noted that while the temperature rates of change fall within the previously described limits (current estimate of maximum temperature in sensor is 0.0004 K/sec), improvements can be contemplated which would control these rates better. For example, the model currently has the shaft connected directly to the center of the aluminum endcap of the sensor module, essentially a worst-case solution. A set of Kevlar straps between the shaft and the sensor could provide high stiffness with lower conductance. However, such improvements, as well as better fidelity modeling of the inner structure of the sensor, require more sensor design detail.

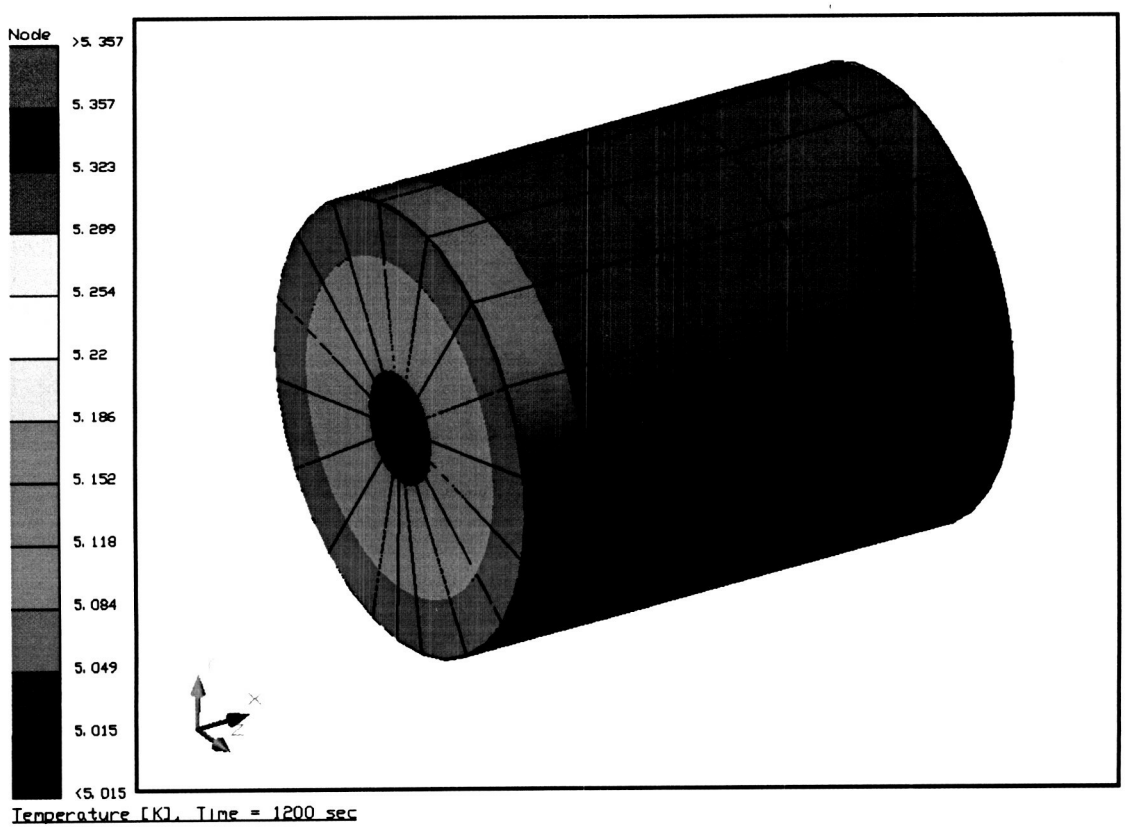

Figure 4 Sensor temperature distribution at end of 20 min.

INSTRUMENT ELECTRONICS OVERVIEW

The overall communication and control system for the experiment is shown below. Minimum electronics beyond that already in the detector are added to provide a data collection and status link to electronics mounted outside the vacuum chamber. The link electronics on the detector is a battery-powered RS-232 to IR transceiver comprised of a 110 ° field of view IR emitter-detector pair driven by an IR encoder-decoder and linked to an identical pair on the side of the chamber. The total power required for this portion of the interface should be less than 100mW. Presently the electronics will need to run at -40 ° C, but we will investigate if we can go lower.

The power and telemetry control box will be a comprised of a Book-sized PC with an Ethernet interface to a procured telemetry radio, such as the Freewave FGR1115RE 900MHz spread spectrum radio. A small IR to RS-232 module provides the interface to the IR transceiver inside the capsule. The externally mounted system will run from a single +12VDC 85W power source. The unit is expected to occupy a volume of 40cm*30cm*25cm.

The gondola will contain a standard SIP module for ground communication and control. We will need to provide an interface between the SIP telemetry interface and a radio that links to the experiment. This interface will essentially be the same design as the power and telemetry control box in the instrument.

Other means of communication within the capsule were considered, including a low power 2.4 GHz radio link, and this option could be a viable alternative if the IR link is not feasible. The major advantage to this approach would that the link does not depend on position, and the power would be about the same.

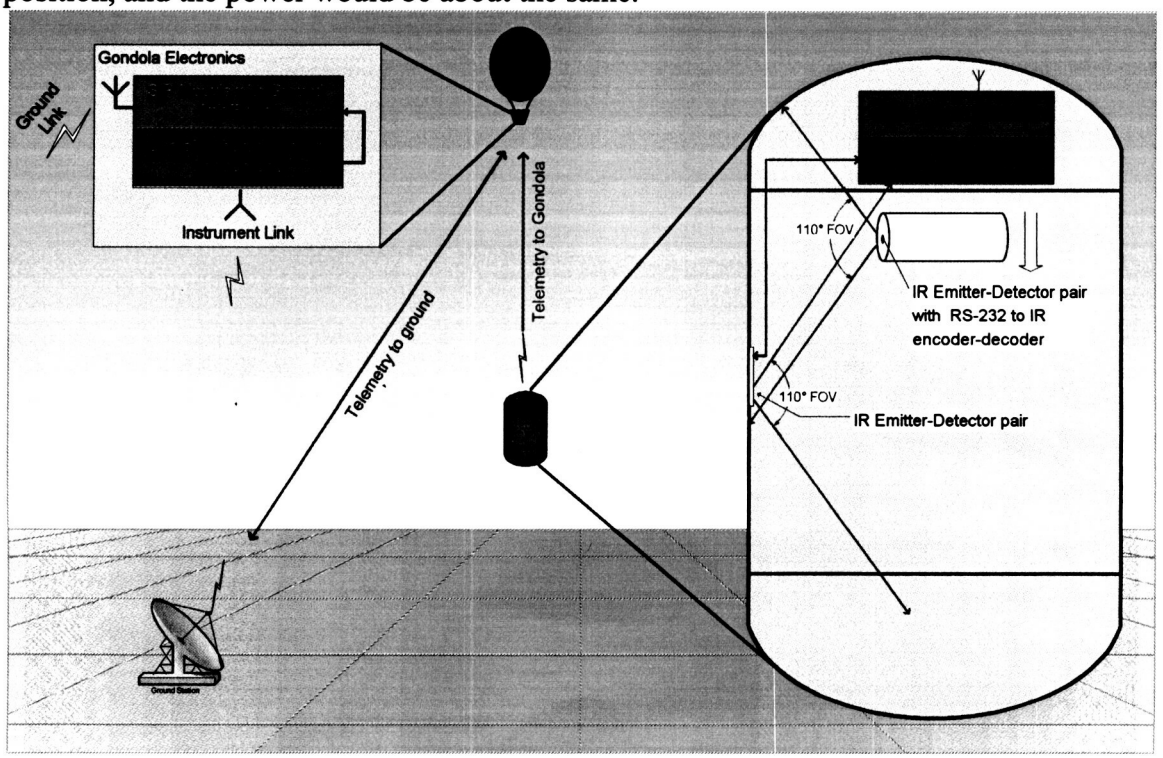

Figure 5 Schematic of telemetry links

SYSTEM REQUIREMENTS DEVELOPMENT

Table 6 is an update of key requirements of major subsystems.

Table 1 Development of Requirements vs. Design Drivers (version #2)

Design Driver	[redacted]	[redacted]	[redacted]	[redacted]
Free-fall (time > 20 s)	N/A	Transient damping time < 5 s;	N/A	$\beta_0 > 5000$ kg/m^2
Amplifier noise (white)	$< 6\times10^{-15}$ g/$\sqrt{\text{Hz}}$	Preamp. $T_N < 60$ mK	N/A	N/A
Brownian noise (white)	$< 6\times10^{-15}$ g/$\sqrt{\text{Hz}}$	$\omega_0/Q < 2\pi/10^5$ rad/s $T < 10$ K	LHe cryostat High-Q proof masses	N/A
Viscous drag on proof masses (dc)	$< 10^{-12}$ g	$p_d < 10^{-9}$ mBar	N/A	N/A
Temperature gradients [Radiometer effect, (ω)]	$< 5\times10^{-16}$ g	$\Delta T/\Delta x < 0.1$ K/m	T uniformity inside cryostat	N/A
Acceleration noise inside capsule in free fall	$< 10^{-12}$ g	CMRF $< 10^{-4}$	$p_c < 10^{-6}$ mBar	Structural and attitude freqs. >> ω
Earth's gravity gradients	$< 10^{-12}$ g (2ω) $< 10^{-15}$ g (ω)	Centering of proof masses (δ_x) along spin axis within 1 μm	N/A	Verticality before release $\delta_x\phi$ □ 0.1 μm-deg
Cryostat's gravity gradients (distributed mass)	$< 10^{-12}$ g (2ω) $< 10^{-16}$ g (ω)	Centering of proof masses within 10 μm	Cryostat internal diameter ≥ 1 m	N/A
Gravity gradients of lump masses on board capsule	$< 10^{-12}$ g (2ω) $< 10^{-16}$ g (ω)	Centering of proof masses within 10 μm	N/A	Mass-distance exclusion zones (see Annual#1, p. 33)
Magnetic disturbances	$< 10^{-16}$ g	Use Niobium alloy blanket around detector. Degauss proof masses	Temperature of package $T < T_c$ (T_c = critical temperature)	Limit magnetic moments outside sensor package $M_m <$ TBD A-m^2 and r > TBD m
Higher-order mass moments	$< 10^{-16}$ g	Proof masses with almost equal moments of inertia. Belted cylinders not required.	Mass of cryostat < 500 kg, Intern. dia. ≥ 1 m	N/A
Centrifugal gradients due to skewed rotation axis	$< 10^{-15}$ g	Centering of proof masses $\delta_x \leq 1$ μm	N/A	Verticality within 0.1°; rate errors at release ≤ 0.1 °/s

ω = signal angular frequency; ω_0 = detector resonant angular frequency

EXPERIMENTAL ACTIVITY (IFSI/CNR)[1]

Our partners have been working very hard in carrying out experimental activity on critical aspects of the detector development. The team at the Institute of Space Physics (IFSI/CNR) has already built a differential accelerometer prototype and carried out significant laboratory measurements on the prototype.

The prototype was designed with the goal of exploring key aspects of a differential accelerometer and not for carrying out a preliminary test of the Equivalence Principle in the laboratory. As such, the prototype has two sensing masses of the same material with their centers of masses close together but not perfectly coincident. The prototype has several features in common with the instrument that we expect to develop for the flight experiment as follow: same capacitive pick-up system; same elastic suspension of the sensing masses; same measurement chain to extract the differential signal from the accelerometer.

Figures 76 and 77 show a cross section of the differential accelerometer prototype when disassembled and assembled. Each sensing mass (blue and orange elements in the figure) is shaped to compenetrate (with leeway) into the opposing one so as to bring the two CMs close together (perfect coincidence is not a requisite for this prototype).

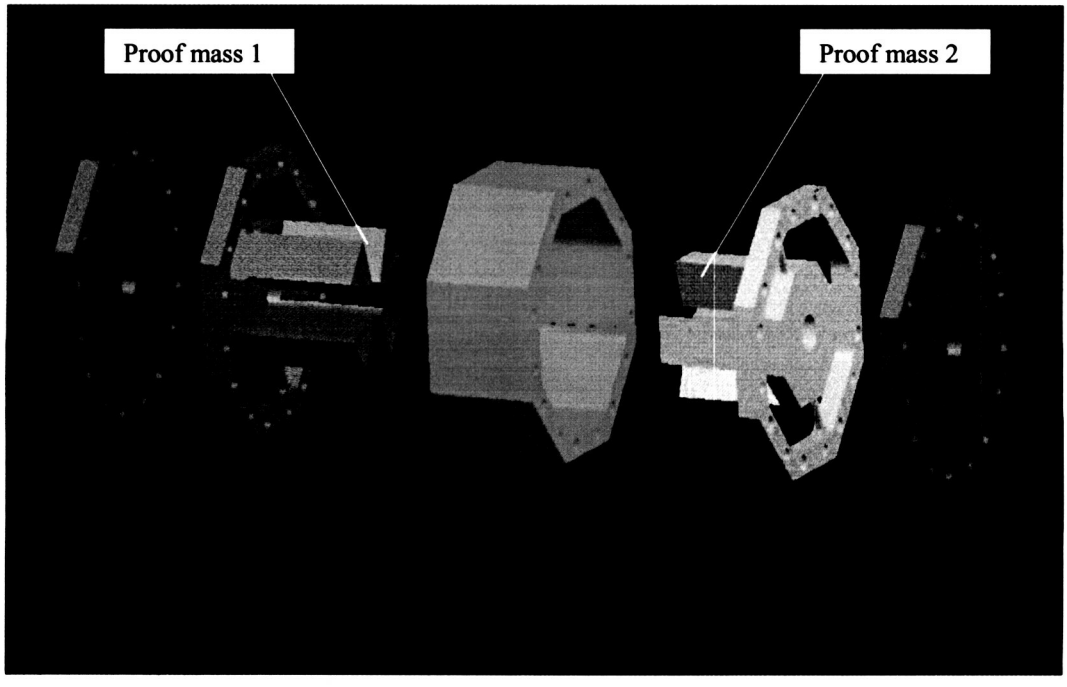

Figure 6 Exploded view of differential accelerometer prototype

[1] Section contributed by V. Iafolla and S Nozzoli of IFSI/CNR funded through Italian Space Agency (ASI).

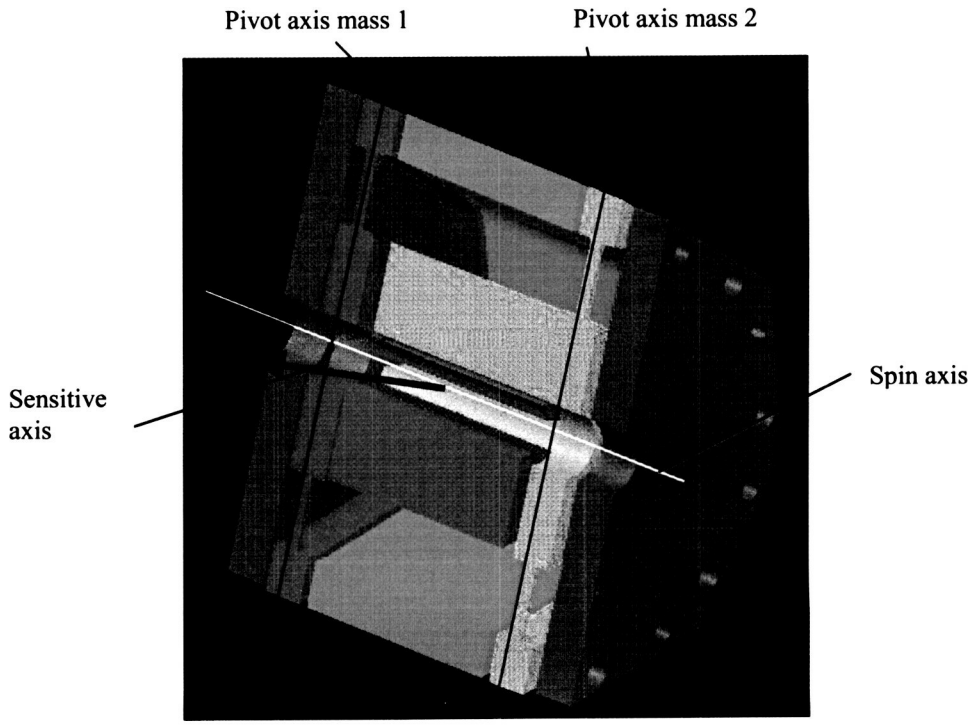

Figure 7 Cross section of (assembled) differential accelerometer prototype

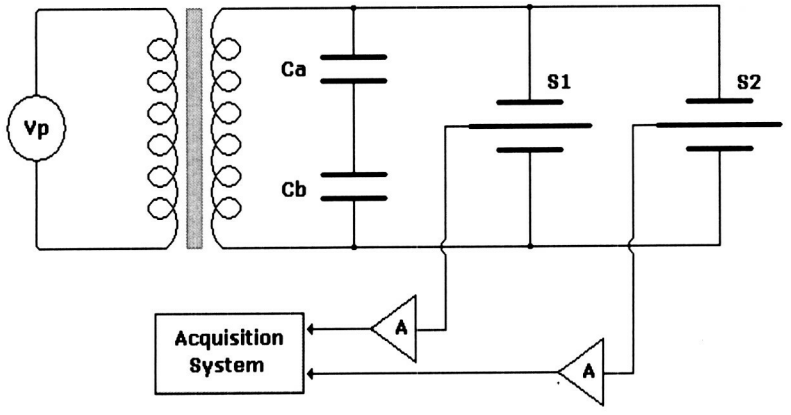

Figure 8 Simplified electrical diagram of signal pick-ups

Each sensing mass can rotate (through elastic restraints) about the pivot axis on each side of the accelerometer. The two pivot axes are parallel to one another. The sensitive axis of the differential accelerometer is perpendicular to the pivot axes and to the longitudinal axis of the instrument (spin axis). Each sensing mass has two fixed capacitor plates for signal pickup.

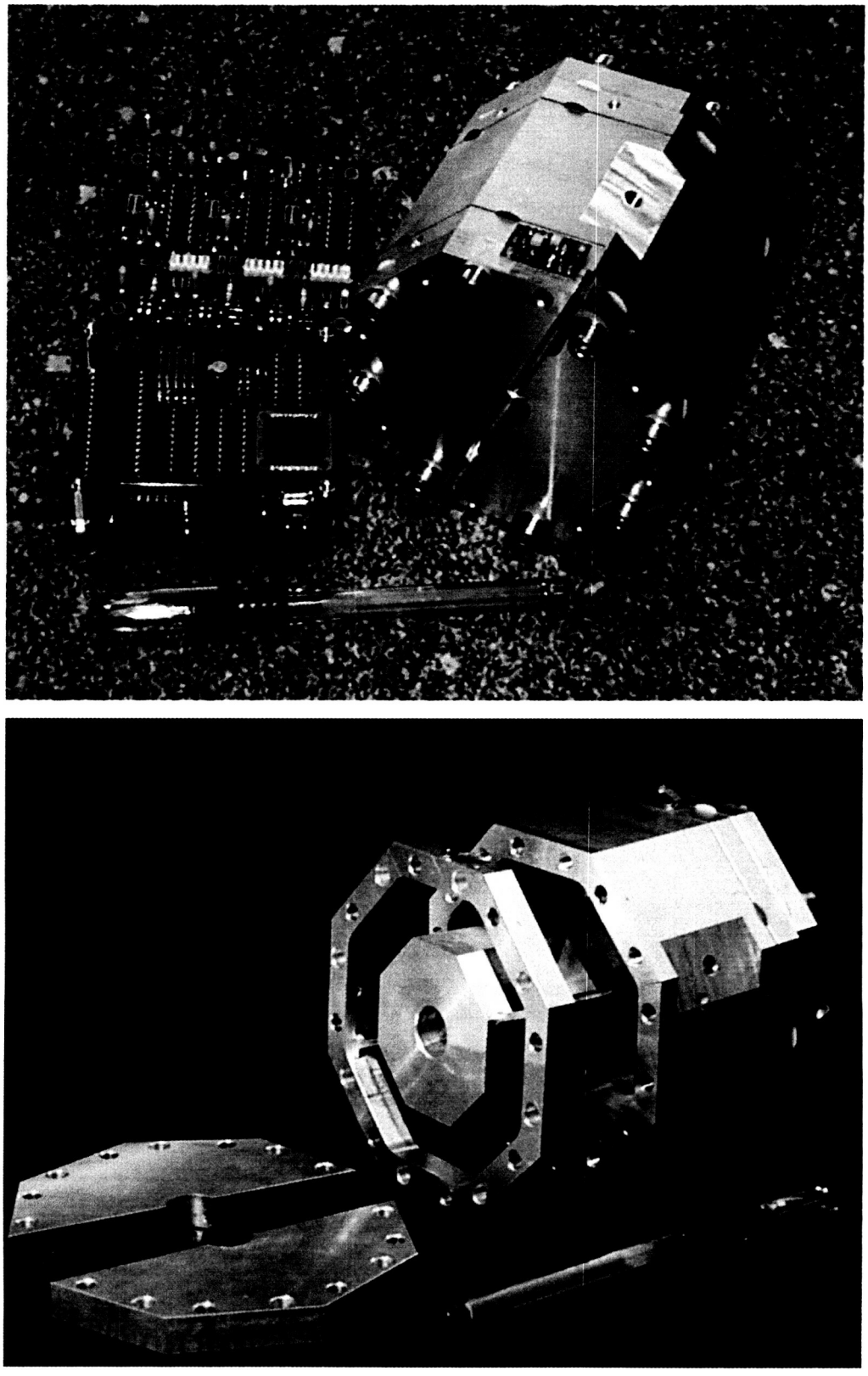

Figure 9 Pictures of differential accelerometer prototype

The output signals of the sensing masses are independently amplified and sent to the data acquisition system for conditioning, filtering and comparing. This prototype differential accelerometer builds on the heritage of (single) high-sensitivity accelerometers that were built by IFSI through the years. These accelerometers were tested extensively in the laboratory and in the field[xii]. Key characteristics of the differential accelerometer prototype are summarized in Table 1.

Table 2 Key characteristics of differential accelerometer prototype

Item	
Sensing mass	0.22 kg
Quality factor	2900
Resonance frequency	18.12 Hz
Preamplifier noise (K)	0.76
Preamplifier type	AD743 (commercial)

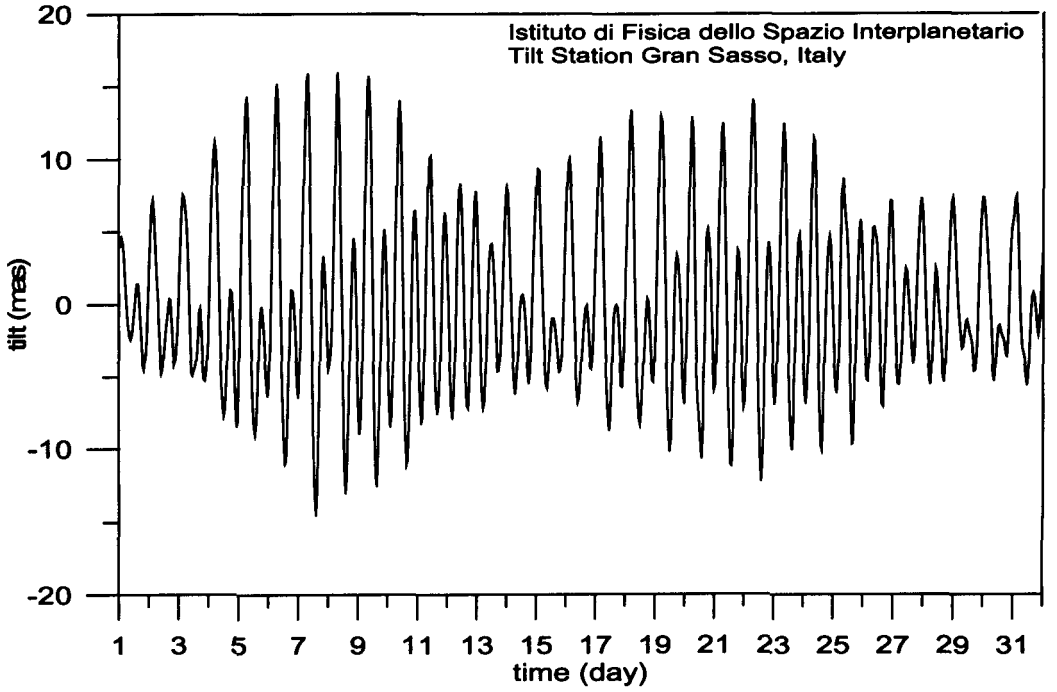

Figure 10 Tide signal filtered with 49-hour filter (1 mas = 2.78×10^{-7} g) and measured with single accelerometer. August 1998.

The single accelerometer, in its various implementations, has demonstrated a remarkable sensitivity and repeatability. The accelerometer was able to resolve a modulated gravity signal (at 0.3 Hz) with a strength of less than 10^{-9} g in the presence of seismic noise. Another single accelerometer is used to measure the Luni-Solar tides (working as a tilt meter) in the Gran Sasso laboratory (Italy). Excellent tidal signal over periods of months have been measured by the IFSI team. A month-long sample of a Luni-Solar tide in August 1998 is shown in Fig. 80 as an example of the performance of the single accelerometer in the field.

Damping of transient oscillations

The differential accelerometer prototype was developed and built to test, thus far, key aspects of differential acceleration measurements as follows: (a) abatement of the natural dynamics excited by the instrument release into the capsule; and (b) rejection of the common-mode signals. Point (a) above is critical for the success of our experimental scheme. For an instrument that is required to measure acceleration of 10^{-14} g, the release is an abrupt event that pushes the detector well beyond its saturation point. Moreover, a (flight) instrument with a Quality factor (Q) of order 10^5 and a resonance frequency of a few Hz, it would take a very long time for the oscillation to decay to within the instrument's dynamic range. The strategy that we plan to follow in the experiment is to reduce the Q factor during the first few seconds of fall from 10^5 down to a few units. The reduction of the Q factor is accomplished by inserting a resistance in the feedback control loops of the accelerometer. The technique has been tested successfully on the prototype accelerometer.

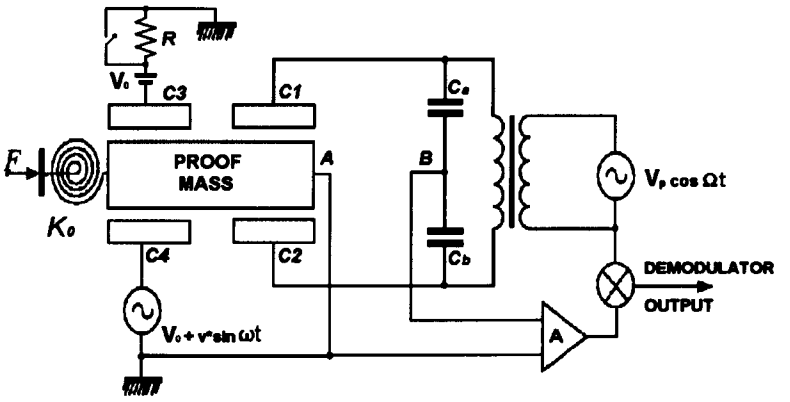

Figure 11 Electrical diagram of one test mass pickup system with resistance added to the feedback loop

Figure 82 shows the oscillation amplitude (from the oscilloscope output) of the accelerometer after an excitation. The accelerometer has a resonant frequency of 18.5 Hz and an (undamped) $Q_t = 2900$. The introduction of 50×10^6 ohm resistive load in the feedback loop, reduces the Q from its undamped value to $Q_t' = 441$ and, consequently,

the oscillation amplitude decays much more rapidly. Subsequently, the resistance is removed to demonstrate that this operation does not re-excite the oscillation amplitude.

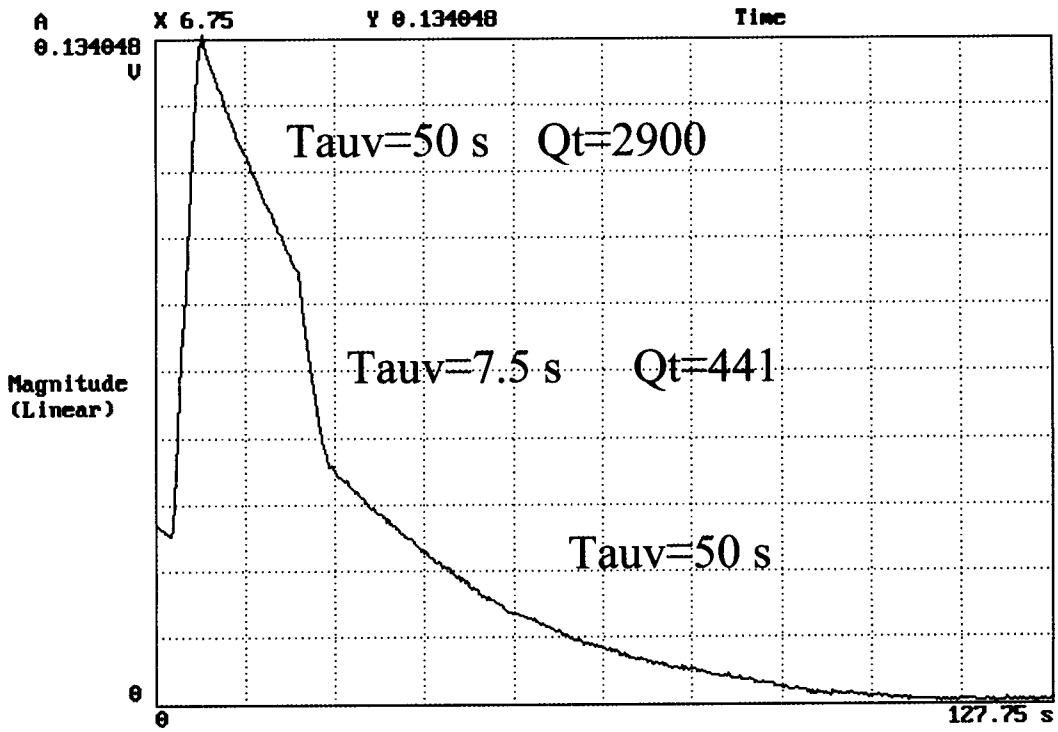

Figure 12 Oscillation amplitude decay vs. time with and without resistance inserted in the feedback loop

It is worth reminding that the decay of the proof mass oscillations is driven by the total quality factor of the electro-mechanical system which is as follows:

$$\frac{1}{Q_t}=\frac{1}{Q_m}+\frac{1}{Q_e} \quad with \quad \frac{1}{Q_e}=\beta\frac{\omega_0 RC}{1+(\omega_0 RC)^2}$$

where β is the electro-mechanical coupling factor

$$\beta=\frac{CE^2}{m\omega_0^2}$$

that is the ratio of electrical energy to mechanical energy. The electro-mechanical coupling factor of the instrument prototype is a low $\beta = 0.01$. The flight instrument will have a value much closer to unity thanks to a lower value of ω_0 and higher value of the capacitance C. Consequently, an electrical resistance of the value adopted for this test coupled into the feed-back loop of the flight instrument will imply a reduction of the value of Q_t to a few units. In summary, this damping technique is able to provide the desired damping performance.

Common-mode rejection factor

One important characteristic of a differential accelerometer is its ability to reject perturbations that are not differential, i.e., common-mode disturbances. This ability is quantified by the common-mode rejection factor (CMRF).

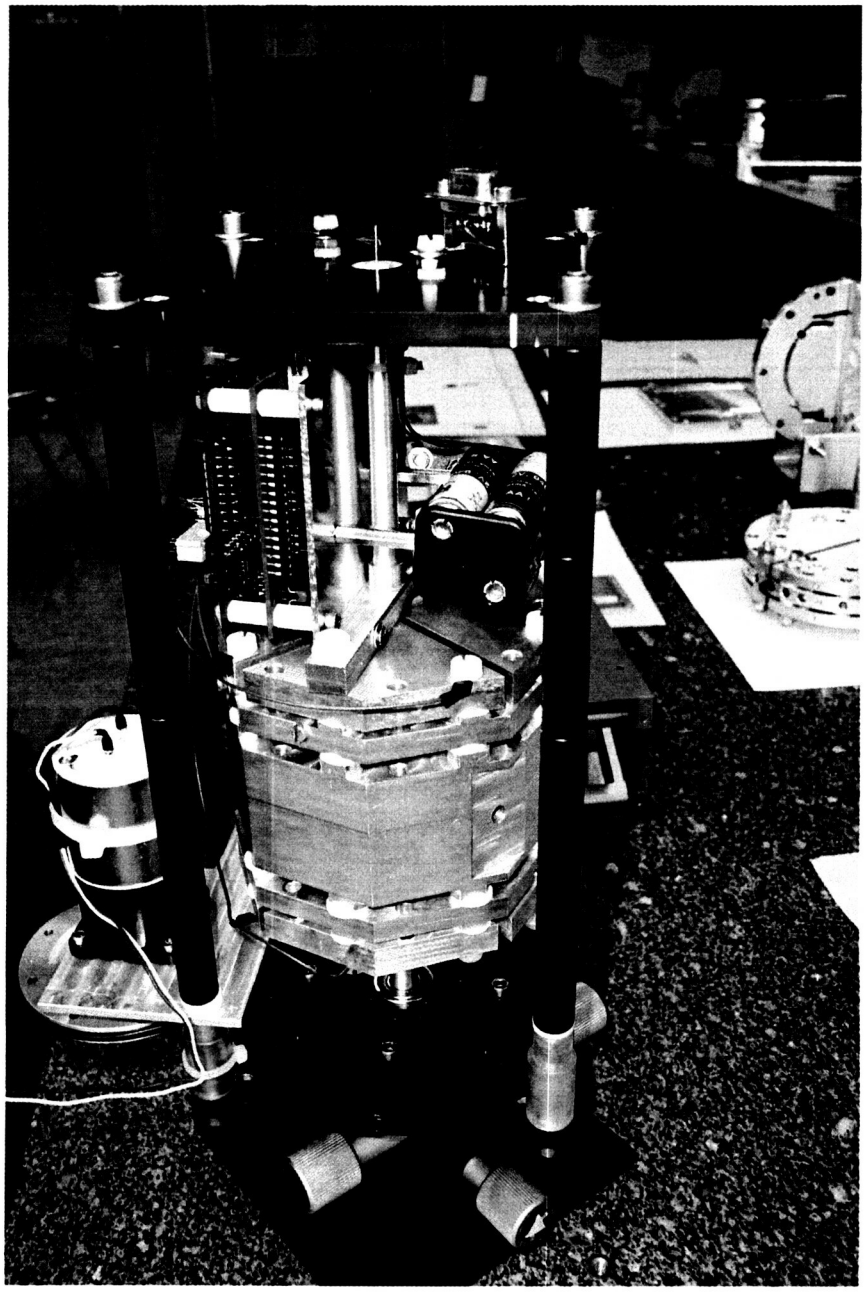

Figure 13 Experimental setup to perturb differential accelerometer with periodic common-mode disturbances.

The IFSI laboratory has built a rotating system whose rotation axis can be tilted away from the vertical (see Fig. 83). The accelerometer is mounted inside the rotating device with the sensitive axis orthogonal to the spin axis. The rotating outfit is tilted by about 10^{-3} rad away from the vertical and spun at a slow rotation with a frequency of 0.15 Hz. As the differential accelerometer slowly rotates, it measures a small component (proportional to the tilt) of the Earth's gravity field at the rotation frequency. This perturbation is a common-mode disturbance which affects equally the two proof masses.

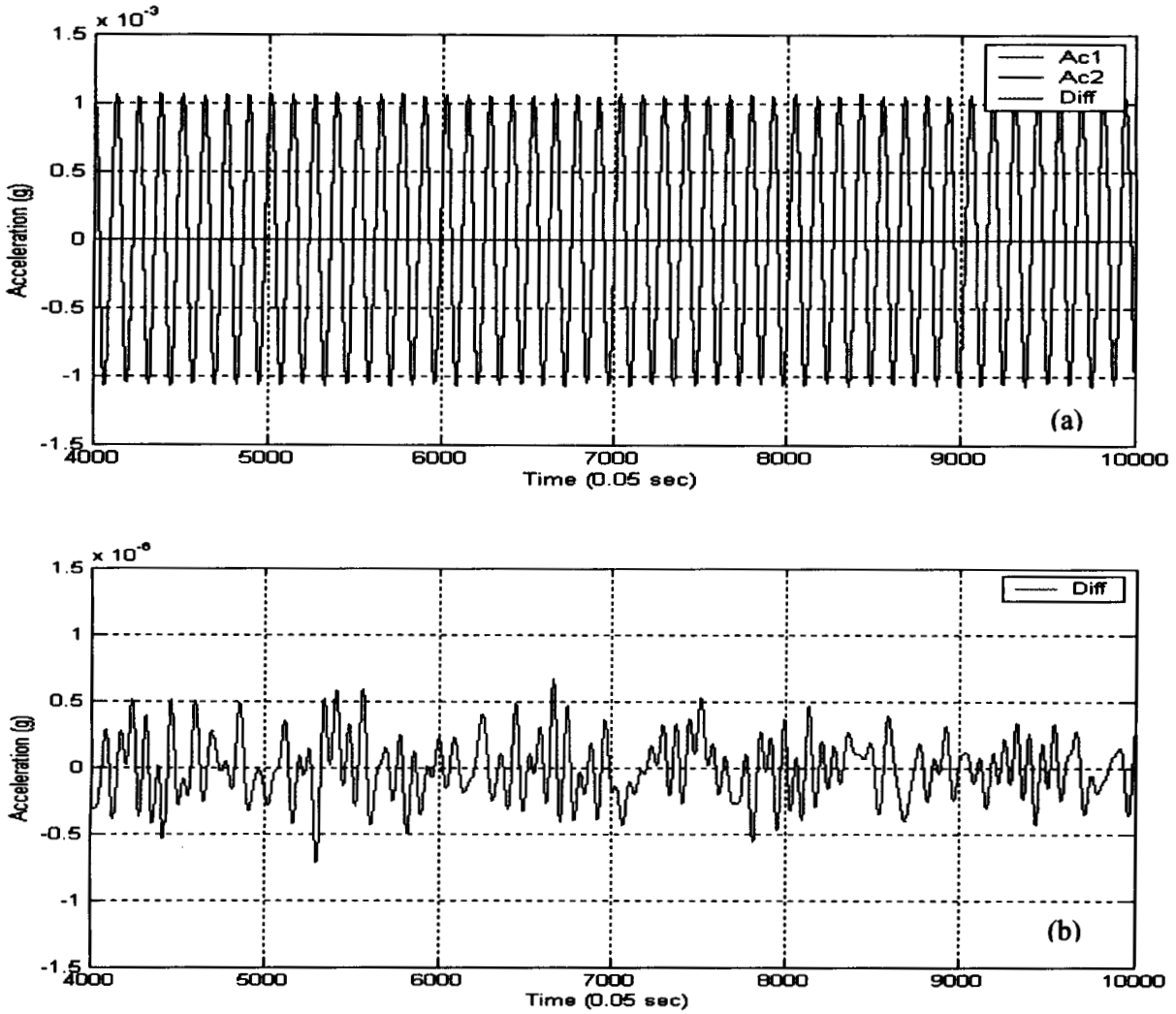

Figure 14 Accelerometer outputs: (a) single acceleration from proof mass 1 and 2 and (b) differential acceleration.

The differential output generated by the calibration signal is then treated by the software through spectral analysis of the individual signals to adjust the proportionality factors of the two sensing masses and the phase differences of their responses.

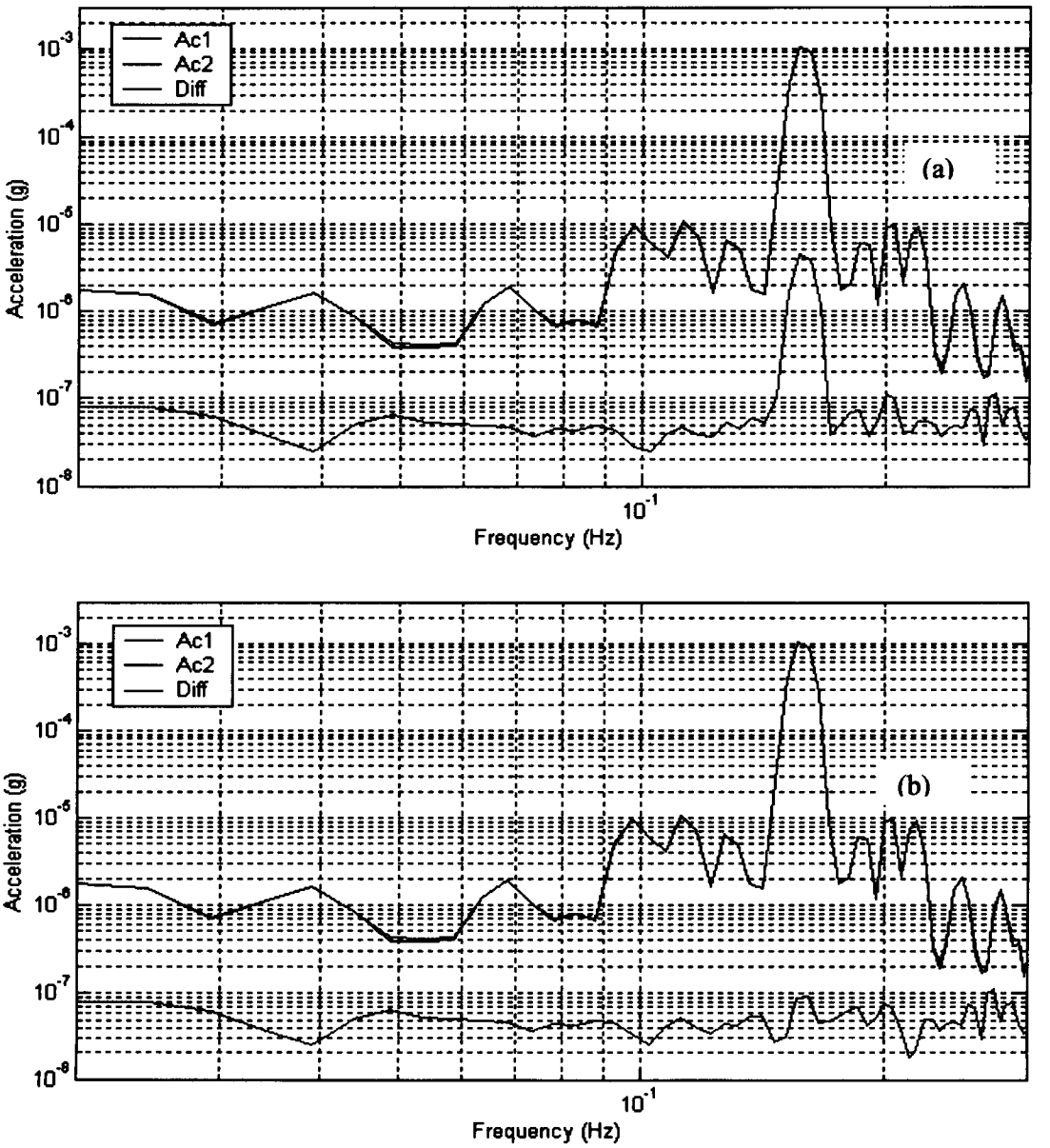

Figure 15 Spectra of individual and differential acceleration outputs: (a) after amplitude calibration only and (b) after amplitude and phase calibration.

Figure 85 shows that after calibrating for amplitude and phase a 10^4 attenuation is readily obtained for the differential signal. This level of attenuation is effective not only at the perturbation frequency of 0.15 Hz but also over a larger frequency band. An attenuation of 10^4 or equivalently a common-mode rejection factor of 10^{-4} meets the present requirement on the CMRF for the proposed tests of the Equivalence Principle.

Concluding remarks

The laboratory activity consisted in the construction of a laboratory prototype of a differential accelerometer. The laboratory prototype has been used to conduct key tests on the differential instrument. We demonstrated the ability to damp quickly transient oscillations by utilizing a resistive load in the feedback loops and then removing that load to reestablish a high quality factor of the detector. A rotating divide with tilt control was also built. This device was utilized to impart (through the Earth's gravity) common-mode perturbations to the differential accelerometer. These calibration disturbances have been used to trim the acceleration outputs of the individual proof masses in order to obtain a common-mode rejection factor better than 10^{-4} in a sufficiently large frequency band centered at the spin frequency.

KEY AREAS TO BE ANALYZED

Instrument package

- Simulate dynamics of instrument package and differential accelerometer during free fall in the presence of the gravity gradient field.
- Extract from simulated data an EP violation signal at the sensitivity threshold in the presence of errors at release, CM position errors and intrinsic noise of the detector.
- Analyze effect of gravity quadrupole disturbance on instrument package and compare results with requirement on common-mode rejection factor.
- Select inertia characteristics of instrument package and derive balancing requirements.

Leveling/Release mechanism

- Develop dynamic model of capsule attached to balloon gondola and study dynamics and stabilization before double release. Fine tune design concept.

Cryostat design (in cooperation with Janis Research and Topsfield Engineering)

- Dewar layout. Define interfaces. Evaluate mass and cost of cryostat.

Detector design

- Cooperate with our non-US partners on laboratory testing of instrument prototype to address critical issues related to the flight experiment;
- Cooperate with our non-US partners on proof mass design (for flight instrument) and mechanization of the detector.

Magnetic disturbances

- Revisit the early estimates of magnetic disturbances as a result of updated configuration of instrument package.
- Derive requirements of magnetic cleanliness for typical levels of ferromagnetic impurities in the sensing masses.

Appendix A: Implementation and Computer Code

The purpose of the code is to compute the force and the torque acting on each test mass, given arbitrary capsule. The test mass is characterized by its mass, and moment of inertia distribution (first, second and third order). The capsule is decomposed into few basic objects, such as cylinder, caps, and point mass, etc. The position of a test body relative to the capsule is given by its center of mass, C.M., and by its rotation matrix, Φ. The radius vector of the center of mass is expressed in capsule frame. The rotation matrix defines the rotation between the capsule frame, and the body frame (not necessarily the principal frame). The origin of the capsule coordinate system is at the center of the cylinder base, where the Z-axis (axisymmetry axis) is pointing upward.

The code was designed as general and as flexible as possible, and also with computational efficiency in mind. The user may define and add any number of basic capsule objects. The code was written in Matlab, and it contains m files as source code and mat files as data files. It also contains script language (in Matlab), for the purpose of automatic generation and reading of files.

The following figure shows a schematic description of the code. Attached below is the Matlab help file, located at the code directory. It describes the code and gives specific instructions how to run the code.

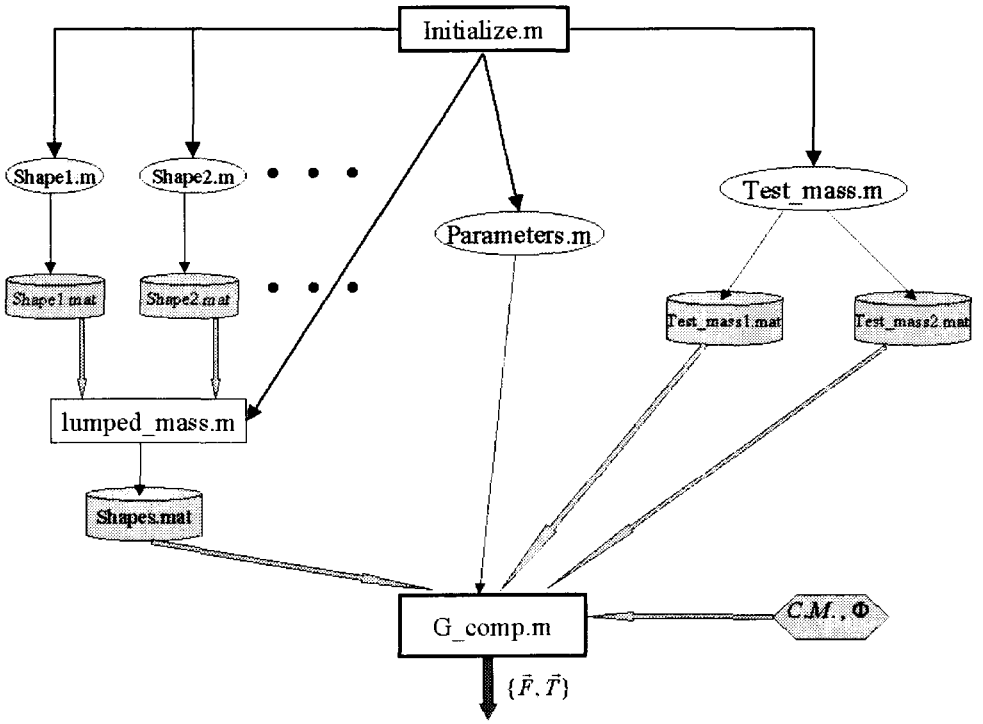

Figure A Flow-Chart of the Code

G_help.txt

```
General description
--------------------

The distributed mass elements for each shape are defined (by user) in
the files: shape#.m
Each file defines a particular shape (cylinder, cup, point mass, etc).
The output data is the element
coordinates vector: x#, y#, z#, and a mass vector: m#. These are saved
into shape#.mat files.
Note that the shape enumeration does not have to be in a specific
order. The user may add any number of
shape files, and these should save the date to the appropriate
shape#.mat files.
The test body is defined in the file: test_mass#.m, where # is an index
(ex: 1 or 2).
The user defined parameters are the body index, the mass and the
principal moments of inertia of the body.
The results are saved into the files: test_mass#.mat
The file: parameters.m defined (by user) global parameters.
It enables the user to include any combination of a given shape from
shape#.dat by defining the
index array: i_shape. This array includes the shape number. (ex:
i_shape=[1 3 6]).
The file lumped_mass.m reads any shape#.mat specified by i_shape, and
aggravates the coordinates vectors
and the mass vectors into single vectors: x,y,z and m. These vectors
are saved into the file: shapes.mat
The force/torque computation is done in the function file: G_comp.m
It loads the data files: shapes.mat and test_mass.mat
The input arguments to this function are: 1. body. It is a cell array
contains the CM position and the
transformation matrix for the orientation of the body, relative to the
capsule frame. 2. The body index.
The output of this function are arrays of force and array of torque.

Software usage
--------------------

The package include the files:

initialize.m
parameters.m
test_mass.m
shape#.m ....
G_comp.m
G_driver.m

These files generate a stand alone application, when using the driver:
G_driver to run the code.
However, for a future usage, the function: G_comp can be a part of a
dynamical simulation code,
with the interface of the input/output of this function.
The software consists of two functionalities:
```

1. Initialization of the data files: *.mat and the global parameters.
2. Gravitational computation.

Once the user initializes, G_comp.m can be run independently.

To run the code, the following action should be taken:

- Defining the parameters in: shape#.m ..., test_mass.m and in parameters.m
- Typing as command line: initialize
- Defining in G_driver: body index, body{1}=CM and body{2}=Trans, or defining it in other calling routine.
- Typing as command line: [F,T]=G_comp(body,index)

Appendix B: Gravitational Model for the Caps

The discretization of the flat cup is by using a rectangular grid, where the lumped-masses are allocated at the mid-layer.

In order to verify the precision of the discrete model, we will compare it with an analytical model.

It is easy to see that the axial force between a point mass, m, and a finite size disk with radius R_c and density ρ, is:

$$Fz = 2\pi G\rho m \int_{\eta=Z-t/2}^{Z+t/2} \int_{r=0}^{R_c} \frac{r\eta}{\left(r^2+\eta^2\right)^{3/2}} dr\, d\eta$$

where Z is the radius vector between the point mass and the center of the disk.

The resulting force is:

$$Fz = 2\pi G\rho m\left[t - \sqrt{\left(Z+\frac{1}{2}t\right)^2 + R_c^2} + \sqrt{\left(Z-\frac{1}{2}t\right)^2 + R_c^2}\right]$$

However, our model is equivalent with a thin layer distribution of masses. So, the analytical expression for the force between a point mass and a thin disk is computed by applying the limiting process for t:

$$\underset{t\to 0}{Fz} = 2\pi Gm \lim_{t\to 0} \frac{\rho_A}{t}\left[t - \sqrt{\left(Z+\frac{1}{2}t\right)^2 + R_c^2} + \sqrt{\left(Z-\frac{1}{2}t\right)^2 + R_c^2}\right]$$

where $\rho_A = t \cdot \rho$, thus ρ_A is the area density. The resulting approximation is:

$$\underset{t\to 0}{Fz} = 2\pi G\rho m t\left(1 - \frac{Z}{\sqrt{Z^2+R_c^2}}\right)$$

The question now is where is the best location of the thin disk (i.e. somewhere between the lower and upper surfaces of the cup). Figure C1 compares the axial force due to a finite thickness disk with the force due to a thin disk. The location of the thin disk varies between the lower surface and the upper surface. It is normalized by the thickness, so its value at the lower surface is 0 and its value at the upper surface is 1. Z is the radius vector between a point mass of 1 kg, and the middle of the cup. It is obvious that the best location for the thin disk is at the middle of the cup.

This argument can be proved analytically as well. Suppose that Z_0 is the radius vector for the thin disk (unknown, so far), and Z is the radius vector to the middle of the cup. Comparing the corresponding forces results in,

$$\frac{Z_0}{\sqrt{{Z_0}^2+R_c^2}} = \frac{1}{t}\cdot\left(\sqrt{\left(Z+\frac{1}{2}t\right)^2+R_c^2}-\sqrt{\left(Z-\frac{1}{2}t\right)^2+R_c^2}\right)$$

This equation can be solved for $t/R_c << 1$, and a straightforward expansion leads to,

$Z_0 = Z + O\left(\frac{t}{R_c}\right)^2$, as expected.

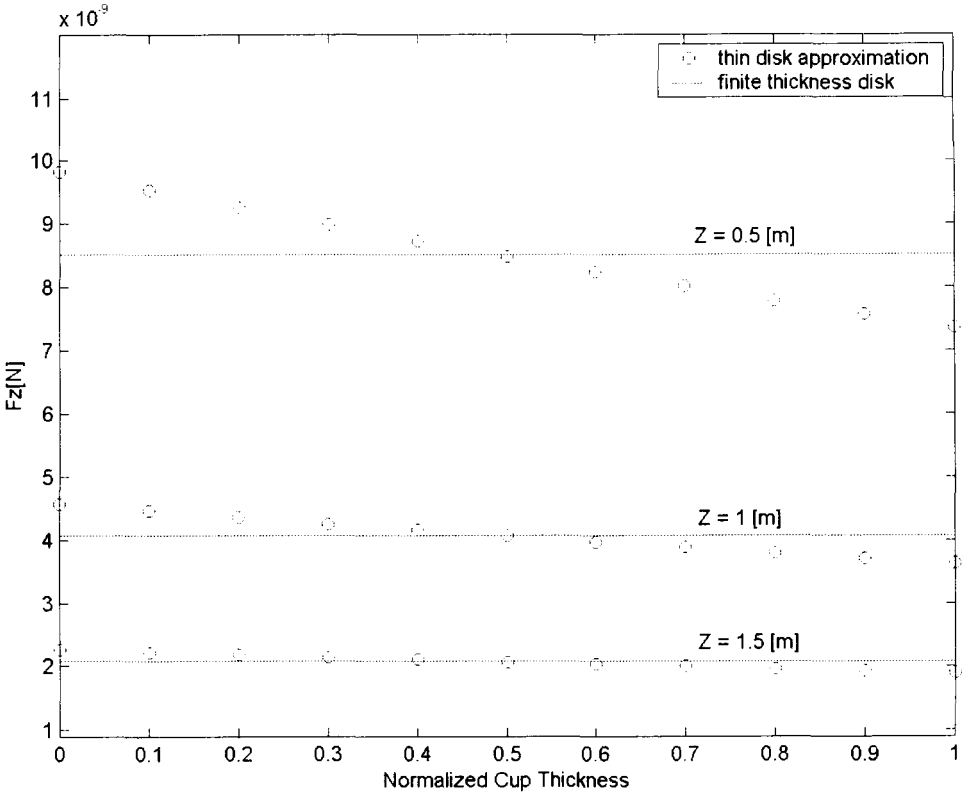

Figure B1. Forces due to various locations of thin disk compared with forces due to finite thickness disk

The next question concerns the sufficient discretization. Let N be the number of grids along the diameter. (The number of cells, that is the number of lumped-masses, becomes closer to $\frac{\pi}{4}N^2$ as $N\to\infty$). Figure C2 shows the axial force between the two caps, for a

point mass of 1 kg. Even a crude discretization (N=4) gives a reasonable approximation. In our code we take N=20; sufficiently to represent the caps.

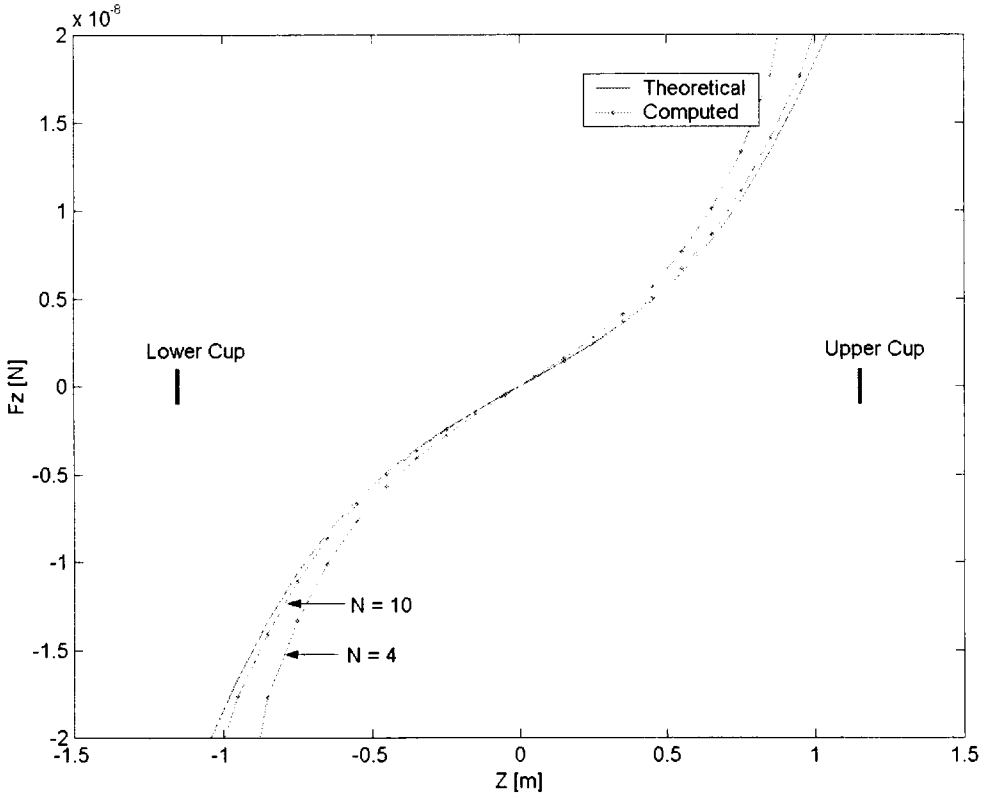

Figure B2. Effect of discretization on axial force between two caps

Appendix C: Gravitational Model for the Cylinder

The discretization of the flat cup is by done by dividing the circumference into sectors, and the height into rectangular grid, in a way that the horizontal and the vertical solid angles are equal.

In order to verify the precision of the discrete model, we will compare it with an analytical model.

The axial force between a point mass, m, at height h from the cylinder button, and a finite thickness cylinder with internal radius R_1, external radius R_2, height H and density ρ is:

$$Fz = 2\pi G\rho m \int_{\eta=-h}^{H-h} \int_{r=R_1}^{R_2} \frac{r\eta}{\left(r^2+\eta^2\right)^{3/2}} dr\, d\eta$$

The first integration is related to the force between the mass element and a hollow disk, at a distance η. The second integration is along the height of the cylinder.

The resulting force is:

$$Fz = 2\pi G\rho m[\sqrt{R_1^2+(H-h)^2} - \sqrt{R_1^2+h^2} - \sqrt{R_2^2+(H-h)^2} + \sqrt{R_2^2+h^2}]$$

Note that in order to work with coordinate system that is centered at the middle height (X, Y, Z), we have to apply the following transformation: $h \leftarrow H/2+Z$

Next, we compute the thin cylinder approximation force (as our discrete model), and compare it with the finite thickness force.

$$\underset{t\to 0}{Fz} = 2\pi G m \lim_{t\to 0} \frac{\rho A}{t}[\sqrt{R_1^2+(H-h)^2} - \sqrt{R_1^2+h^2} - \sqrt{(R_1+t)^2+(H-h)^2} + \sqrt{(R_1+t)^2+h^2}$$

The resulting approximation is:

$$\underset{t\to 0}{Fz} = 2\pi G m\rho t\left(\frac{1}{\sqrt{R^2+h^2}} - \frac{1}{\sqrt{R^2+(H-h)^2}}\right)$$

The best R is found by comparing the thin cylinder approximation with the finite thickness formula. Figure C1 suggests that $R \cong (R_1 + R_2)/2$ is the best place to locate the approximate cylinder.

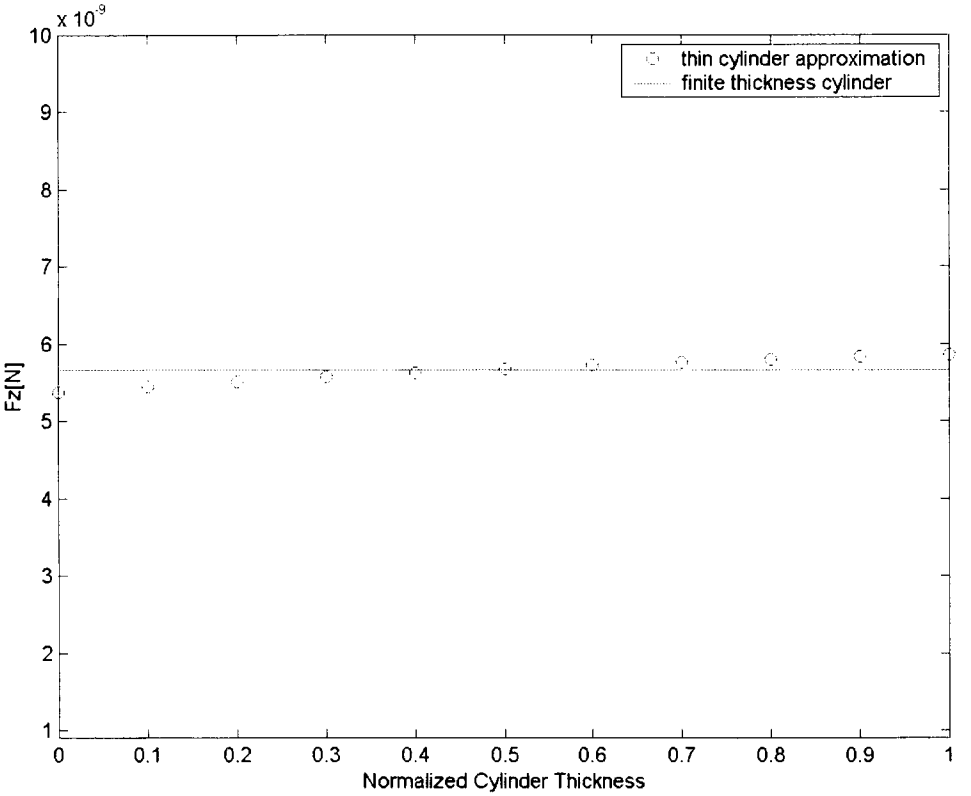

Figure C1: Axial force due to various radius of thin cylinder compared with an axial force due to finite thickness cylinder

The accuracy of the discretization is demonstrated in figure C2. The axial force computed by the thin cylinder approximation is compared with numerical solution of the discrete model. The angular interval between the lumped-masses is 1 degree. Note that even an angular interval of 6 degrees gives a reasonable model (the maximal error is less than 1%).

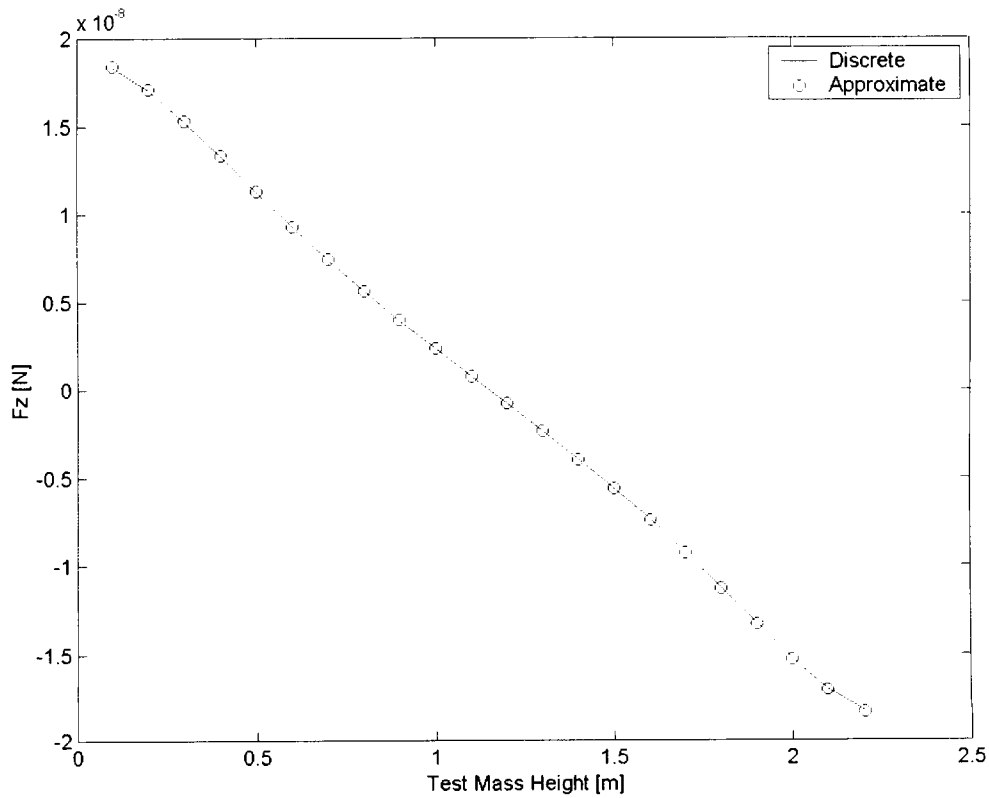

Figure C2. Axial force for a test mass along the cylinder axisymmetrical axis: analytical Vs numerical solutions

Appendix D: Interpolation of the Gravitational Force Field by Radial Basis Functions

The computation of the gravitational force inside the capsule is time consuming, especially when considering a dynamical simulation of the test masses. In this case, the gravitational field has to be evaluated at each integration instance. The computational efficiency may increases dramatically if we represent the gravitational field by a low order functional approximation.

Our interpolation method is generally subjected to two requirements. First, the approximate surface should be close enough to the computational surface. Second, the approximate surface should be as smooth as possible. The second requirement guarantees the computation of a gravity gradient field. Therefore, we avoid using any interpolation that introduces high frequencies and has ill convergence (for example, polynomial approximation). A feasible interpolation method is the following Radial Basis Functions (RBF) method.

Consider a mapping from a d-dimensional input space, X, to a one-dimensional target space, T. In our problem the input space consists of the radial direction, x, and the axial direction, z, (d = 2). The target space is a component of the gravitational force, Fx or Fz. The data set consists of N input vectors X, together with the corresponding N targets. The goal is to find a function S(X), such that $S(X_n) = t_n$; $n = 1,\ldots,N$. That is, the mapping should be exact at the fitting points, and approximates the rest of the field.

The RBF approach introduces a set of N basis functions, one for each data point. We adopted RBF in the Gaussian form:

$$R_n(\| x - t_n \|) = \exp\left[-\frac{(X - t_n)^2}{2\sigma_n^2}\right]$$

Note that each training data serves as a center for the basic function, R_n.

The variance σ determines the locality of each RBF. Small variance will result is a good local fitting but worse fitting between the training data, and worse smoothing. While a large variance will result in a better smoothing but worse local fitting. The interpolation function is a linear combination of the RBF, in the form:

$$S(X) = \sum_{n=1}^{N} w_n \exp\left[-\frac{(X - t_n)^2}{2\sigma_n^2}\right]$$

Assuming constant variance, the mapping relations of the N fitting points results in the following linear system:

$$\underbrace{\begin{bmatrix} \exp\left[-\frac{(X_1-X_1)^2}{2\sigma^2}\right] & \exp\left[-\frac{(X_1-X_2)^2}{2\sigma^2}\right] & \cdots & \exp\left[-\frac{(X_1-X_N)^2}{2\sigma^2}\right] \\ \exp\left[-\frac{(X_2-X_1)^2}{2\sigma^2}\right] & \exp\left[-\frac{(X_2-X_2)^2}{2\sigma^2}\right] & \cdots & \exp\left[-\frac{(X_2-X_N)^2}{2\sigma^2}\right] \\ \vdots & \vdots & \vdots & \vdots \\ \exp\left[-\frac{(X_N-X_1)^2}{2\sigma^2}\right] & \exp\left[-\frac{(X_N-X_2)^2}{2\sigma^2}\right] & \cdots & \exp\left[-\frac{(X_N-X_N)^2}{2\sigma^2}\right] \end{bmatrix}}_{\Phi} \underbrace{\begin{bmatrix} w_1 \\ w_2 \\ \vdots \\ w_N \end{bmatrix}}_{W} = \underbrace{\begin{bmatrix} t_1 \\ t_2 \\ \vdots \\ t_N \end{bmatrix}}_{T}$$

The matrix Φ is well conditioned under certain conditions, determine by the size of the system and the covariance. The solution for the weights is:

$$W = \Phi^{-1} T .$$

The RBF for the force field was carried out as follows. The training data is taken in the region of the expected trajectory (21 points), as demonstrated in the figure below.

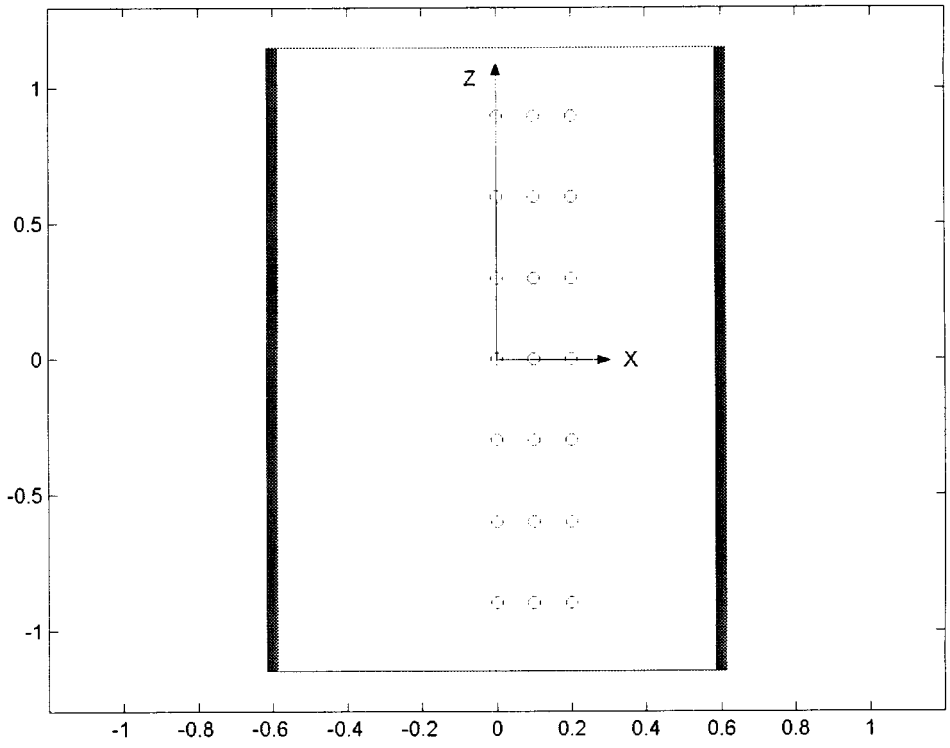

Figure D1. The training data for the RBF approximation inside a cylinder

The forces Fx and Fz were computed for each training point. The quality of the fitness is demonstrated for Fx (harder surface to fit than Fz). The variance was taken as 1m. The worst fitting is about 0.2%.

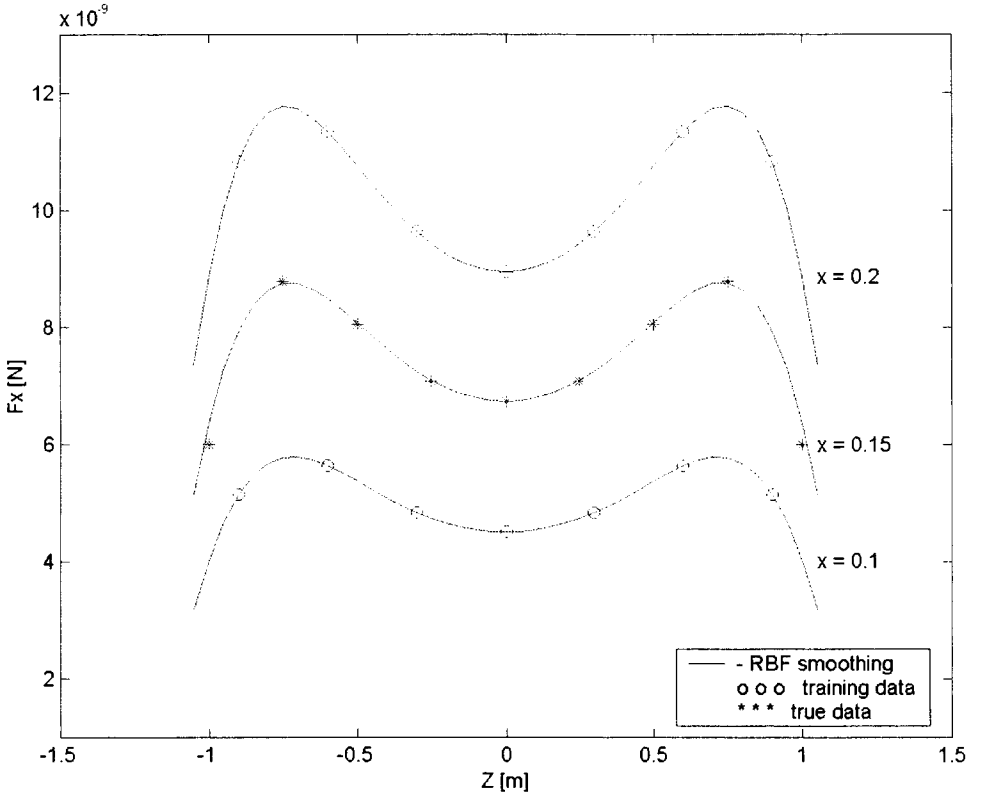

Figure D2. Validation of the RBF approximation for the radial force

The interpolated surfaces for Fx and Fz are shown below. The computation of these is very efficient now, because it requires the evaluation of only 21 exponential terms. Note that this example is related to a simple open cylinder. The force field due to a more complicated chamber, with additional attracting elements, will be handled with almost the same computational effort. That is, after the computation of the force field for the training points, only 21 RBF evaluations are required for approximating the force field at a different location.

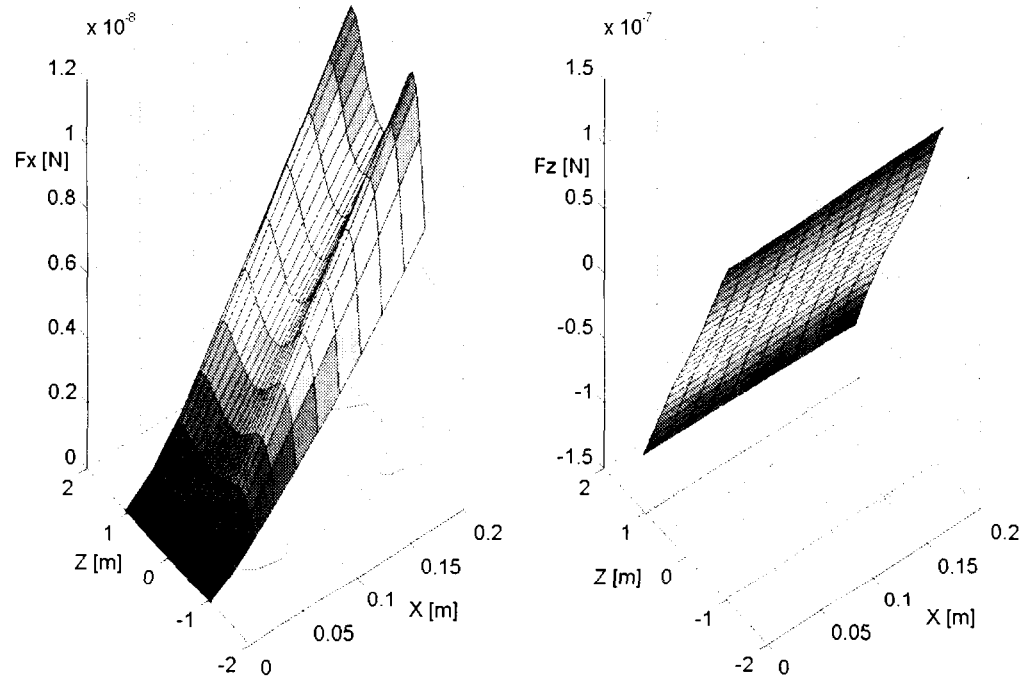

Figure D3: RBF approximate surfaces for Fx and Fz

Note that there is a fitting problem when the force field consists of terms of different order of magnitude. In this case the RBF will fit only the largest terms. Given a force field expressed as: $F = F^{(1)} + F^{(2)} + \cdots$, a feasible solution is to approximate each term by a different RBF, such that the approximate force field becomes: $\tilde{F} = \tilde{F}^{(1)} + \tilde{F}^{(2)} + \cdots$.

Another approach is to start from the gravitational potential. After evaluating the potential of the capsule/test-body at the training points, and computing the RBF weights, taking the gradient of the RBF representation gives the forces. A similar approach, for evaluating the gravity gradient, is demonstrated in the following section.

One of the advantages of using RBF is the smoothness that enables us to compute the gradient. The gravity gradient field can be also interpolated by analytical computation, and then approximating it by RBF. However, the analytical expression for the gravity gradient of a high-order potential may be a very complicated. Therefore, our approach is to compute the RBF for the force field and use it as a generating function for the gravity gradient.

Let $\vec{F}$ be the force field expanded in RBF.

$$\vec{F} = \sum_{n=1}^{N} \vec{W}_n \exp\left[-\frac{r_n^2}{2\sigma^2}\right]$$

where $r_n^2 = (x - x_n)^2 + (y - y_n)^2 + (z - z_n)^2$, $\vec{W} = [w^X, w^Y, w^Z]^T$, and $\vec{F} = [Fx\ Fy\ Fz]^T$.

The gravity gradient is then,

$$G = \nabla_r \vec{F} = \begin{bmatrix} \nabla_X F_X & \nabla_Y F_X & \nabla_Z F_X \\ \nabla_X F_Y & \nabla_Y F_Y & \nabla_Z F_Y \\ \nabla_X F_Z & \nabla_Y F_Z & \nabla_Z F_Z \end{bmatrix}$$

Given a RBF force field at a point r, the RBF force field at an adjacent point is:

$$\begin{bmatrix} Fx \\ Fy \\ Fz \end{bmatrix}_{(r+\Delta r)} = \begin{bmatrix} Fx \\ Fy \\ Fz \end{bmatrix}_{(r)} + G(r) \begin{bmatrix} \Delta x \\ \Delta y \\ \Delta z \end{bmatrix}$$

Let $\varphi(r_n) = \exp\left[-\frac{r_n^2}{2\sigma^2}\right]$ be a local radial basis function, then its gradient is:

$$\nabla_r \varphi(r_n) = -\frac{1}{\sigma^2}\left[(x - x_n)^2 \quad (y - y_n)^2 \quad (z - z_n)^2\right] \exp\left[-\frac{r_n^2}{2\sigma^2}\right]$$

The gravity gradient expressed in RBF is the following superposition of the gradients of the local radial basis functions.

$$G = \sum_{n=1}^{N} \vec{W}_n \nabla_r \varphi(r_n)$$

The final form of the RBF gravity gradient is:

$$G = -\frac{1}{\sigma^2} \sum_{n=1}^{N} \begin{bmatrix} w_n^X (x - x_n) & w_n^X (y - y_n) & w_n^X (z - z_n) \\ w_n^Y (x - x_n) & w_n^Y (y - y_n) & w_n^Y (z - z_n) \\ w_n^Z (x - x_n) & w_n^Z (y - y_n) & w_n^Z (z - z_n) \end{bmatrix} \exp\left[-\frac{r_n^2}{2\sigma^2}\right]$$

REFERENCES

[i] R.V. EÖTVÖS, Math. u. Naturw. Ber. aus Ungarn Vol. 8, 65 (1890).

[ii] R.V. EÖTVÖS, V. PEKAR AND E. FETEKE, "Beitrage zum Gesetze der Proportionalität von Trägheit und Gravität," *Annalen der Physik*, Vol. 68, 11-66 (1922).

[iii] P.G. ROLL, R. KROTKOV AND R.H. DICKE, *Annals of Physics*, Vol. 26, 442 (1964).

[iv] I.I. SHAPIRO, C.C. COUNSELMAN AND R.W. KING, *Phys. Rev. Lett.* Vol. 36, 555 (1976).

[v] J.G. WILLIAMS ET AL., *Phys. Rev. Lett.* Vol. 36(11), 551 (1976).

[vi] Williams, J.G., X.X. Newhall and J.O. Dickey (1996), Relativity parameters determined from lunar laser ranging, *Phys. Rev. D*, 53, 6730.

[vii] Baessler S., Heckel B., Adelberger, E. Gundlack J., Schmidt U. and Swanson E. (1 Nov. 1999), *Phys Rev Lett.*, Vol. 83.

[viii] Damour, T., F. Piazza, and G. Veneziano, "Violations of the Equivalence Principle in a dilaton-runaway scenario." Phys. Rev. D66, 046007:1-15, 2002.

[ix] Damour, T., F. Piazza, and G. Veneziano, "Runaway dilaton and Equivalence Principle violations." Phys. Rev. Letters, Vol. 89, No. 8, 081601:1-4, 2002.

[x] I. Shapiro et al., "Test of the equivalence principle in an Einstein elevator. " Annual Report #1on NASA Grant NAG8-1780, May 2002.

[xi] Lazarevich, A. et al., "Balloon-borne, high altitude gravimetry: the flight of Ducky Ia." Report AFGL-TR-0342, Air Force Geophysics Laboratory, Hanscom AFB, MA, 1985.

[xii] Iafolla et al., "Measurements at Gran Sasso laboratory", see web site http://iafosun.ifsi.rm.cnr.it/~iafolla/gravsper.html.